République Algérienne Démocratique et Populaire
Ministère de l'Enseignement Supérieur et de la Recherche Scientifique
Université A.MIRA-BEJAIA

جامعة بجاية
Tasdawit n Bgayet
Université de Béjaïa

Faculté : Des Sciences Exactes
Département : Physique
Laboratoire ou unité de recherche de rattachement : Physique Théorique

THÈSE

EN VUE DE L'OBTENTION DU DIPLOME DE DOCTORAT

Domaine : Sciences de la matière Filière : Physique
Spécialité : Physique théorique

Présentée par

Hilal Hamdellou

Thème

Probing the Higgs-Gauge Couplings at Leptonic Colliders

Soutenue le : 12/04/2025 **Devant le Jury composé de :**

Nom et Prénom	Grade		
Nadia Oulebsir	**MCA**	Univ. de Bejaia	Présidente
Amine Ahriche	**Prof**	Univ. de Sharjah, UAE	Rapporteur
Mohamed Meziani Abdelkader	**MCA**	Univ. de Bejaia	Co-Rapporteur
Mohamed Reda Bekli	**MCA**	Univ. de Bejaia	Examinateur
Mustafa Moumni	**Prof**	Univ. de Batna 1	Examinateur
Nabil Baouche	**MCA**	Univ. de Jijel	Invité

Année Universitaire : **2024/2025**

مُلخص

في هذه الأطروحة، قمنا بالتحقيق من اقترانات بوزون هيغز على مستوى حد الشجرة HVV (مع $V = W, Z$) وذلك من خلال عدة حالات نهائية مختلفة في المصادمات اللبتونية. إن التحديد التجريبي لاشارات الإقترانات بين جسيمات النموذج المعياري (SM) والرنين السلمي عند 125GeV غير حاسم إلى حد كبير. ومع ذلك، فإن سعات هذه الإقترانات تتوافق وتتلائم بشكل عام مع بوزون هيغز للنموذج المعياري. في العديد من توسيعات النموذج المعياري، يمكن تعديل هذه الإقترانات على الشكل $g_{hVV} = \kappa_V g_{hVV}^{SM}$، وذلك من خلال المساهمات الإشعاعية أو بسبب الطبيعة المركبة للهيغز و\ أو البوزونات المعيارية. كخطوة أولى، نفترض أن إقترانات هيغز-البوزونات المعيارية هي شبيهة بالنموذج المعياري (SM-like) $\kappa_V = \pm 1$، نعتبر ثلاثة حالات نهائية في المصادمات اللبتونية المصادم الخطي الدولي (ILC): $h\nu\bar{\nu}$@250GeV، hW^+W^-@500GeV و ZW^+W^-@1TeV (حيث $h \to b\bar{b}$ و $Z \to jj$)، بهدف تحديد اشارات κ_V من خلال الانحرافات المحتملة في قيم المقطع العرضي مقارنة مع النمودج المعياري (SM). بعد ذلك، نفترض أنه لا يمكن ملاحظة مثل هذا الإنحراف في κ_V مقارنة مع النموذج المعياري في السطوع العالي للمصادم الهادروني الكبير HL-LHC ، أي $|\delta\kappa_V/\kappa_V| \approx 0.04 \sim 0.05$، نستكشف هذه العمليات الثلاثة في حالة الإشارة $|\kappa_V| = 1$ لتحليل توزيعات المتغيرات الحركية. قد يؤثر هذا الاستكشاف على قيم القطوع الفعالة والتوزيعات الحركية، ويمكن الإبلاغ عن الفائض الصغير أو عدم وجود أحداث.

كلمات مفتاحية: اقترانات هيغز- بوزونات المقياس، المصادم الخطي الدولي(ILC) ، إنتاج $h\nu\bar{\nu}$، إنتاج hW^+W^-، إنتاج ZW^+W^-.

Abstract

In this thesis, we investigate the tree-level Higgs couplings hVV (with $V = W, Z$) through various final states at leptonic colliders. The experimental determination of the signs of the couplings between the Standard Model (SM) particles and the scalar resonance at 125GeV is largely inconclusive. However, the magnitudes have generally aligned with the Higgs boson of the SM. In many SM extensions, these couplings could be modified as $g_{hVV} = \kappa_V g_{hVV}^{SM}$, either through radiative contributions or due to the composite nature of the Higgs and/or gauge bosons. As a first step, assuming that the Higgs-gauge couplings are SM-like ($\kappa_V = \pm 1$), we consider three final states at the leptonic collider International Linear Collider (ILC): $h\nu\bar{\nu}$@$250, \text{GeV}$, hW^+W^-, @500GeV, and ZW^+W^-@1TeV (with $h \to b\bar{b}$, $Z \to jj$, and $W^- \to \ell^-\bar{\nu}$), aiming to identify the signs of κ_V through possible deviations in cross-section values from the SM. Subsequently, assuming that such a deviation in κ_V with respect to the SM cannot be observed at HL-LHC, i.e., $|\delta\kappa_V/\kappa_V| \approx 0.04 \sim 0.05$, we explore these three processes in the signal case $|\kappa_V| = 1$ to analyze kinematic variables distributions. This exploration may impact the cross-section and kinematic distributions, and a tiny excess or lack of events could be reported.

Keywords: Higgs gauge-bosons couplings, ILC, $h\nu\bar{\nu}$ production, hW^+W^- production, ZW^+W^- production.

Résumé

Dans cette thèse, nous étudions les couplages de Higgs au niveau de l'arbre hVV (avec $V = W, Z$) à travers divers états finaux dans des collisionneurs leptoniques. La détermination expérimentale des signes des couplages entre les particules du Modèle Standard (SM) et la résonance scalaire à 125 GeV est largement peu concluante. Cependant, les magnitudes se sont généralement alignées sur le boson de Higgs du SM. Dans de nombreuses extensions SM, ces couplages pourraient être modifiés comme $g_{hVV} = \kappa_V g_{hVV}^{SM}$, soit par des contributions radiatives, soit en raison de la nature composite des bosons de Higgs et/ou de jauge. Dans un premier temps, en supposant que les couplages de jauge Higgs sont de type SM ($\kappa_V = \pm 1$), nous considérons trois états finaux au collisionneur leptonique International Linear Collider (ILC) : $h\nu\bar{\nu}$@250GeV, hW^+W^-@$500, \text{GeV}$ et ZW^+W^-@1TeV (avec $h \to b\bar{b}$, $Z \to jj$ et $W^- \to \ell^-\bar{\nu}$), visant à identifier les signes de κ_V à travers d'éventuels écarts dans les valeurs de section efficace par rapport au SM. Par la suite, en supposant qu'un tel écart de κ_V par rapport au SM ne puisse pas être observé au HL-LHC, c'est-à-dire $|\delta\kappa_V/\kappa_V| \approx 0.04 \sim 0.05$, nous explorons ces trois processus dans le cas du signal $|\kappa_V| = 1$ pour analyser les distributions des variables cinématiques. Cette exploration peut avoir un impact sur les distributions transversales et cinématiques, et un léger excès ou manque d'événements pourrait être signalé.

Mots clés: Couplages de Higgs-bosons de jauge, ILC, production $h\nu\bar{\nu}$, production hW^+W^-, production ZW^+W^-.

Acknowledgments

In the name of Allah, praise be to Allah, and peace and blessings be upon Muhammad, the Messenger of Allah, and upon those who followed him.

Through this thesis, I would like to extend my heartfelt thanks to everyone who contributed to the completion of this dissertation, whether directly or indirectly. I would like to begin by expressing my sincere gratitude to my supervisor, Professor Amine Ahriche, who was dedicated, responsible, and exceptionally helpful throughout the completion of the thesis. May Allah bless him and his knowledge. I would also like to warmly thank the assistant supervisor, Dr. Mohamed-Abdelkader Meziani, whose cooperation was effective and unconditional.

I express my sincere gratitude to Dr. Nadia Oulebsir for accepting to chair the examination committee, and I also extend my heartfelt thanks to Dr. Mohamed Reda Bekli, Dr. Nabil Baouche and Prof. Mustafa Moumni for accepting to be members of the examination committee as examiners.

Thanks are also due to all the professors who contributed to my reaching this stage, whether here at the University of Bejaia or at the University of Jijel during my undergraduate (bachelor's and master's) studies, as well as to all the professors outside the university. I also do not forget to thank every member of the respected family, each according to their position, as well as colleagues and friends.

Contents

List of Tables

List of Figures

Introduction

Following the discovery of the Higgs boson within the Standard Model (SM) with a mass of 125.18GeV [1, 2], accurately determining its properties is crucial for substantiating any potential new physics (NP) phenomena beyond the standard model (BSM). In particular, the determination of the hVV gauge couplings modifiers $\kappa_V = g_{hVV}/g_{hVV}^{SM}$ is crucial to extract information on the true nature of electroweak symmetry breaking (EWSB). Here, V stands for W and Z vector bosons; and g_{hVV} (g_{hVV}^{SM}) is the Higgs-gauge couplings in the considered model (SM). Although the Large Hadron Collider (LHC) was/is able to probe these Higgs-gauge couplings, the current results for any experimental deviation from the SM are still negative. Both the High-Luminosity LHC (HL-LHC) program and upcoming projects for high-energy leptonic/hadronic colliders are anticipated to achieve precise measurements of the Higgs-boson couplings to SM particles. The model-independent approach is among the most favored ones to look for BSM signatures, especially in extended Higgs sector where the Higgs couplings get modified with respect to the SM. The assumption that the Higgs scalar potential respects the residual global $SU(2)$ symmetry, called the custodial symmetry [3], after the EWSB, ensures the ρ parameter to be equal to 1; and the ratio $\lambda_{WZ} = \kappa_W/\kappa_Z$ should equal to 1 at tree level. From experimental searches [4–6], this ratio (λ_{WZ}) can generally be either positive or negative.

In many SM extensions, λ_{WZ} is exactly 1, however, it may deviate significantly from 1 for higher scalar representations SM extensions, where the hVV couplings may deviate also from their SM values. It's important to note that the values of both κ_V and λ_{WZ} can be examined through the decay rates of the Higgs, while the effects of tree-level/one-loop interference play a crucial role in determining the overall sign of λ_{WZ} [7–11]. As mentioned above the ratio λ_{WZ} could be different from 1, and the authors in [7] explained that when λ_{WZ} depends only on the custodial representation of h, there are two possible values: $\lambda_{WZ} = +1$ where h is a

singlet (as in the SM); and $\lambda_{WZ} = -1/2$ where h is a fiveplet like in the Georgi-Machacek (GM) model [12–15]. In [7, 16–19], a study into the ratio λ_{WZ} of coupling modifiers, demonstrated that λ_{WZ} could be measured (the amplitude and sign of λ_{WZ}) with approximately 10 % precision using the interference effects[1] via for example vector boson fusion (VBF), Higgs decays to four leptons, W^+W^-h production, and the combination of Zh and tH production. Fits to the couplings by the 13 TeV CMS analysis [20] did allow either sign, but the 13 TeV ATLAS analysis [21] did not consider negative values of λ_{WZ}. In some SM extensions with modified hVV couplings, excess in event numbers can be observed in some final states, and such improvements can appear in the distributions of kinematic variables.

Many studies have considered the anomalous couplings hVV in the framework of lepton/hadron colliders using Higgs effective field theory (EFT); and using a variety of observables that include kinematic distributions. One can cite the following: angular observables at e^-e^+ colliders; the sensitivity of the hW^+W^- production to possible anomalous Higgs couplings; investigation of the feasibility to measure anomalous couplings of the Higgs boson to electroweak gauge bosons and gluons, including CP-violating couplings at proton and lepton colliders [22–29]. Previous investigations of the anomalous hVV couplings were performed by both the CMS and ATLAS experiments and have shown an agreement with the SM predictions; and put some constraints that are still weak to allow for a significant BSM contribution [10, 11, 17, 30–39]. The possible precision in the measurements of κ_W and κ_Z at the HL-LHC with an integrated luminosity of 3 ab^{-1} , are expected to be $\delta\kappa_W/\kappa_W \leq 5\,\%$, $\delta\kappa_Z/\kappa_Z \leq 4\,\%$, respectively [40]. The relative precision measurement of the Higgs boson coupling to the vector bosons κ_V could be less than 0.5 % at all future lepton colliders [41], such as the International Linear Collider (ILC) [42, 43], the Compact Linear e^-e^+ Collider (CLIC) [44], Future Circular Collider (FCC-ee) [45], the Circular Electron Positron Collider (CEPC) [46] or Cool Copper Collider (C^3) [47] and for multi-TeV colliders the FCC-hh [48], SppC and Muon Collider. The ILC can run in a center of mass energies from 250 GeV to 1 TeV with luminosity up to $8\,ab^{-1}$ [49, 50]. It will be operating as a Higgs factory with a clean collider environment, fixed center of mass energy, attainability of polarized beam and large statistics, then the Higgs properties can be measured and the structure of the scalar sector can be identified. This thesis is organized as follows:

[1] Here, we mean tree-level interference effects between W and Z mediated processes i.e., $VV \to Vh$, $V = W, Z$, and also the interference between amplitudes at tree and one-loop levels as described in [7], while in this work, only tree-level processes that involve interference effects between W and Z are considered.

- Chapter 1: a brief explanation of the Standard Model, the Higgs mechanism, Higgs couplings and unanswered issues in the SM are discussed.

- Chapter 2: outline of particle colliders in general, followed by an extensive description of the international leptonic collider (ILC).

- Chapter 3: the investigation of the effect of the hVV couplings modifications on the processes $h\nu\bar{\nu}$ @ 250 GeV, hW^+W^- @ 500 GeV and ZW^+W^- @ 1 TeV (with $h \to b\bar{b}$, $Z \to jj$ and $W^- \to \ell^-\bar{\nu}$) at e^-e^+ colliders for both unpolarized and polarized beams ($P_{e^-,e^+} = [-0.8, +0.3]$); where ℓ denotes an electron or muon. We try to identify the $\kappa_W \equiv hWW$ and $\kappa_Z \equiv hZZ$ couplings sign by considering different recent combined measurements of the LHC Run-II [20, 21, 39, 51]. Then by taking into account the SM-like signal scenario $\kappa_V = 1$, we analyzed the signal processes $b\bar{b} + \not{E}_T$ @ 250 GeV, $hW^+W^- \to b\bar{b} + \ell^+\ell^- + \not{E}_T$ @ 500 GeV; and $ZW^+W^- \to jj + \ell^+\ell^- + \not{E}_T$ @ 1 TeV at an e^-e^+ colliders with unpolarized beams $P_{e^-,e^+} = [0, 0]$.

Conclusions are presented at the end of the thesis.

Chapter 1

The standard model of particle physics

The standard model of particle physics is the most successful and certain description of elementary particle physics to date. It is formulated within the framework of Quantum Field Theory (QFT), which combines principles from quantum mechanics and special relativity to explain the interactions of elementary particles, these interactions are mediated by the electroweak force [52–55] and strong force [56–59, 88]. The SM excludes interactions caused by gravity. We will give a brief summary of the SM in the following. The most widely applicable renormalisable QFT is the SM, and it has a field content that corresponds to the observable particles and is invariant under gauge symmetry

$$\mathrm{SU}(3)_{\mathrm{C}} \otimes \mathrm{SU}(2)_{\mathrm{L}} \otimes \mathrm{U}(1)_{\mathrm{Y}}\,, \tag{1.1}$$

with $\mathrm{SU}(3)_{\mathrm{C}}$ is the gauge group of quantum chromodynamics (QCD) operating on fields with colour charge, while $\mathrm{SU}(2)_{\mathrm{L}} \otimes \mathrm{U}(1)_{\mathrm{L}}$ is the EW gauge group operating on left chiral fields and fields carrying hypercharge (Y). The field content of the SM consists of fermions with spin 1/2, gauge bosons with spin 1, and a single spin 0 boson. Each of the above gauge symmetries has a unique gauge field that corresponds to it: the gluon field G^a_μ of QCD, the $\mathrm{SU}(2)_L$ gauge field W^a_μ, and the $\mathrm{U}(1)_Y$ gauge field B_μ, where a is the index of the gauge representation. All SM fermions are Dirac fermions with left- and right-handed chiralities. Under $\mathrm{SU}(2)_L$, the right-handed fields are singlets whereas the left-handed fields are doublets. Right-handed neutrinos are not introduced into the SM, because it considers neutrinos (which are known

Fermions (Spin 1/2)				Gauge Bosons (Spin 1)		Higgs (Spin 0)
Generation	1	2	3	Interaction	Boson	
Leptons	e	μ	τ	Strong	g	Scalar boson H
	ν_e	ν_μ	ν_τ			
Quarks	u	c	t	Weak	W	
	d	s	b		Z	
				EM	γ	

Table 1.1: Table summarizing an overview of the Standard Model particles content with their matter particles.

to be massive) as massless particles. However, because the neutrino masses are constrained to be so tiny, considering them as massless particles is sufficient for our purposes.

1.1 The fundamental particles

The Higgs boson discovery in July 2012, was the last piece of SM point particles, these particles have some basic properties: spin, charge and mass. The spin can only take integer or half-integer values, which is used to classify particles into two categories: bosons (integer spin) and fermions (half-integer spin) which is also the matter and anti-matter particles described by the SM. The SM successfully combines three out of four interactions known in nature: the weak, the strong, the electromagnetic and the gravitation interactions. Gravity differs from all other interactions and is not integrated into the SM. All spin-1 particles are considered to be force carriers. The gluons are the force carriers of the strong force, discovered at DESY collider in 1979 [60]. The Z and W bosons are the force carriers of the weak force and they lead to $\beta-$nuclear decay. They were discovered in 1983 at the $Sp\bar{p}S$ collider at CERN [61–63]. The photon is the force carrier of the electromagnetic force, and it was introduced by Albert Einstein to describe the observation of the photoelectric effect [64]. The structure of fermionic fields, Bosonic fields and the Higgs scalar field are listed in table (1.1). The coupling strength of a particle is determined by its charge. As a result, each force has a unique charge. The strong force only between colour charges, the weak force only between weak isospins, and the EM force only between electric charges. For each fermion, there is an antifermion with the same quantum numbers but opposing additive quantum numbers, and hence opposite charges for all three forces.

1.2 The Standard Model structure

The weak and electromagnetic interactions between leptons and quarks are described by the electroweak theory by Glashow-Weinberg-Salam, that is a Yang–Mills theory based on the symmetry group $\mathrm{SU}(2)_L \otimes \mathrm{U}(1)_Y$, while the strong interactions (or QCD) between quarks is a non commutative colour theory for quarks.

1.2.1 The Electroweak Lagrangian

The empirical facts, the $\mathrm{SU}(2)_L \otimes \mathrm{U}(1)_Y$ family structure of the fermions, the Gell-Mann-Nishijima relation and the existence of vector bosons allow puting the formulation of the SM in the phenomenological basis. The electroweak Lagrangian is split into four different parts according to the general principles of constructing gauge-invariant field theory with spontaneous symmetry breaking

$$\mathcal{L}_{EW} = \mathcal{L}_{Gauge} + \mathcal{L}_{Fermion} + \mathcal{L}_{Higgs} + \mathcal{L}_{Yukawa}, \tag{1.2}$$

where $\mathcal{L}_{Gauge}$ describes the pure gauge field Lagrangian in the rules of the non-Abelian case

$$\mathcal{L}_{Gauge} = -\frac{1}{4} W^a_{\mu\nu} W^{\mu\nu,\,a} - \frac{1}{4} B_{\mu\nu} B^{\mu\nu}, \tag{1.3}$$

the isotriplet $W^a_{\mu\nu}$, $a = 1, 2, 3,$ is a triplet of vector fields $W^\alpha_{\mu\nu}$ with the isospin operators I_1, I_2, I_3 and the isosinglet B_μ is a singlet field with the hypercharge Y (I and Y are generalized charges of the non-Abelian $\mathrm{SU}(2) \otimes \mathrm{U}(1)$ groupe) lead to the field strenght tensors

$$\begin{aligned} W^a_{\mu\nu} &= \partial_\mu W^a_\nu - \partial_\nu W^a_\mu + g \epsilon_{abc} W^b_\mu W^c_\nu, \\ B_{\mu\nu} &= \partial_\mu B_\nu - \partial_\nu B_\mu, \end{aligned} \tag{1.4}$$

g denotes the non-abelian $SU(2)$ gauge coupling constant and g' the Abelian $U(1)$ coupling. In eq. (1.2) $\mathcal{L}_{Fermion}$ represents the kinetic term for the SM fermions. The interaction of the gauge bosons and the fermions are generated through the gauge covariant derivative

$$D_\mu = \partial_\mu - i g I_a W^a_\mu + i g' \frac{Y}{2} B_\mu. \tag{1.5}$$

The right-handed fermion fields of each lepton and quark family are grouped into singlets

$$e_{Rj} = \overline{e_{Rj}},\ u_{Rj} = \overline{u_{Rj}},\ d_{Rj} = \overline{d_{Rj}},\ \psi_R = \frac{1+\gamma_5}{2}\psi, \tag{1.6}$$

while the left-handed ones are grouped into SU(2) doublets

$$L_j = \begin{pmatrix} \nu_e \\ e^- \end{pmatrix}_L,\ Q_j = \begin{pmatrix} u \\ d \end{pmatrix}_L,\ \psi_L = \frac{1-\gamma_5}{2}\psi, \tag{1.7}$$

where the subscript j runs over the three generations of fermions and ψ are the chiral fields. The connection between the hypercharge Y, the electric charge Q and the third component of the weak isospin I_3 is valid by the Gell–Mann-Nishijima relation

$$Q = I_3 + \frac{Y}{2}. \tag{1.8}$$

The corresponding values of the third component of the isospin I_3, Y, and Q are listed in table (1.2). The left-handed down-type quarks (d', s', b'), are related to their mass eigenstates (d, s, b), by the Cabibbo-Kobayashi-Maskawa (CKM) mixing matrix [65, 66] according to $d'_i = \sum_{ij} V_{ij}^{CKM} d_j$. The gauge group $\mathrm{SU}(2)_L \otimes \mathrm{U}(1)_Y$ has four generators, three for which are

Fermions type		I_3	Y	Q
Leptons	$\begin{pmatrix} e \\ \nu_e \end{pmatrix}_L$ $\begin{pmatrix} \mu \\ \nu_\mu \end{pmatrix}_L$ $\begin{pmatrix} \tau \\ \nu_\tau \end{pmatrix}_L$	$-1/2$ $1/2$	$-1/2$ $-1/2$	-1 0
	e_R μ_R τ_R	0	-1	-1
	$\nu_{e,R}$ $\nu_{\mu,R}$ $\nu_{\tau,R}$	0	0	0
Quarks	$\begin{pmatrix} u \\ d' \end{pmatrix}_L$ $\begin{pmatrix} c \\ s' \end{pmatrix}_L$ $\begin{pmatrix} t \\ b' \end{pmatrix}_L$	$1/2$ $-1/2$	$1/6$ $1/6$	$2/3$ $-1/3$
	u_R c_R t_R	0	$2/3$	$2/3$
	d_R s_R b_R	0	$-1/3$	$-1/3$

Table 1.2: Quantum numbers of leptons and quarks. The third component of the weak isospin I_3, the weak hypercharge Y and the electric charge Q.

the iosospin operators T^a ($a = 1, 2, 3$) and the other one is the hypercharge Y. Each of these operators corresponts to a vector field, $T^{1,2,3}$ corresponds to $W_\mu^{1,2,3}$ and Y corresponts to B_μ. The group $\mathrm{SU}(2)_L$ non-Abelian because its generators do not commute in general

$$[T_a, T_b] = i\epsilon_{abc} T_c, \tag{1.9}$$

where ϵ_{abc} is the antisymetric tensor, while the $U(1)_Y$ group is Abelian $[Y, Y] = 0$. The generators T^a are related to Pauli matrices by

$$T^a = \frac{1}{2}\tau^a,\ \tau^1 = \begin{pmatrix} 0 & 1 \\ 1 & 0 \end{pmatrix},\ \tau^2 = \begin{pmatrix} 0 & -i \\ i & 0 \end{pmatrix},\ \tau^3 = \begin{pmatrix} 1 & 0 \\ 0 & -1 \end{pmatrix}. \tag{1.10}$$

The SM Lagrangian for fermions, neglecting mass terms, is then given by

$$\mathcal{L}_F = \overline{L_j} i D_\mu \gamma^\mu L_j + \overline{e_{Rj}} i D_\mu \gamma^\mu e_{Rj} + \overline{Q_j} i D_\mu \gamma^\mu Q_j + \overline{u_{Rj}} i D_\mu \gamma^\mu u_{Rj} + \overline{d_{Rj}} i D_\mu \gamma^\mu d_{Rj}, \tag{1.11}$$

where γ^μ is the Dirac matrices.

1.2.2 Fermions and the Vector bosons interaction

The interaction term is phrased in terms of electromagnetic, charged and neutral current of each fermion field ψ_f

$$\mathcal{L}_{int} = -e\left\{A_\mu J^\mu_{em} + \frac{1}{\sqrt{2}\sin\theta_W}\left(W^+_\mu J^\mu_{cc} + W^-_\mu J^{\mu\,\dagger}_{cc}\right) + \frac{1}{\sin\theta_W \cos\theta_W} Z_\mu J^\mu_{nc}\right\}, \tag{1.12}$$

with

$$J^\mu_{em} = \bar{\psi}_f \gamma^\mu \left(T_3 + Y\right)\psi_f \tag{1.13}$$

$$J^\mu_{cc} = \bar{\psi}_f \gamma^\mu \left(T_1 + iT_2\right)\psi_f \tag{1.14}$$

$$J^\mu_{nc} = \bar{\psi}_f \gamma^\mu T_3 \psi_f - \sin^2\theta_W J^\mu_{em}, \tag{1.15}$$

where the electrical charge is identified with $Q = T_3 + Y$. The charged current term describes W boson production and decay into chiral fermions

$$J^\mu_{cc} = \frac{1}{2}\bar{\psi}_f \gamma^\mu \left(1 - \gamma^5\right)\psi_f. \tag{1.16}$$

The neutral current is usually written in a more general way to split vector and axial-vector currents

$$J^\mu_{nc} = \frac{1}{2}\bar{\psi}_f \left(g^f_V \gamma^\mu - g^f_A \gamma^\mu \gamma^5\right)\psi_f, \tag{1.17}$$

with the coupling constants

$$g_V^f = T_3 - 2Q\sin^2\theta_W \tag{1.18}$$

$$g_A^f = T_3, \tag{1.19}$$

where Y and T_3 denote the hypercharge and the third isospin component of the weak isospin (see the table (1.2)).

1.2.2.1 The Higgs mechanism

In the Glashow-Weinberg-Salam theory [67], which unifies the electromagnetic interaction and weak interaction, the application of Higgs mechanism appears. Electroweak symmetry breaking of $\mathrm{SU}(2)_L \otimes \mathrm{U}(1)_Y$, which leaves the $U(1)_{EM}$ unbroken and provides non-zero masses to the weak vector bosons Z and $W^{\pm}$ while quarks and leptons get their masses via Yukawa interactions. To explain the Higgs mechanism, a complex scalar field ϕ, is introduced with massless vector fields and produce a real scalar field and massive vector fields without breaking the gauge invariance of the Lagrangian density. The Higgs Lagrangian reads

$$\mathcal{L}_{\text{Higgs}} = \left(D_\mu \phi\right)^+ \left(D^\mu \phi\right) - V\left(\phi\right), \tag{1.20}$$

where

$$\phi\left(x\right) = \begin{pmatrix} \phi^+\left(x\right) \\ \phi^0\left(x\right) \end{pmatrix} \tag{1.21}$$

is a doublet of complex scalar fields with hypercharge $Y = 1$ and four degrees of freedom. The covariant derivative D_μ defined in eq. (1.5) takes into account the kinetic part of the field and its interaction with the gauge bosons, while $V\left(\phi\right)$ is the Higgs potential

$$V\left(\phi\right) = \mu^2 \phi^+ \phi + \frac{\lambda^2}{2}\left(\phi^+ \phi\right)^2, \tag{1.22}$$

where the Higgs self coupling $\lambda > 0$ in order to put a lower bound on the potential. For the case $\mu^2 > 0$ there is a unique vacuum state which is the minimum of the potential at $< 0|\phi|0 > \equiv \phi_0 = 0$, while μ^2 must be less than zero $\left(\mu^2 < 0\right)$ in order to have electroweak

breaking and the minimum of the potential (shown in Fig. 1.1) will be at

$$< \phi >_0 \equiv < 0|\phi|0 >= \sqrt{-\frac{\mu^2}{2\lambda}}, \tag{1.23}$$

The vacuum expectation value (v.e.v) is not zero $v = \sqrt{-\mu^2/\lambda}$ which leaves the potential

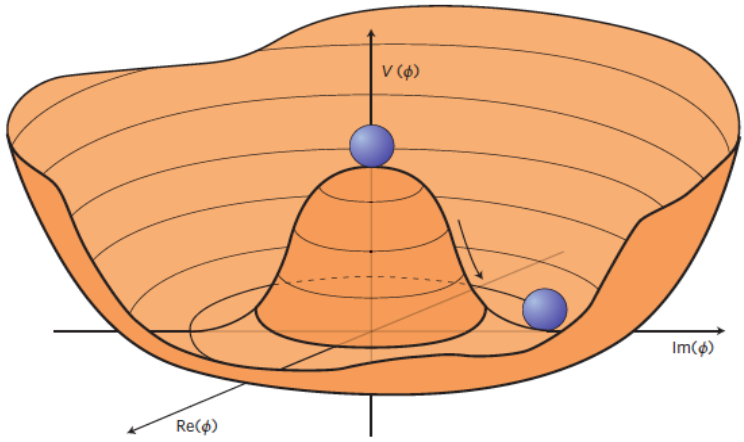

Figure 1.1: The Higgs potential as shown in eq. (1.22) with $\mu^2 < 0$, in which case the minimum is at $< \phi >_0 = \sqrt{-\frac{\mu^2}{2\lambda}}$. Choosing any of the points at the bottom of the potential breaks spontaneously the rotational $U(1)$ symmetry.

symmetric around zero in real-imaginary plan Fig.(1.1) requiring spontaneouse breaking of symmetry. The vacuum for the charged component (in eq. (1.21)) has been set to zero, since the exact electromagnetic symmetry needs to be preserved. We can write the Higgs field in the unitary gauge as[1]

$$\phi(x) = \frac{1}{\sqrt{2}} \begin{pmatrix} 0 \\ \upsilon + H(x) \end{pmatrix}, \tag{1.24}$$

where $H(x)$ is the physical Higgs scalar field. Now we can write the Higgs Lagrangian as

$$\begin{aligned} \mathcal{L}_{\text{Higgs}} = & \frac{1}{2}(\partial_\mu H)^2 + \frac{g^2}{8}(\upsilon + H)^2 \left(W_\mu^1 - iW_\mu^2\right)\left(W^{\mu 1} + iW^{\mu 2}\right) \\ & + \frac{1}{8}(\upsilon + H)^2 \left(gW_\mu^3 - g' B_\mu\right)^2 - \lambda \upsilon^2 H^2 - \lambda \upsilon H^3 - \frac{\lambda}{4} H^4. \end{aligned} \tag{1.25}$$

[1]Since the vacuum is neutral, then one must have ($I = \frac{1}{2}$, $I_3 = -\frac{1}{2}$), and as $Q = I_3 + \frac{1}{2}Y$, the choice that $Y = 1$ breaks the EW gauge symmetry.

The physical fields A_μ, Z_μ and $W_\mu^\pm$ are correlated by

$$W_\mu^\pm = \frac{W_\mu^1 \mp W_\mu^2}{\sqrt{2}} \tag{1.26}$$

$$Z_\mu = \frac{gW_\mu^3 - g^{'}B_\mu}{\sqrt{g^2 + g^{'2}}} = \cos\theta_W W_\mu^3 - \sin\theta_W B_\mu \tag{1.27}$$

$$A_\mu = \frac{g^{'}W_\mu^3 + gB_\mu}{\sqrt{g^2 + g^{'2}}} = \sin\theta_W W_\mu^3 + \cos\theta_W B_\mu, \tag{1.28}$$

with the weak mixing angle θ_W defined by

$$\cos\theta_W = \frac{g}{\sqrt{g^2 + g^{'2}}}. \tag{1.29}$$

By simplification of the Lagrangian eq. (1.25) it will become

$$\begin{aligned}\mathcal{L}_{\text{Higgs}} = \frac{1}{2}(\partial_\mu H)^2 - \lambda\upsilon^2 H^2 - \lambda\upsilon H^3 - \frac{\lambda}{4}H^4 - \frac{g^2\upsilon^2}{4}W_\mu^+ W^{-\mu} + \frac{\left(g^2 + g^{'2}\right)\upsilon^2}{8}Z_\mu Z^\mu \\ + \frac{g^2\upsilon}{2}HW_\mu^+ W^{-\mu} + \frac{g^2}{4}H^2 W_\mu^+ W^{-\mu} + \frac{\left(g^2 + g^{'2}\right)\upsilon}{4}HZ_\mu Z^\mu + \frac{\left(g^2 + g^{'2}\right)}{8}H^2 Z_\mu Z^\mu.\end{aligned} \tag{1.30}$$

The Lagrangian eq. (1.30) contains the mass terms for the gauge fields, that can be expressed in terms of the fields $W^\pm$ and Z, so

$$m_W = \frac{g\upsilon}{2}, \quad m_Z = \frac{g\upsilon}{2\cos\theta_W} = \frac{m_W}{\cos\theta_W}, \tag{1.31}$$

the photon field A_μ is massless since no quadratic term in the photon field appears. The Higgs boson mass is given by

$$m_H = \sqrt{2\lambda\upsilon^2}. \tag{1.32}$$

The mass of the $W^\pm$ could also expressed via the Fermi constant, where they are related at lowest order as

$$\upsilon = \frac{1}{\left(\sqrt{2}G_F\right)^{1/2}} \approx 246\,GeV. \tag{1.33}$$

The Feynman diagrams for the interaction vertices of the Higgs boson shown in Fig. (1.2). The Higgs boson coupling to fermions and gauge bosons Hff, HVV and $HHVV$ are directly

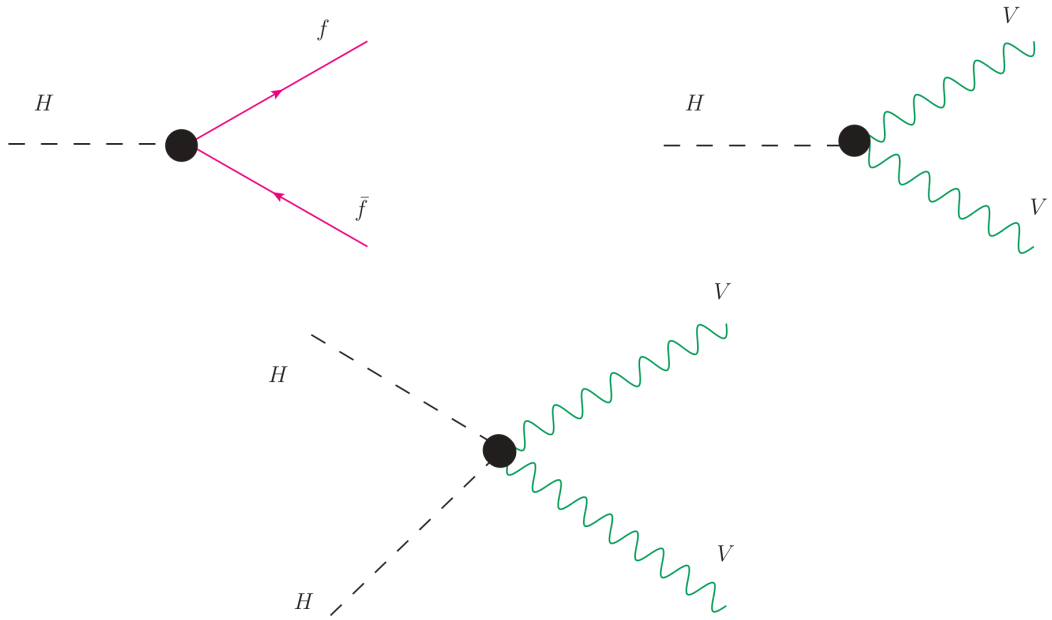

Figure 1.2: Higgs boson couplings to fermions f and gauge bosons $V = W$, Z are depicted in lowest order Feynman diagrams.

linked to their masses with Feynman rules being given by

$$g_{Hff} = i\frac{m_f}{\upsilon},\ g_{HVV} = 2i\frac{m_V^2}{\upsilon}, g_{HHVV} = \frac{g_{HVV}}{\upsilon}. \tag{1.34}$$

Furthermore, eq. (1.30) indicates that the Higgs boson has triple and quartic self-interactions with corresponding Feynman rules

$$g_{HHH} = -3i\frac{m_H^2}{\upsilon},\ g_{HHHH} = \frac{g_{HHH}}{\upsilon}. \tag{1.35}$$

1.2.2.2 Yukawa Lagrangian

The fermionic mass term that could combine chiral left-handed and right-handed compenents are given by

$$m\psi\psi = m\left(\bar{\psi}_R\psi_L + \bar{\psi}_L\psi_R\right), \tag{1.36}$$

this part (eq. (1.36)) is not invariant under local symmetry $\mathrm{SU}(2)_L \otimes \mathrm{U}(1)_Y$. For this reason, this mass term is removed from the Lagrangian before symmetry spontaneouse breaking (SSB). In order to restore it via SSB, we introduce an interaction between the fermions and

the Higgs field through the Yukawa Lagrangian

$$\mathcal{L}_{Yuk} = -\lambda_{e_i}\bar{L}_i\Phi e_{R_i} - \lambda_{d_i}\bar{Q}_i\Phi d_{R_i} - \lambda_{u_i}\bar{Q}_i\tilde{\Phi}u_{R_i} + h.c., \tag{1.37}$$

where $\lambda_{e_i}, \lambda_{d_i}$ and λ_{u_i} are the Yukawa coupling constants for Leptons, down-type quarks d_i and up-type quarks u_i with $i = 1, 2, 3$ and $\tilde{\Phi} = i\tau_2\Phi^*$ (h.c. denotes the hermitian conjugate). For example the first fermion family reads

$$\mathcal{L}^1_{Yuk} = -\lambda_e\bar{L}_1\Phi e_R - \lambda_d\bar{Q}_1\Phi d_{R_1} - \lambda_u\bar{Q}_1\tilde{\Phi}u_{R_1} + h.c., \tag{1.38}$$

substituting we obtain

$$\begin{aligned}\mathcal{L}^1_{Yuk} = &-\frac{\lambda_e}{\sqrt{2}}\left(\bar{\nu_e}, \bar{e}_L\right)\begin{pmatrix} 0 \\ \upsilon + H \end{pmatrix} e_R - \frac{\lambda_d}{\sqrt{2}}\left(\bar{u}_L, \bar{d}_L\right)\begin{pmatrix} 0 \\ \upsilon + H \end{pmatrix} d_R \\ &- \frac{\lambda_u}{\sqrt{2}}\left(\bar{u}_L, \bar{d}_L\right)\begin{pmatrix} \upsilon + H \\ 0 \end{pmatrix} u_{R_1} + h.c.,\end{aligned} \tag{1.39}$$

inserting the h.c. term and simplifing using eq. (1.36) we write[2]

$$\mathcal{L}^1_{Yuk} = -\frac{\lambda_e}{\sqrt{2}}\left[\upsilon\bar{e}e + \bar{e}eH\right] - \frac{\lambda_u}{\sqrt{2}}\left[\upsilon\bar{u}u + \bar{u}uH\right] + \ldots, \tag{1.40}$$

so that the masses of the electrons and up-type quarks are given by

$$m_e = \frac{\lambda_e\upsilon}{\sqrt{2}},\ m_u = \frac{\lambda_u\upsilon}{\sqrt{2}},\ m_d = \frac{\lambda_d\upsilon}{\sqrt{2}}. \tag{1.41}$$

By spontaneously breaking the $\mathrm{SU}(2)_L \otimes \mathrm{U}(1)_Y$ gauge symmetry while maintaining the electromagnetic $U(1)_Q$ symmetry and the $SU(3)_C$ colour symmetry, the same isodoublet Φ generates the masses of fermions and weak vector bosons $W^{\pm}$ and Z. A gauge invariant $\mathrm{SU}(3)_C \otimes \mathrm{SU}(2)_L \otimes \mathrm{U}(1)_Y$ symmetry serves as the foundation of the SM. Contrary to the initial formulation of the SM, observations of neutrino flavour oscillations [68] conclusively demonstrate that neutrinos are not massless particles. Neutrinos masses can be treated on

[2] In general case $\mathcal{L}_{Yuk}$ reads

$$\mathcal{L}_{Yuk} = -\frac{\lambda_\ell}{\sqrt{2}}\left[\upsilon\bar{\ell}\ell + \bar{\ell}\ell H\right] - \frac{\lambda_q}{\sqrt{2}}\left[\upsilon\bar{q}q + \bar{q}qH\right],$$

with $\ell = e, \mu, \tau$, by considering the neutrinos are massless, $q = u, d, c, s, t, b$.

Hadrons	symbol	name	charge	quark components	mass (GeV)	spin
	p	proton	$+1$	uud	0.938	$\frac{1}{2}$
	$\bar{p}$	antiproton	-1	$\bar{u}\bar{u}\bar{d}$	0.938	$\frac{1}{2}$
Baryons	n	neutron	0	udd	0.940	$\frac{1}{2}$
	λ^0	lambda	0	uds	1.116	$\frac{1}{2}$
	Ω^-	omega	-1	sss	1.672	$\frac{3}{2}$
	π^+	pion	$+1$	$u\bar{d}$	0.14	0
	K^-	kaon	-1	$s\bar{u}$	0.494	0
Mesons	ρ^+	rho	$+1$	$u\bar{d}$	0.776	1
	B^0	B	0	$d\bar{b}$	5.297	0
	η_c	Eta	0	$c\bar{c}$	2.98	0

Table 1.3: Examples of Baryons and Mesons and some of their properties.

the same footing as charged leptons in the formalism mentioned above. Similar to quarks, the neutrinos are not mass eigenstates. For this we add Majorana Lagrangian given by

$$\mathcal{L}_{Majorana} = -m_M \left(\bar{\psi^c}_{\nu,\,L}\psi_{\nu,\,L} + h.c\right) \tag{1.42}$$

However, this contribution does not conserve lepton number and result in a neutrino-less double beta decay, a process which has thus far not been observed [69].

1.2.3 Strong interactions sector

In the SM, strong interactions of quark field ψ_q and gluon field G_μ are described by the following Lagrangian term

$$\mathcal{L}_{Colour} = -\frac{1}{4}F_a^{\mu\nu}F^a_{\mu\nu} + \sum_q i\bar{\psi}_{q,j}\gamma^\mu\left(\partial_\mu - ig''G^a_\mu\frac{\lambda_a}{2}\right)\psi_{q,k}\,, \tag{1.43}$$

where $a = 1, ..., 8$, and $j, k = 1, 2, 3$ indicate the colour indices for gluons and quarks, respectively. The sum extends over all quarks u, d, s, c, t, b which are indicated in the table (1.3)

The gauge field strength of the gluon field G_μ is given by

$$F^a_{\mu\nu} = \partial_\mu G^a_\nu - \partial_\nu G^a_\mu - g'' f^{abc}G^b_\mu G^c_\nu, \tag{1.44}$$

while g'' is the $SU(3)$ coupling parameter and the factors f^{abc} are the $SU(3)$ structure constants whose values are real and totally antisymmetric as shown in the table (1.4)

abc	123	147	156	246	257	345	367	458	678
f^{abc}	1	$\frac{1}{2}$	$-\frac{1}{2}$	$\frac{1}{2}$	$\frac{1}{2}$	$\frac{1}{2}$	$-\frac{1}{2}$	$\frac{\sqrt{3}}{2}$	$\frac{\sqrt{3}}{2}$

Table 1.4: The numerical values of the $SU(3)$ structure constants.

The λ_a matrices (the Gell-Mann matrices) denote the three-dimensional representation of the group generators $T_a = \frac{\lambda_a}{2}$ of $SU(3)$. They satisfy the relations

$$\begin{cases} \lambda_a = \lambda_a^+, \\ Tr\left(\lambda_a \lambda_b\right) = 2\delta_{ab}, \\ Tr\left(\lambda_a\right) = 0, \\ \left[\lambda_a, \lambda_b\right] = i f^{abc} \frac{\lambda_c}{2}. \end{cases} \tag{1.45}$$

The strong coupling constant is $\alpha_s = g''^2/4\pi$. The running of α_s is the most interesting property of Quantum Chromodynamics (QCD) [70] when virtual corrections resulting from the gluon field are taken into account, renormalized strong coupling depends on momentum-transfer scale q such that, at leading order

$$\alpha_s\left(q^2\right) = \frac{12\pi}{(33 - 2n_f)\log\left(q^2/\Lambda_{QCD}^2\right)}, \tag{1.46}$$

where Λ_{QCD} is the QCD energy scale and n_f is the number of quark flavours with quark masses lower than q^2. This means that the value of α_s decreases with increasing q^2. This effect is known as asymptotic freedom.

1.3 Open issues in the SM

The SM has been well verified with a large number of experimental observations, including: the discovery of the electron anti-neutrino in 1956 [71], the discovery of the muon neutrino in 1962, and the experimental discovery of Up, Down and strange quarks in 1968 at the SLAC Electron Collider. The prediction of the SM and experimental measurements agree with regard to the presence of charged and neutral currents that contributed to the unification of the electromagnetic and weak forces in a single force, the electroweak force established in the theory of Abdus Salam, Glashaw and Weinberg in 1973. After the experimental proof of these currents in CERN [72], the three obtained The Nobel Prize in 1979. The discovery

of the tau by Martin Perl in 1975 at SLAC, the discovery of gluons, which are the bosons responsible for the mediation of the strong nuclear force, were discovered in 1979 in the DESY laboratory in Germany. The discovery of the W and Z bosons was during a series of experiments made possible by Carlo Rubbia and Simon van der Meer at the $Sp\bar{p}S$ collider at CERN in 1983 [61–63]. While a large number of experimental discoveries agree very well with the SM, there are several signs that there must be physics beyond the SM. In this section, we provide brief summaries of a few particle physics unsolved problems that cannot be resolved within the SM.

1.3.1 Hierarchy problem

This arises from the large discrepancy between the weak and gravitational forces. Specifically, the weak force is about 10^{24} times stronger than gravity, despite the fact that both forces are thought to arise from the same fundamental interactions between particles. One proposed solution to the hierarchy problem is the theory of supersymmetry, which posits the existence of a new class of particles called superpartners. These particles are thought to be associated with the known particles of the SM, but with different spin values. Supersymmetry predicts that each known particle has a superpartner, and that these superpartners could explain the relative weakness of gravity compared to the weak force. Another proposed solution to the hierarchy problem is the theory of extra dimensions, which suggests that there may be additional dimensions of space beyond the three dimensions that we observe. In this theory, the weakness of gravity compared to the weak force could be explained by the fact that gravity is diluted across these extra dimensions, while the other forces are confined to our three-dimensional space. Despite these proposed solutions, the hierarchy problem remains one of the major theoretical challenges facing particle physicists today. It is likely that future experimental data, as well as advances in theoretical physics, will be needed to fully understand this issue.

1.3.2 Vacuum Stability in the SM

At tree-level, it can be observed that the scalar potential of the SM, as represented by eq. (1.22), has just one minimum, up to physically equivalent minima related by gauge transformations. upon extending the model to high scales, this behaviour may be altered due to the effect of the running of the quartic Higgs coupling λ, as delineated in ref. [73–86,89,90].

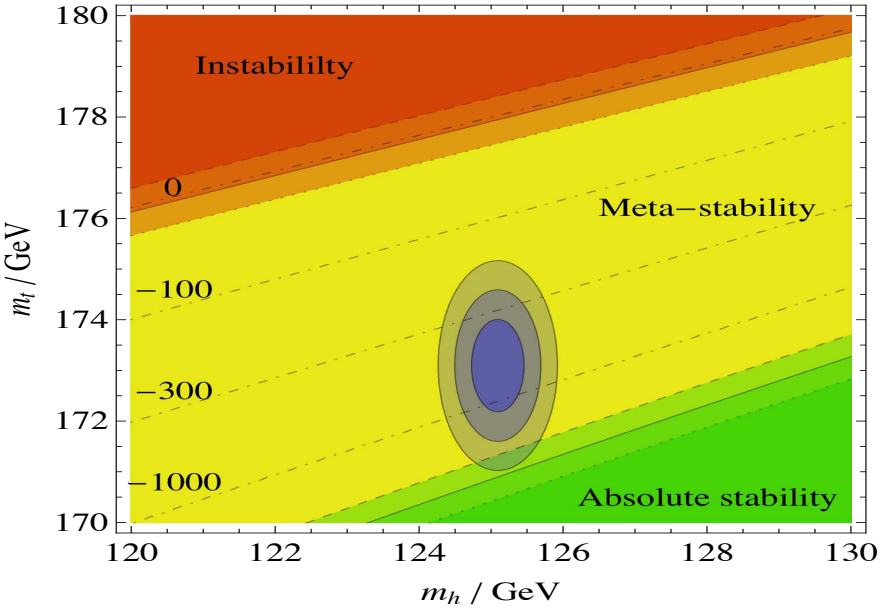

Figure 1.3: Top-quark and Higgs mass plane stability of the SM, from ref. [86]. The regions around the most recent measured values are shown by the blue ellipses at 1σ, 2σ, and 3σ. The labelled dashed lines roughly depict the log_{10} of the ratio between the universe's age and the EW vacuum's lifetime.

According to current theoretical predictions and experimental inputs of the top-quark mass, Higgs boson mass and strong coupling constant the EW vacuum of the SM is no longer the global minimum of the scalar potential for energy of order $10^{10}\,GeV$. If the EW vacuum is not the scalar potential's global minimum, the vacuum may tunnel into a minimum where the Higgs vev assumes a favourable value in terms of energy. The initial calculations for the lifetime of such a tunnelling process were made in [87], while the most recent calculations for the SM found lifetimes of around $\sim 10^{139}$ yrs [89]. In comparison to the age of the the universe, this lifetime is incredibly long. As a result, at these energy scales, the EW vacuum of the SM is metastable, it is not the global minimum, but it has a long enough lifetime to be practical. According to Fig. (1.3), this result is extremely sensitive to parametric uncertainties from the top-quark mass, the Higgs mass, and the strong coupling constant. The current observations are still consistent with the SM being completely stable, i.e. the EW vacuum being the global minimum of the scalar potential up to the Planck scale, within the 3σ bands for these uncertainties. On the other hand, a short-lived instability of the SM is incompatible with current measurements. Therefore, vacuum stability is not a major issue for the SM. Metastability is completely acceptable from an observational perspective. These results, however, are only valid if there is absolutely no NP below the Planck scale.

The vacuum stability behaviour in BSM theories that include NP at smaller scales may be entirely different. Vacuum stability is, therefore, not a critical issue of the SM.

1.3.3 Baryon asymmetry

Why is there more matter than antimatter in the universe? The SM predicts that matter and antimatter should have been created in equal amounts during the Big Bang[3], but observations of the universe today show that it is made up of matter, with only small amounts of antimatter. According to the SM, when particles and antiparticles come into contact, they annihilate each other and release energy. The reason for this baryon asymmetry is not yet understood, there are several proposed mechanisms for baryogenesis, including the electroweak baryogenesis, leptogenesis, and GUT baryogenesis. These theories involve various physical processes, such as the decay of heavy particles, the production of baryon number through interactions between particles and fields, and the violation of CP symmetry, which describes the behavior of particles and antiparticles under the combined operations of charge conjugation (C) and parity (P) inversion. The SM predicts that CP symmetry should be conserved, but experimental observations have shown that this is not the case. By assuming that all CMB photons are the result of thermal annihilations of baryons, it is possible to determine the universe's matter-antimatter asymmetry from the baryon to photon ratio

$$\left.\frac{N_b - N_{\bar{b}}}{N_b + N_{\bar{b}}}\right|_{T \gtrsim 1\,GeV} \approx \eta = \left.\frac{N_b}{N_\gamma}\right|_{\text{todady}} \sim 6 \times 10^{-10},$$

where the numerical value is obtained from CMB measurements [91]. No matter is expected to survive thermal annihilations in the absence of a baryogenesis theory that results in a matter-antimatter asymmetry. This ratio needs to be explained by a baryogenesis theory that satisfies the three Sakharov criteria [92] of baryon number violation, C and CP violation, and departure from thermal equilibrium in the early universe.

1.3.4 The dark matter

The majority of the universe may not be made of the same type of matter as the Earth. We infer from gravitational effects the presence of this dark matter, a type of matter that

[3]Basically, the Big Bang theory suggests that all the matter in the universe, both present and past, originated simultaneously around 13.8 billion years ago. During this period, all matter was condensed into an extremely tiny, infinitely dense, and intensely hot sphere known as a Singularity.

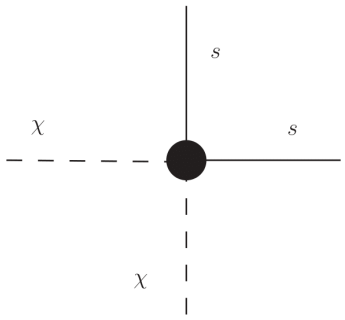

Figure 1.4: Illustration of the scattering processes via a vertex between two SM particles s and two DM particles χ.

we cannot see. There is strong evidence that it might not be made up of protons, neutrons, and electrons. The Dark Matter (DM) problem is the discrepancy between the observed mass in the universe and the amount of mass predicted by the laws of physics. DM is a hypothetical form of matter that is thought to account for approximately 85 % of the matter in the universe [93]. The existence of DM was first proposed in the 1930s by Swiss American astronomer Fritz Zwicky, who noticed that the observed mass of galaxy clusters was not enough to account for the gravitational forces within them [93]. Today, physists indirectly study DM by using gravitational lensing [94]. The rest of the universe appears to be made of dark energy (68 %) and "ordinary" visible matter (5 %) [93, 94]. Recent Cosmic Microwave Background (CMB) observations by the Planck team [95, 97, 120] yield a dark matter density Ω_c that is normalized to the universe's total energy density of

$$\Omega_c h^2 = 0.120 \pm 0.001, \tag{1.47}$$

where h is the reduced Hubble parameter. There are various theories about what dark matter might be made of, such as Weakly Interacting Massive Particles (WIMPs), Axions, and sterile neutrinos, but so far, none of these proposals have been confirmed through experimental observation. DM is permitted to interact with SM particles with couplings very comparable to the weak interaction under the existing constraints. This makes the inclusion of DM candidates an interesting extension of the SM. There are additional candidates for non-particle DM, such primordial black holes. The hunt for DM particles is still being done experimentally. The majority of WIMP searches rely on processes of scattering across a vertex between two DM particles χ and two SM particles s, with the content of the resulting blob depending on the specified dark matter model. The annihilation of two χ into two s

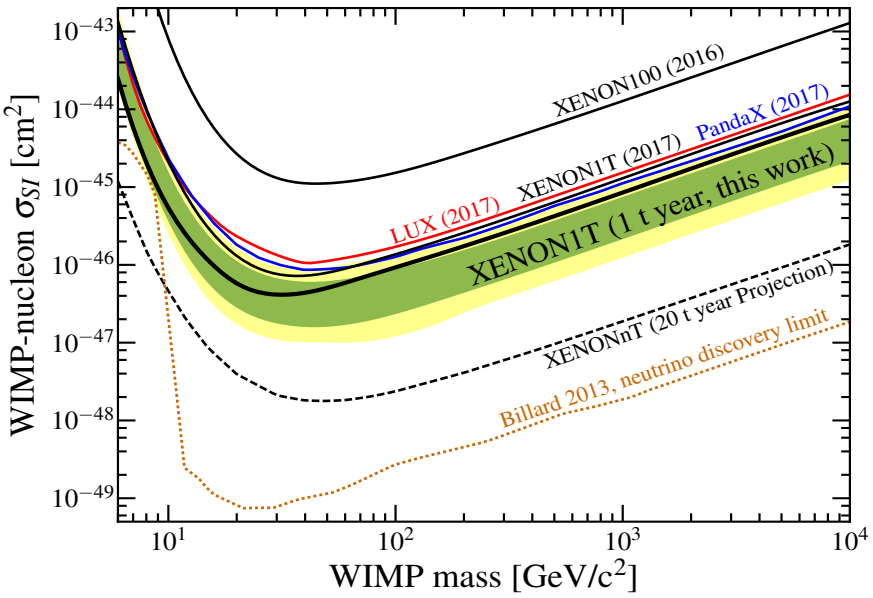

Figure 1.5: Result taken by the XENON1T experiment from [121]. Bound on the spin-independent dark matter nucleon scattering cross section at 90 % confidence level as a function of the DM mass. The blue and red curves indicate previous bounds by different experiments (LUX [99] and PandaX-II [100]) and the inset shows a normalisation of the plot the expected XENON1T limit.

(as in Fig. (1.4)) can be looked for in cosmic rays and is named indirect detection. Through searches for initial state radiation and missing energy, pair production of dark matter particles may be studied at colliders (called mono-X searches, where $X \in \{j, h, \gamma, ...\}$ depending on the radiated particle). Another possibility is called direct detection (scattering a dark matter particle off a SM particle). Direct detection experiments typically look for scattering of DM against heavy nucleons, where Xenon is currently the most prominent scattering medium for WIMPs. The strictest bounds on WIMPs are presently provided by direct detection experiments. Fig.(1.5) displays the XENON1T experiment's strongest direct detection bound as of now on the spin-independent scattering cross section.

1.3.5 Neutrino masses

Neutrinos have no mass according to the SM because there are no right-handed neutrino fields, however recent observations of neutrino oscillations [96, 98] have shown that they have a tiny mass. The discovery of neutrino masses raised several questions and challenges for particle physics, including the origin of the masses and their relationship to the masses of other particles in the SM. Proposed explanations for the origin of neutrino masses include the

so-called "seesaw mechanism", which involves the existence of heavy, undiscovered particles that interact with neutrinos, and the idea that neutrinos could be Majorana particles[4]. The evidence for neutrino mass requires new physics beyond the SM. This problem may be resolved by adding right-handed neutrinos $\nu^\alpha \equiv \nu_R^\alpha$, so that neutrinos may get mass through the same mechanism that generates masses for the quarks and charged leptons. The SM is therefore extended by adding a gauge-invariant term to the Lagrangian involving only two right-handed neutrinos, known as a Majorana mass term and contains N sterile neutrinos

$$\mathcal{L}_{\nu_R} = \overline{\nu}^\alpha i\not{D}\nu^\alpha - \left(\lambda_{i\beta}^\nu \overline{L}^i \nu^\beta \tilde{\phi} + h.c.\right) - \frac{1}{2} M_{\alpha\beta} \overline{\nu}^\alpha \nu^\beta, \tag{1.48}$$

where $\lambda_{i\beta}^\nu$ are the neutrino Yukawa couplings, $M_{\alpha\beta}$ is the Majorana mass matrix, and $\alpha = \beta = 1, ..., N$, where $N \geq 2$ so that at least two neutrino states are massive. When electroweak symmetry is broken, the Higgs field gets a vacuum expectation value. The neutrino mass eigenstates are then determined by diagonalizing the complete $(3+N) \times (3+N)$ neutrino mass matrix

$$m_\nu = \begin{pmatrix} 0 & \lambda_{i\beta} < \phi > \\ \lambda_{\alpha j}^* < \phi > & M_{\alpha\beta} \end{pmatrix}. \tag{1.49}$$

"Active" neutrinos are defined as linear mass eigenstates that are mostly composed of left-handed neutrinos, and "sterile" neutrinos are defined as linear mass eigenstates that are predominately composed of right-handed neutrinos. Light sterile neutrinos are often candidates for dark matter. We denote this neutrino ν_s, with mass m_s and mixing angle θ defined by $\nu_s = cos\,\theta\,\nu_R + sin\,\theta\,\nu_L$, where $\nu_R\,(\nu_L)$ is a linear combination of right-handed (left-handed) gauge eigenstates. The precise values of neutrino masses are also not well known, and measuring them accurately is an active area of research in particle physics. The nature of dark matter, the origin of the universe, and other unanswered topics in particle physics may be revealed through precise measurements of neutrino masses.

1.3.6 Unification of forces

One of the major goals of particle physics is to unify the various fundamental forces in a “Grand Unified Theory (GUT)” or “Theory of Everything” which could offer a more elegant

[4]It is named after the Italian physicist Ettore Majorana, who proposed it in 1937 as a means of describing fermions that are their own antiparticle [102], i.e if the neutrino is identical to its antineutrino (whether or not they are is unknown).

understanding of the structure of the universe. Such a simplification of the SM might well help to answer our questions and point toward future areas of study. James Maxwell took a big step toward this goal when he unified electricity and magnetism, and physicists now understand that at high energies the electromagnetic and weak forces are aspects of the same force called the electroweak force. This unification was proposed in the 1970s. The strong nuclear force, which holds protons and neutrons together in the atom's nucleus, is responsible for this, although it is still incompletely understood and has not yet been unified with the electroweak force. Moreover, the SM does not account for gravity, which is the force that governs how objects behave on vast sizes and is explained by the theory of general relativity. General relativity is a classical theory, nevertheless, and cannot be reconciled with the ideas of quantum physics, which explain how subatomic particles behave. As a result, it is still a challenge for theoretical physics to develop a good theory of quantum gravity that integrates gravity with the other basic forces. If there is a Grand Unification of all interactions, then every interaction we see is only a different feature of the same, unified interaction. How, therefore, can this be the case if the strengths and effects of electromagnetic interactions (both strong and weak) are so different? Bizarrely enough, data and theory contend that, for sufficiently high energy, all of these various forces combine into a single force.

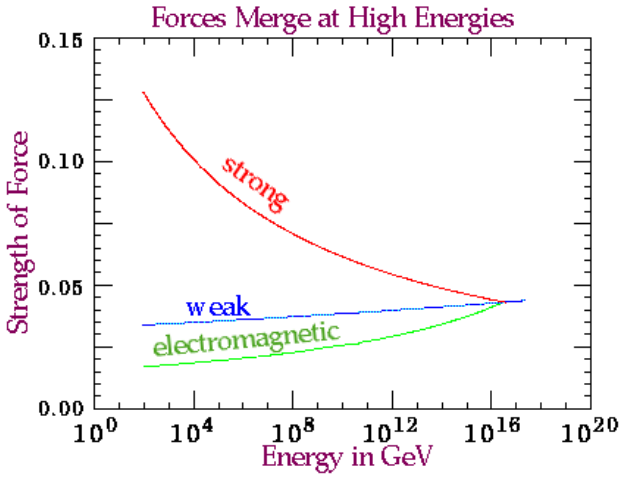

Figure 1.6: Grand Unification Theories propose that at the highest energy levels, which would have occurred shortly after the Big Bang, the effects of forces of nature is indifferentiable. Image sourced from The Particle Adventure.

Chapter 2

Physics of Lepton colliders

One of the planned future leptonic colliders is the international Linear Collider (ILC). Many reasons will make a deal for building ILC or any similar collider such as the Compact Linear Collider (CLIC) which would operate at higher energies than ILC (ILC up to $1\,TeV$ and CLIC up to $3\,TeV$). CLIC and the ILC have been unified under the Linear Collider Collaboration [103].

2.1 Historical view

Over many yeares, as well as the considerable cost of designing, building, and operation of the technology that serves as the experimental basis for the SM. This strategy runs the risk of grossly underestimating the cost and sociotechnical challenges faced when building the ILC and its detectors. The history of particle physics in the 20th century has been a steady progression toward higher and higher energies for particles with ever smaller particles. Studying smaller particles requires shorter de Broglie wavelengths $\lambda = h/p$, which requires probes of increasing energy. In the early 20th century, probes made from cathodic or radioactive nuclear decay were sufficient for tabletop discoveries, but as the century progressed, more complex and expensive technology were required. Tabletop experiments performed by a single experimentalist with a small number of helpers were adequate for making significant findings for the initial generation of SM fermions. With a cathode ray tube, a simple handheld evacuated glass tube with low voltages for electron emission, acceleration and deflection, J.J. Thomson made the discovery of the electron in 1898. The glass tube itself served as the detector. The experiment of Geiger and Marsden which led Ernest Rutherford

to the discovery of the atomic nucleus in 1911 was a simple setup of a Radium source of incident alpha particles, a lead collimator, Gold foil for providing heavy nuclei targets and a phosphorescent screen of Zinc Sulfide for a detector. Similarly, the discovery of the photon as the gauge boson which mediates the electromagnetic interaction occurred with considerable theoretical energy on the part of James Clerk Maxwell, Max Planck and Albert Einstein but, by today's standards, negligible cost and simple experimental technology. The photoelectric effect, blackbody spectrum, Compton scattering and Franck-Hertz experiments are easily demonstrated in beginning undergraduate physics courses.

By the time Niels Bohr and others used the results of low-cost spectroscopy experiments to figure out how electrons, nuclei and photons make up non-relativistic quantum atoms, the energies and event rates of tabletop experiments were no longer sufficient for new discoveries. The tabletop experiments of nuclear beta decay, from which Wolfgang Pauli inferred the existence of the neutrino in 1930, and of James Chadwick, used to discover the neutron in 1932, were some of the last. A step away from tabletop experiments, physicists are looking not here on earth for electrons crossing voltage differences or nuclear fragments escaping decaying nuclei, but for a new source of high-energy particles in the sky: secondary showers of particles created by collisions of highly energetic cosmic rays (protons or atomic nuclei) with atoms in the atmosphere. Like the tabletop experiments using radioactive nuclei, cosmic ray experiments cannot provide a uniform energy or intensity, but the energies could be orders of magnitude larger than in the tabletop experiments and the event rates were large enough for new discoveries by sufficiently patient physicists.

The year 1932 was also the year the positron e^+ was discovered among cosmic secondaries by Carl Anderson in a detector known as a cloud chamber, invented by Charles Wilson in 1911. The positron is the antimatter version of the electron e^-, first predicted by P.A.M. Dirac in 1931 using his fully relativistic quantum mechanics. The cloud chamber is a closed device filled with supersaturated water or alcohol which, when traversed by a charged particle, exhibits a visible track due to condensation centers made by ions created from the traversing charged particle. Four years later, in 1936, Anderson discovered the charged muons π^+, π^- and the muons μ^+, μ^- in the same cloud chambe. The neutral and charged kaons K^0, K^+, K^- were discovered in cosmic secondaries in 1947 in cloud chambers. The table 2.1 summarizes the chronological evolution of particle accelerators.

In 1954, war-devastated nations banded together to build the CERN in Geneva, a sig-

Year	Accelerator	Beam energy
1921	"Kaskadengenerator" (Greinacher)	
1924-1928	Concept and first prototype of linear accelerator (Ising /Wideroe)	
1932	First nuclear reaction induced by cascade particle, protons accelerator $p\,^7Li \rightarrow 2\alpha$ (Cockroft / Walton)	$400\,keV$
1930	First Van de Graaff accelerator	$1.5\,MeV$
1930-1932	First cyclotron (concept: Lawrence) Upgraded cyclotrons (Synchrocyclotron)	$1.5\,MeV$ $300-700\,MeV$
1953	First synchrotron at Brookhaven lab—Cosmotron (concept: Oliphant / Veksler / McMillan)	$3\,GeV$
1958	Proton Syncrotron (CERN)	$28\,GeV$
1983	Tevatron (Fermilab)	$1000\,GeV$
1990	HERA (DESY): first and only electron-proton collider	$320\,GeV$
2008	Large Hadron Collider (CERN)	up to $7000\,GeV$

Table 2.1: Timeline of particle accelerator evolution

nificant new laboratory. The Joint Institute for Nuclear Research (JINR) was founded in Dubna, Soviet Union, shortly after that in 1956. The Deutsches Elektronen Synchrotron (DESY) facility was established in Hamburg, West Germany, in 1960. The Institute for High Energy Physics opened its doors in China in 1973. The KEK was established in Japan considerably later, in Tsukuba in 1997. In 1947, a group of universities in the US joined forces with the government to establish a national laboratory at Brookhaven on Long Island. Other national labs in the western US also had their roots at Stanford University and the University of California, Berkeley. They later evolved into the Lawrence Berkeley National Laboratory (LBNL), the Stanford Linear Accelerator Center (SLAC), and the Brookhaven National Laboratory (BNL) (LBNL). Just west of Chicago, the Fermi National Accelerator Laboratory (FNAL), usually referred to as Fermilab, was founded in 1967.

2.2 Colliders principle

Among experiments in particle physics, collider experiments which may be classified into three types: synchrotron colliders, linear accelerators (LINAC) and linear colliders. Where each collider experiments can be arranged to provide collisions of two types: **Fixed-target accelerators** and **colliders**, as shown in the Fig.(2.1). In both cases one can study the resulting interactions with particle detectors.

In a fixed-target accelerator, a charged particle such as an electron e^- or a proton p is

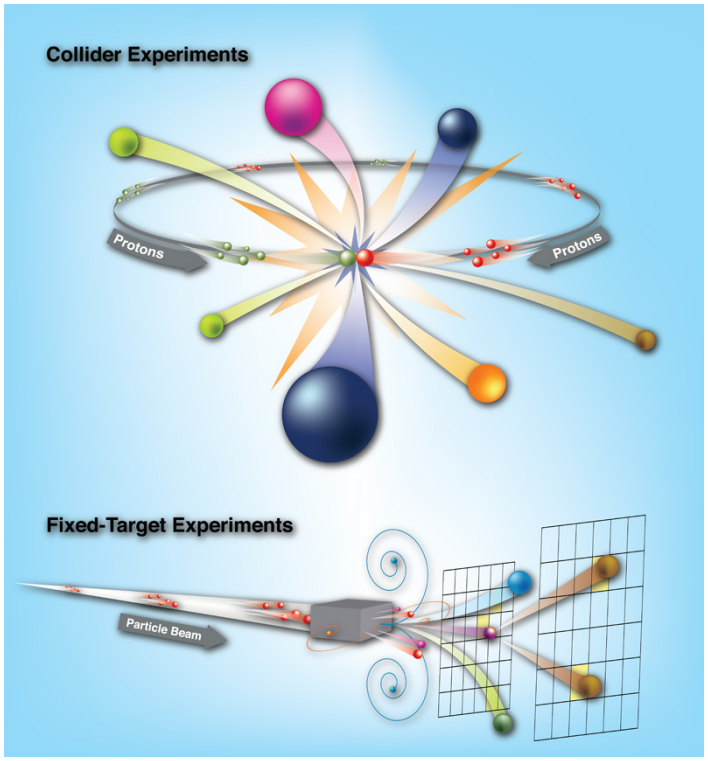

Figure 2.1: Colliders (up) and Fixed-Target accelerators (down).

accelerated by an electric field and collides with a target, which can be a solid (e.g. lead), liquid (H_2), or gas. A detector determines the charge, momentum, mass, etc... of the resulting particles. Advantages of fixed-target accelerators include: **(1)** Higher event rate due to the fact that targets are dense. **(2)** Produced particles in fixed-target accelerators are boosted, i.e. they have large forward momentum. Therefore they can produce collimated beams of secondary particles. This is useful for neutrino beams which are aimed at targets long distances away. In colliders experiment, two beams of high-energy particles are produced and are steered into each other so that their constituent particles can collide in the opposing direction. For such colliders both beams have equal energy if the initial particles have identical mass (e.g. LEP and LHC). This results in a lot more energy going into interesting (new) physics. For instance if we have two beams of energy $E = 80\,GeV$, then the centre-of-mass energy would equal $E_{CM} = 160\,GeV$, it would thus be possible to "discover" a particle of a mass up to $m = \frac{E}{c^2} = 160\,\frac{GeV}{c^2}$. The advantage of colliders is that both beams have significant kinetic energy, so a collision between them is more likely to produce a higher mass particle than would a fixed-target collision (with the one beam) at the same energy. Since we are

dealing with particles with a lot of momentum, these particles have short wavelengths[1] and make excellent probes. For a fixed target, the momentum 4-vectors (in natural units) are

$$p_1^\mu = (E, \overrightarrow{p}) \; ; \; p_2^\mu = (m, 0) \, . \tag{2.1}$$

So, if s is defined to be the square of the center of mass energy, s is equal to

$$s = (p_1^\mu + p_2^\mu)^2 = (E + m)^2 - p^2 = E^2 + 2mE + m^2 - p^2, \tag{2.2}$$

using the relativity relation $E^2 - p^2c^2 = m^2c^4$ (with m the mass of both the beam and target particles) and neglecting the mass of the target, the centre of mass energy is therefore

$$\sqrt{s} \cong \sqrt{2mE}, \tag{2.3}$$

since E represents the energy of the incoming beam, the center of mass energy grows only with square root of (E). However, for colliders the beams both have momentum and energy, for simplicity let us suppose that the projectile and target particle are the same, or possibly particle antiparticle (e.g. proton-proton, proton-antiproton, or electron-positron) so that their masses, m are the same, so

$$s = \left(\sum_i E_i \right)^2 - \left(\sum_i p_i c \right)^2 , \tag{2.4}$$

In the centre-of-mass frame, where the momenta are equal and opposite the second term vanishes and we have

$$s = 4E_{CM}^2 \, . \tag{2.5}$$

For symmetric colliders, such as LEP (e^+e^- collider) and LHC ($p\overline{p}$ collider), the laboratory frame is the centre-of-mass frame, outgoing particles are produced uniformly in space with total momentum equal to zero. For non-symmetric colliders (Fig. 2.2), such as HERA, the total momentum is not zero, and the lab frame is not the centre of mass frame.

[1]The spatial resolution increases with beam energy. According to the de Broglie equation, the relation between momentum $|\overrightarrow{p}|$ and wavelength λ of a wave packet is given by $\lambda = \frac{h}{|\overrightarrow{p}|}$.

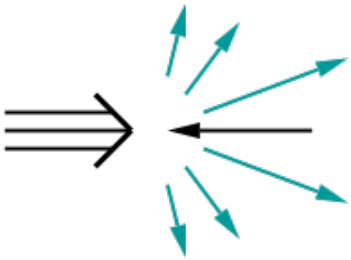

Figure 2.2: The non-symmetric colliders

2.2.1 Cross section

In physics the cross-section σ is a measure of the probability of interaction, and may be considered as the effective area available for the reaction by a given target. The cross-section is the number of reaction events per unit time per unit flux of incident beam (number of incident particles per unit time per unit area) per unit particles in the target, so it has units of area$\left(m^2\right)$, the common unit is barn, $1\,b = 10^{-28}m^2$. The total cross-section σ_{tot} is a sum of contributions by many final states $\sigma_{tot} = \sum_i \sigma_i$, We could write

$$\sigma_i = \frac{f_i}{J.N}, \tag{2.6}$$

Here f_i is the number of observed events per unit time, N is the number of particles in the target, and $J = n.v$ is the flux of the incident beam, n is the volume density of the incident particles, v is the speed of the incident particles.

2.2.2 Luminosity

The luminosity $\mathcal{L}$ is the number of particle collisions per unit area per second. The number of events of a particular type which occur per second is the cross section multiplied by the luminosity. Cross section is simply an expression for the underlying quantum mechanical probability that an interaction will occur. So, the general formula for reaction rate

$$R = \frac{dN}{dt} = \sigma.\mathcal{L}, \tag{2.7}$$

while for the integrated luminosity over the time $L = \int \mathcal{L} dt$, and has units of cm^{-2} (or fb^{-1}, pb^{-1}ect.), the number of events, N is given by

$$N = \sigma.L\,. \tag{2.8}$$

The cross sections characterize the scattering process, the luminosity characterizes an accelerators performance. The event rate can also be specific to a given channel or can be a total event rate for any outcome. Because the dimension of the cross section is a surface, the units of luminosity are $m^{-2}.s^{-1}$. If n_1 particles in a bunch[2] are incident on n_2 targets in a colliding bunch, and bunches are brought into collision at frequency f, then the time rate of particle particle interactions is $f\, n_1 n_2$, then the luminosity is given by

$$L = \frac{f\, n_1 n_2}{A}, \tag{2.9}$$

where A is the cross-sectional area of the bunches. Note that, if there are several bunches in the beams then $f = b \times \nu$, where ν is the revolution frequency of the bunches and b is the number of bunches in each of the beams. Considering e. g. an e^+e^- accelerator with N particles per beam, revolving f times per second, for bunches with Gaussian populations of horizontal width σ_x and vertical width σ_y at the interaction point, the bunch cross section is elliptical with area $A = 4\pi\sigma_x\sigma_y$. In one turn, one electron crosses $N/(4\pi\sigma_x\sigma_y)$ positrons. Because there are N particles revolving in each beam f times per second the number of collisions per second is

$$L = \frac{fN^2}{4\pi\sigma_x\sigma_y}, \tag{2.10}$$

from eq. (2.7), the number of events per second is

$$R = \frac{\sigma f N^2}{4\pi\sigma_x\sigma_y}, \tag{2.11}$$

luminosity can be enhanced by reducing the cross-sectional area of the beam, by increasing the number of particles in the beam or by increasing the revolution frequency.

[2]bunch of particles: it is a beam divided into chunks (the beam is not a continuous string of particles). In accelerators particles are grouped and accelerated in bunches of multiple particles means maximizing the number of particles brought into collision per unit time, so maximizing the rate of interesting events at a collider.

2.2.3 Classification of colliders

As we mentioned above there are three collider experiments, as shown in Fig.(2.2.3)

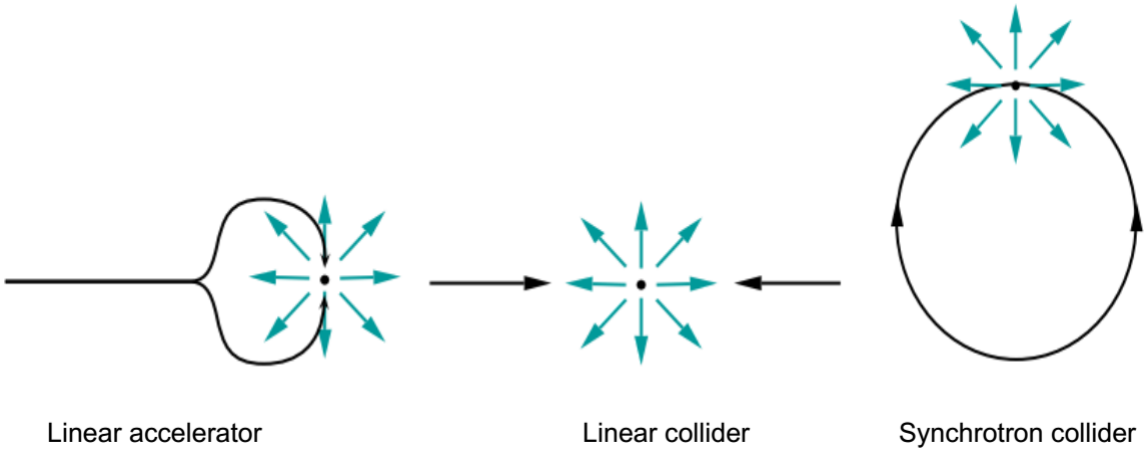

Figure 2.3: An illustration of different collider types.

2.2.3.1 Synchrotron colliders

A synchrotron is a particular type of cyclic particle accelerator, descended from the cyclotron, in the case of the synchrotron, the trajectory radius is kept constant. This is achieved by dipole magnets see Fig.(2.4). A charged particle with charge q moving with velocity v in a magnetic field B experiences a force F, where $F = qv \times B$, when the magnetic field is perpendicular to the plane of motion of the charged particle, this force is always towards the

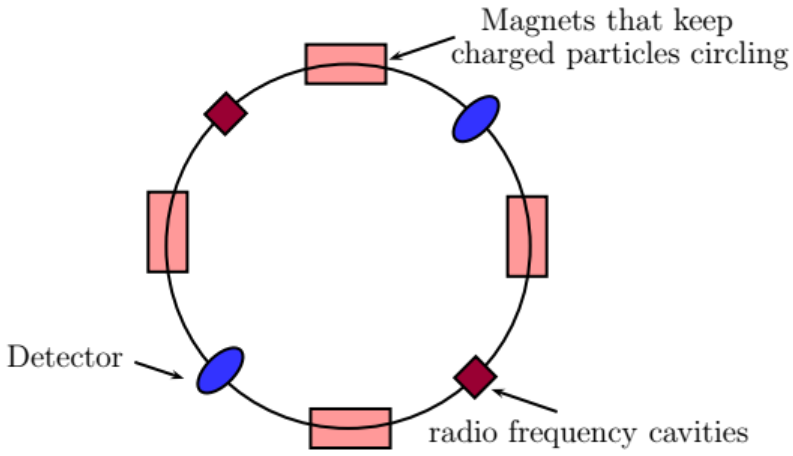

Figure 2.4: The general design of synchrotron colliders. The bremsstrahlung of photons produces significant energy loss.

centre and gives rise to centripetal acceleration, so that at the moment when the particles are moving in a circle of radius r

$$F = qvB = m\frac{v^2}{r}, \tag{2.12}$$

where m is the mass of the particle. the angular velocity $\omega = v/r$ is constant, so that the frequency of the alternating electric field remains constant. The maximum energy that the particles can acquire depends on the radius, R, for which the velocity has its maximum value $v_{max} = \frac{BqR}{m}$, thus the maximum kinetic energy is

$$T_{max} = \frac{1}{2}mv_{max}^2 = \frac{B^2q^2R^2}{2m}. \tag{2.13}$$

In high energy accelerators the particles are accelerated to energies which are extremely relativistic (the particles are travelling very nearly with the velocity of light). Taking relativistic effects into account the angular velocity has to be modified

$$\omega = \frac{Bq}{\gamma m}, \tag{2.14}$$

where $\gamma = 1/\sqrt{1-\beta^2}$ and $\beta = v/c$. The problem of reducing the cross section to increase the particle density is solved by using quadrupole magnets. One of the main limiting factors of synchrotron accelerators is the Synchrotron Radiation. A charged particle moving in a circular orbit is accelerating (even if the speed is constant) and therefore radiates. The energy radiated per turn per particle is

$$\Delta E = \frac{4\pi q^2\beta^2\gamma^4}{3R}, \tag{2.15}$$

where γ is the Lorentz factor, $\gamma \simeq \frac{E}{mc^2}$ with E the energy of the particle and m its mass, and R is the radius of curvature of the circular path. Therefore for a given energy and radius of curvature, it turns out that the synchrotron radiation that is lost is proportional to m^{-4}. For relativistic electrons and protons of the same momentum the ratio of energy losses are very large for electrons versus protons

$$\frac{\Delta E_e}{\Delta E_p} = \left(\frac{m_p}{m_e}\right)^4 \simeq 10^{13}. \tag{2.16}$$

The main advantage of synchrotron colliders is the multi-chances of collisions since the particles go around the collider millions of times, leading to higher event rate of collisions. The main disadvantage, however, is that the charged particles are in orbit around circular paths due to the bending by the magnets. This means that the particles undergo centrifugal accelerations, which by the laws of electrodynamics leads to soft photon bremsstrahlung (synchrotron radiation), Examples of synchroton colliders: **Large Hadron collider (LHC)** pp **collider at CERN:** European Laboratory for Particle Physics, it can accelerate beams of protons to an energy of $6.5\,TeV$, where the Higgs boson was discovered. The discovery was announced on July 4, 2012. **Tevatron** $p\bar{p}$ **collider at FermiLab - Chicago:** was active until 2011 and was runinng in a $6.28\,km$ ring to energies of up to $1\,TeV$. The main achievement of the Tevatron was the discovery in 1995 of the top quark. **LEP** e^+e^- **collider at CERN - Geneva:** was used from 1989 until 2000 and then dismantled in order to make room in the tunnel for the construction of the LHC. **HERA** $e^{\pm}p$ **collider at DESY - Hamburg:** was a non-symmetric collider located at DESY. Operating from 1992 to 2007, HERA was a unique particle accelerator designed to collide electrons and protons at high energies.

2.2.3.2 Linear accelerators (LINAC)

These are used for fixed-target experiments, as injectors to circular accelerators, or as linear colliders see Fig.(2.2.3). Examples include the SLAC collider at Stanford university (USA).

2.2.3.3 Linear colliders

Here two beams collide head on with no circular paths, thus with no synchrotron radiation (unless there is a small bending in the path, which should not be significant). linear accelerators are much easier to build than circular accelerators because they don't need the large magnets required to coerce particles into going in a circle. The main disadvantage of linear colliders is that there is only one chance for collision. In fact, there are currently no linear colliders, however a plan to construct the "international linear collider" (ILC). There will be further discussion on ILC in section 2.4.

2.2.3.4 Linear vs. Circular Colliders

Specificated dipole magnets can bring counterrotating beams into collision at an interation point in a circular collider. To investigate the outcomes of the collisions, detectors are positioned all around the collision point (or points). Because bunches of identical charged particles will refract electromagnetically over time, focusing quadrupole magnets are required to focus the bunches back into focus in beams composed of them. In a circular collider, focusing quadrupoles often alternate with bending dipoles. For a circular collider, synchrotron radiation is a significant disadvantage. Photons are emitted by charged particles in circular orbits. For each orbit, relativistic particles with mass m, charge q, and energy E

$$\Delta E = \frac{4\pi}{3\epsilon_0}\frac{q^2}{R}\left(\frac{E}{m}\right)^4. \tag{2.17}$$

Light particles are particularly susceptible to synchrotron radiation since $\Delta E \propto m^{-4}$. Electron losses are far more severe than proton losses when comparing the two most frequently accelerated particles in a circular collision, as shown in eq. (2.16). With e^+e^- colliders, the power required can be expensive since energy lost to synchrotron radiation needs to be fed back into the beams to maintain fixed $\sqrt{s}$. The technical difficulty of circular e^+e^- colliders will increase when losses $\Delta E \propto E^4$. Higher center of mass energies are needed to explore novel physics. There is no synchrotron radiation for linear colliders. A basic linear accelerator, or LINAC, uses oscillating electric fields parallel to the beamline to create acceleration in the spaces between the drift tubes as the beam particles are guided by progressively longer drift tubes. When an e^+ linac beam collides with an e^- linac beam, a linear e^+e^- collider is formed. The collision location is then surrounded by a detector. The parameters of proposed linear and circular e^+e^- colliders are listed in table (2.2).

2.2.4 Particle detectors

The general aim of particle accelerators is to collide two particles at high energy and create new particles from combined energy and quantum numbers or to probe inside one of the particles to see what it is made of. We need particle detectors to gather data from experiments carried out at accelerators. Accelerators are disposed around the interaction region and detect (directly or indirectly) the reaction products. The most measurements performed on final

e^+e^-	Linear			Circular		
Collider	SLC	ILC	CLIC	LEP	CEPC	FCCee
$\sqrt{s}$, $[GeV]$	100	250	1500	209	240	350
D **or** C, $[Km]$	2×1.5	2×15	2×25	27	54	100
L, $[cm^{-2}s^{-1}]$	2.5×10^{30}	1.5×10^{34}	6×10^{34}	1×10^{32}	2×10^{34}	2.2×10^{36}
Years	1989-1998	-	-	1989-2000	-	-
Laboratory	SLAC	?	CERN?	CERN	?	CERN?

Table 2.2: LEP and The Stanford Linear Collider (SLC) are the immediate predecessors of the possible future e^+e^- colliders, with respect to their parameters. adapted from the PDG [120].

state particles are: spatial coordinates and timing of final state; momentum[3]; energy[4]; type of particle (particle ID). Only stable charged particles can be accelerated: such as electrons, positrons, protons, anti-proton and some ions. Potentially, the long-lived particles such as muon ($\tau \simeq 2 \times 10^{-6}s$) were discussed to be used in the future muon collider. and momenta, and/or distinguishing different particle types. When all these components work together to detect an event[5], individual particles can be singled out from the multitudes for analysis. Modern detectors consist of many different pieces of equipment which test for different aspects of an event (see Fig. 2.5). The reason that detectors are divided into many components is

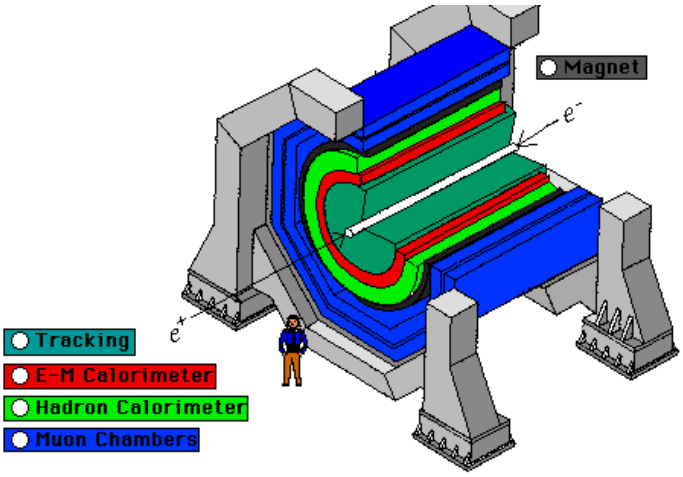

Figure 2.5: A schematic design of a typical modern detector.

[3]since all particles behave like waves, physicists use accelerators to increase a particle's momentum, thus decreasing its wavelength enough that physicists can use it to poke inside atoms.

[4]the energy of speedy particles is used to create the massive particles that physicists want to study.

[5]The event: After an accelerator has pumped enough energy into its particles, they collide either with a target or each other. Each of these collisions is called an event. The physicist's goal is to isolate each event, collect data from it, and check whether the particle processes of that event agree with the theory they are testing.

that each component tests a specific set of particle properties. These components are stacked in such a way that all particles pass through the different layers sequentially. A particle will not be evident until it either interacts with the detector in a measurable fashion, or decays into detectable particles. Important notes that can be cited from Fig.(2.6);

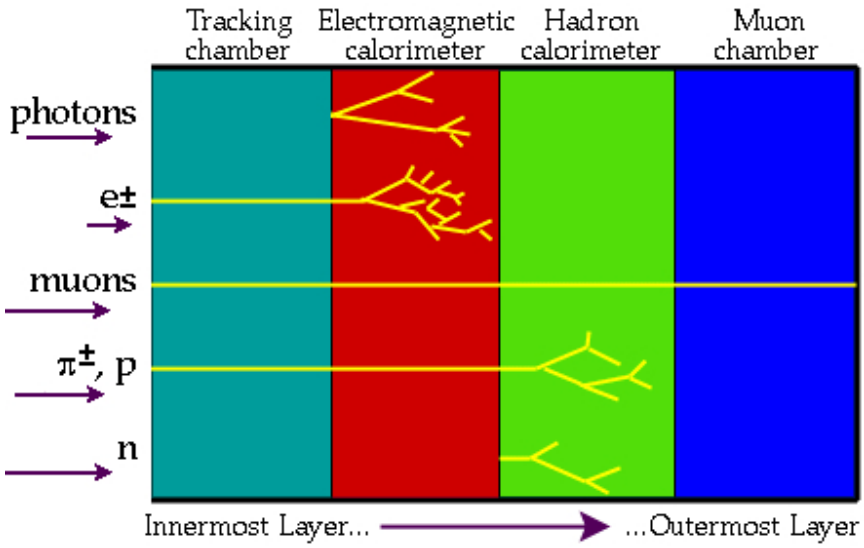

Figure 2.6: The interaction of various particles with the different components of a detector.

- Charged particles, like electrons and protons, are detected both in the tracking chamber and the electromagnetic calorimeter.
- Neutral particles, like neutrons and photons, are not detectable in the tracking chamber; they are only evident when they interact with the detector. Photons are detected by the electromagnetic calorimeter, while neutrons are evidenced by the energy they deposit in the hadron calorimeter.
- Each particle type has its own "signature" in the detector.
- Neutrinos are not shown on this chart because they rarely interact with matter, and can only be detected by missing matter and energy.

In the following part of this thesis, we will focus on e^+e^- colliders.

2.2.5 Particle Production and Decay

Particle production refers to the formation of new particles as a result of high-energy collisions or interactions between particles. This mechanism is commonly observed in particle

accelerators or during natural cosmic-ray interactions. When high-energy particles collide, they can transmit enough energy to produce new particles. These newly created particles can be stable and quantifiable or they can be unstable and decay into other particles extremely quickly. Particle creation can occur via a variety of mechanisms, depending on the energy and type of particle involved. Common procedures include: Pair Production, Hadronization and Lepton Production. **Decay** of an elementary particle is a purely statistical process and occurs regardless of the particle's history. Consider the decay rate Γ of an unstable particle. For N particles the small change in dN in a small amount of time dt is

$$dN = -N\Gamma dt, \tag{2.18}$$

implying that $N(t) = N_0 exp(-\Gamma t)$ and the typical lifetime of a single particle is $\tau = 1/\Gamma$. In general, unstable particles can decay to a number of different final states. Hence the total decay rate is $\Gamma = \sum_f \Gamma_f$ where the sum is across all final states. The branching ratio (BR) for an unstable particle to a specific final state f is

$$BR\,(i \to f) = \frac{\Gamma_f}{\Gamma}. \tag{2.19}$$

The muon μ and tau τ are the only leptons that decay, both through virtual W emission, the former via $\mu \to W^*\nu_\mu \to e\nu_e\nu_\mu$ with branching ratio effectively unity[6], while for the $\tau \to W^*\nu_\tau$ with $W^* \to e\nu_e$, $\mu\nu_\mu$, $q_u q_d$ are accessible for first and second generation quarks. The top quark decays via $t \to bW$ before hadronization with branching ratio unity. All hadrons except the proton decay, also via virtual W emission from a quark within the hadron. The partial widths and branching ratios of the bosons W, Z, and H are considered here. The SM $Zf\bar{f}$ and $Wf_u f_d$ interactions required by gauge invariance, as well as the $Hf\bar{f}$ and HVV interactions determined by the Higgs mechanism, are depicted in Fig.(2.7). The W decays to either leptons $l\nu_l$ or quark pairs $q_i\bar{q}_j$. The decay of the Z is either to lepton pairs $l^+l^-, \nu_l\bar{\nu}_l$ or to quark pairs $q\bar{q}$. Using the Feynman principles with the vertex factors from Fig.(2.7)

[6]The Heisenberg uncertainty principle establishes a natural link between a particle's decay rate and the uncertainty in its mass, $\Delta E \Delta t \geq \bar{h}/2$. A shortlived particle with mass m and mass uncertainty $\Delta E/c^2$ may exist for a short lifetime $\Delta t = 1/\Gamma$, therefore at the most $\Delta E = \bar{h}\Gamma/2$. The mass will be in the interval $\left[m - \Delta E/c^2,\, m + \Delta E/c^2\right]$, therefore the natural width of the particle is $2\Delta E/c^2 = \bar{h}\Gamma$, or simply in natural units the width is just Γ with units of energy.

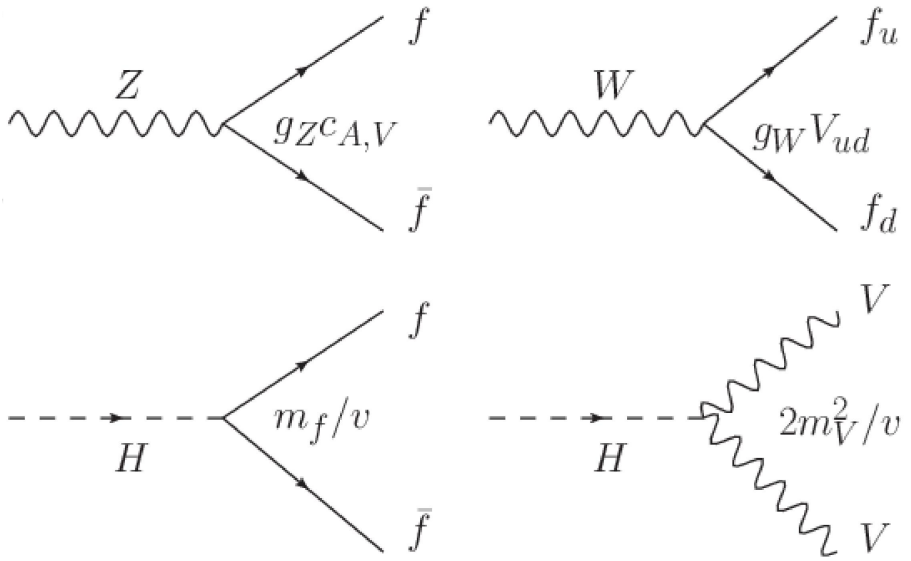

Figure 2.7: Some fundamental interaction vertices of the SM and their couplings to fermions (represented by solid lines), gauge bosons (depicted as wavy or looped lines), and the Higgs boson (shown with dashed lines). In the context of the Z boson vertex, C_A^f and C_V^f. represent axial and vector coefficients, respectively, while for the W. vertex, V_{ud} signifies the Cabibbo-Kobayashi-Maskawa (CKM) matrix element.

provides

$$\Gamma_{\mathrm{W}\to \mathrm{l}\bar{\nu},\, q_i\bar{q}_j} = \frac{\sqrt{2}G_F m_W^3}{12\pi} \times \left(1, 3\,|V_{ij}|^2\right) \tag{2.20}$$

$$\Gamma_{\mathrm{Z}\to\, l^+l^-,\nu\bar{\nu},\,\mathrm{q}\bar{\mathrm{q}}} = \frac{\sqrt{2}G_F m_Z^3}{3\pi} \times (X_l, X_\nu, 3X_q)\,, \tag{2.21}$$

with $G_F = \sqrt{2}g_W^2/8m_W^2$ is the Fermi's constant, which absorbs the vertex factors, and V_{ij} is the CKM matrix elements, and the short-hand $X_f = \left(C_V^f\right)^2 + \left(C_A^f\right)^2$ where C_A^f and $C_V^f$are axial and vector factors. The extra factors 3 appear for quarks because they carry an extra three degrees of freedom: strong colour r, g or b. Leptons $l_i\bar{\nu}_i$ are colourless. The measured decay rates and branching ratios for the W and Z are shown in table (2.3). Let consider the decay rates of the Higgs boson to fermion pairs $f\bar{f}$ and gauge boson pairs ZZ and WW. The Feynman diagram has a single vertex for fermion pairs, and the amplitude is just the vertex factor since there are no internal momenta: $\mathcal{M} = im_f/v$. The first order results are

$$\Gamma_{H\to f\bar{f}} = N_c \frac{G_F m_H m_f^2}{4\sqrt{2}\pi}\left(1 - \frac{4m_f^2}{m_H^2}\right)^{3/2}, \tag{2.22}$$

Decay	Γ_f (GeV)	$BR\,(\%)$
$W \to l\nu_l$	0.226	10.86 ± 0.09
$W \to hadrons$	1.41	67.41 ± 0.27
$Z \to l^+l^-$	0.088398	3.3658 ± 0.0023
$Z \to invisible$	0.4990	20.000 ± 0.055
$Z \to hadrons$	1.744	69.911 ± 0.056

Table 2.3: W and Z boson partial widths and branching ratios were measured. Uncertainties for partial width are suppressed. The total widths and branching ratios are tooken from the PDG [120].

with $N_c = 1$ for leptons and $N_c = 3$ for quarks. The amplitudes of ZZ and WW diagrams are $\mathcal{M} = -2im_Z^2/v$ and $\mathcal{M} = -2im_W^2/v$. At first order the results for $V = Z$, W are

$$\Gamma_{\mathrm{H}\to\mathrm{VV}} = S\frac{G_F m_H^3}{8\sqrt{2}\pi}\left(1 - 4\lambda_V^{1/2}\right)\left(12\lambda_V^2 - 4\lambda_V + 1\right), \tag{2.23}$$

where S is the statistical factor, $S = 1$ for $V = W$ and $S = 1/2$ for $V = Z$. $\lambda_V = \frac{m_f^2}{m_H^2}$. Decay rates for gauge bosons ZZ and WW are more difficult since one gauge boson is virtual due $m_H < 2m_W$, the previous decay rates assume they are both on mass shell, therefore they must be modified by phase space factors before being compared to experiment. The computed Higgs boson decay rates for $m_H = 125\,GeV$ at the current highest order, as well as the currently signal strengths are shown in table (2.4).

Decay	$\Gamma_f\,(MeV)$	$BR\,(\%)$	μ/μ_{SM}
$H \to b\bar{b}$	2.35	$57.7\,^{+3.21}_{-3.27}$	1.02 ± 0.15
$H \to WW^*$	0.875	$21.5\,^{+4.26}_{-4.20}$	$1.08\,^{+0.18}_{-0.16}$
$H \to gg$	0.349	$8.57\,^{+10.22}_{-9.98}$	-
$H \to \tau^+\tau^-$	0.257	$57.7\,^{+3.21}_{-3.27}$	1.11 ± 0.17
$H \to c\bar{c}$	0.118	$2.91\,^{+12.17}_{-12.21}$	-
$H \to ZZ$	0.107	$2.64\,^{+4.28}_{-4.21}$	$1.19\,^{+0.12}_{-0.11}$
$H \to \gamma\gamma$	0.00928	$0.228\,^{+4.98}_{-4.89}$	$1.10\,^{+0.10}_{-0.09}$
$H \to \mu^+\mu^-$	0.000891	$0.0219\,^{+6.01}_{-6.86}$	0.6 ± 0.8
Combined	4.07	100.00	1.10 ± 0.11

Table 2.4: Theoretical Higgs boson partial widths and branching ratios for $m_H = 125GeV$ at highest current order from the LHC Higgs Cross Section Working Group [101, 122, 123] with uncertainties are suppressed, and the measured signal strength relative to the SM μ/μ_{SM} from the PDG [120].

2.3 The LEP collider

LEP is the (Large Electron Positron) collider at CERN in Geneva (1982 -2000). It has circumference of $27\,km$ (same tunnel as the LHC) and collides e^+ and e^-. The maximum beam energy was $209\,GeV$. At the end of 2000, LEP was shut down and then dismantled in order to make room in the tunnel for the construction of the LHC. the LEP collider accelerated the electrons and positrons to a total energy of $45\,GeV$ each to enable production of the Z boson, which has a mass of $91\,GeV$. The LEP collider was run on two steps: **(1) LEP 1: 1989-1995** with a maximum beam energy was 50 GeV, and with centre of mass energy less than $100\,GeV$. From the measured cross-section for $e^+e^- \rightarrow hadrons$, the confirmation of the existence of the Z boson with a mass of about 91.2 GeV was achieved. When the beam energy is about $45.6\,GeV$ for each of the electron and positron, the Z boson is produced as a real particle (on-mass-shell), and the resonance is achieved in the process $e^+e^- \rightarrow Z \rightarrow hadrons$, as shown in Fig.(2.8) **(2) LEP 2: 1995-2000** it was not possible

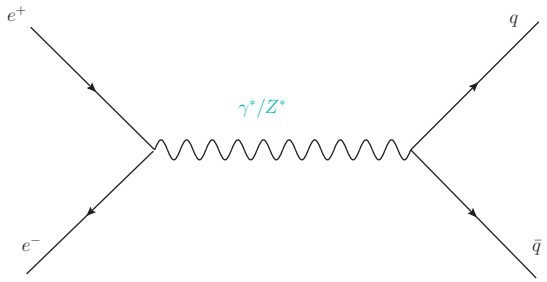

Figure 2.8: The possible diagrams contributing to $e^+e^- \rightarrow q\bar{q}$ procees contain both intermediate photons and Z.

to produce a W boson at LEP 1 because by conservation of charge, W bosons can only be produced in pairs, which required more centre of mass energy. The maximum beam energy reached was about $100\,GeV$ for each of the beams, with a centre of mass energy of about $200\,GeV$, this second run of the LEP collider was characterised by the production of a pair of W bosons each with mass $80.4\,GeV$.

2.4 The International Linear Collider (ILC)

The international leptonic collider (ILC) is a planned linear particle accelerator [104]. It is proposed to have a collision energy of $200 - 500\,GeV$ initially, with the possibility for a

later upgrade to $1\,TeV$. According to the ILC Technical Design Report (TDR) [105–107, 111], published in 2013, the accelerator project is technically feasible and construction ready. Furthermore, the Silicon Detector (SiD) and the International Large Detector (ILD), two detector types described in the TDR, are ready for construction. Schematic diagram of the ILC is shown in Fig.(2.9). The ILC and its detectors serve several purposes and have physics-related secondary motives that further the ILC's scientific usefulness. With a comprehensive ILC program, undiscovered new particles and interactions hypothesized by various theoretical models can be found, confined, or ruled out. In addition to the primary motivation for the ILC, the precise study of the Higgs boson, there is also the ILC goals outlined in the TDR, are summarized below:

- Measuring Higgs boson branching ratios at high precision.
- Constraining new interactions by measuring the W and Z bosons and the top quark at high precision.
- Searching for new particles, possibly including dark matter and supersymmetry.

We quote from the TDR Volume 1 [105] in more detail these goals: An initial ILC program for the 125 GeV Higgs boson will be centered at an energy of 250 GeV, giving a peak cross section for the reaction $e^+e^- \to Zh$. In this reaction, identifying the Z boson at the appropriate

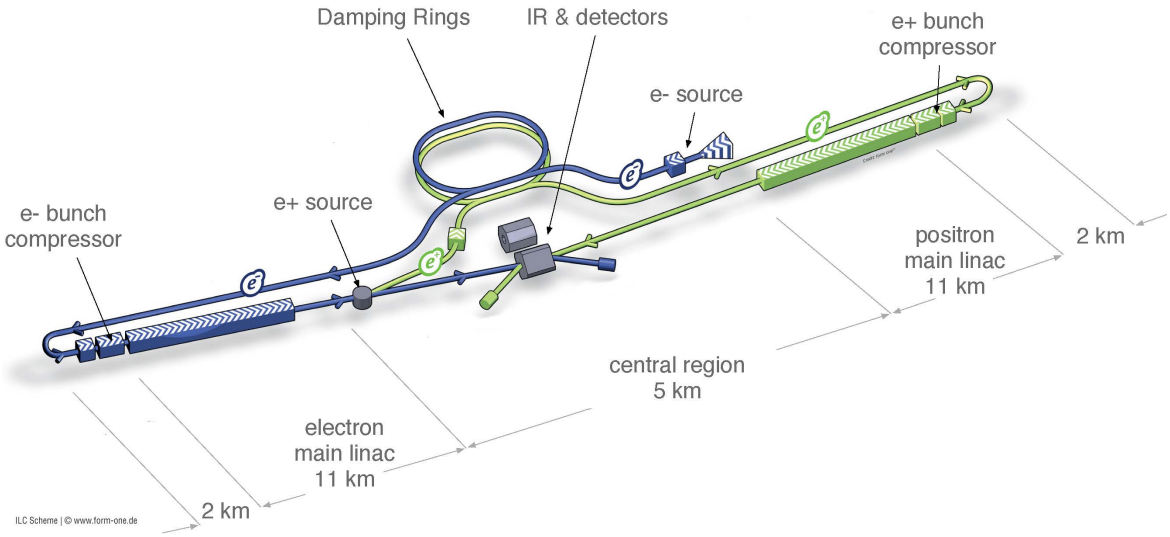

Figure 2.9: Schematic diagram of the main systems of the ILC assuming the nominal TDR design (as described in ref. [105]). Shown are the electron linac, the positron linac, the damping rings and two detectors at the collision point.

energy to recoil the Higgs boson indicates the presence of the Higgs boson. In this setting, the rate of all Higgs boson decays -even to invisible or unusual final states- can be measured with high precision. At $500\,GeV$, the full design energy of the ILC, measurement of the process $e^+e^- \to \nu\bar{\nu}h$ will give the absolute normalization of the underlying Higgs coupling strengths, needed to determine the individual couplings to the percent level of accuracy. A further increase in energy enables the ILC experiments to precisely measure the Higgs boson coupleing to the top quarks and to determine the strength of the Higgs boson nonlinear self-interaction. The ILC will also make important contributions to the search for new particles related to the Higgs field, dark matter and other problems in particle physics. For many such particles with only electroweak interactions, searches at the LHC will be limited by low rates relative to strong interaction induced processes, and by large backgrounds. The ILC will uniquely identify or reject these particles with a mass at least as high as the ILC's beam energy. The ILC will also constrain or discover new interactions at higher mass scales through the pair production of quarks and leptons, W and Z bosons, and top quarks. Much of our current detailed understanding of the Standard Model comes from precise measurements of the properties of the Z boson at e^+e^- accelerators. The ILC will extend this level of precision to the W boson and the top quark. The ILC will measure the mass of the top quark in a direct way that is not possible at hadron colliders. One can see that the TDR outlines several reasons why the ILC is the tool of choice to achieve these goals: **(1) cleanliness** At the LHC, a large number of background events contaminates each collision event, constraining detector design to increase radiation hardness and moving some detector elements away from the collision point. At the ILC, the number of background events for false collisions is much smaller, so detectors are not limited by radiation hardness limits and can be placed very close to the point of collision. **(2) Favorable signal-to-background ratio** ILC signal cross sections are not much smaller than background cross sections since all backgrounds are electroweak in origin. At the LHC background from strong interaction processes are very high compared to signal processes. **(3) calculability** ILC theoretical cross sections are calculated with considerably greater precision since the related uncertainty on QCD calculations is quite significant; in contrast to e^+e^- cross sections, which are computed with extremely high accuracy in order to make experimental departures from the SM more obvious. **(4) detail** Due to the clean event environment and the potential to polarize beams, the detailed spins of initial and final states can be reconstructed. Understanding the theoretical and experimental methods essential to

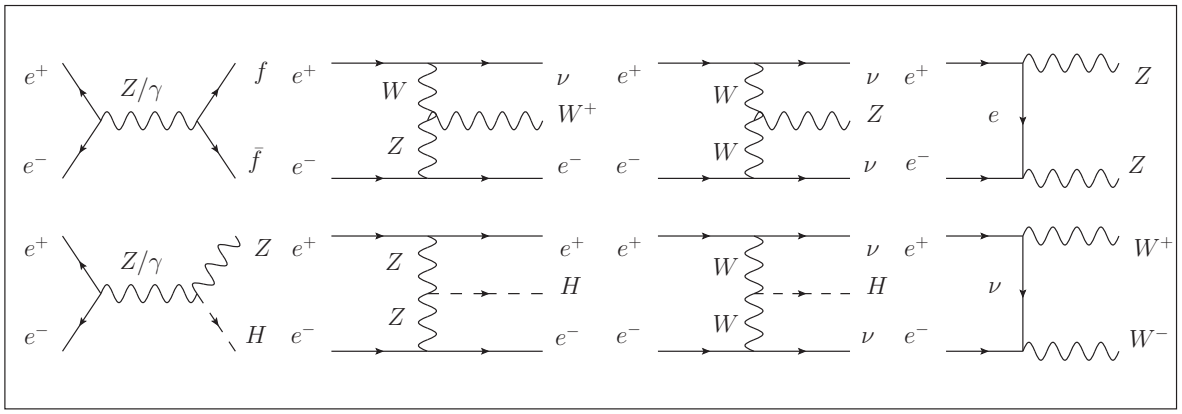

Figure 2.10: Feynman diagrams represent some of the main signals and backgrounds at the ILC. The s-channel diagrams for fermion pair production (top) and Higgstrahlung (bottom) are shown on the far left. The subsequent t-channel diagrams depict WZ fusion production of a single W (top), ZZ fusion production of a single H (bottom), WW fusion production of a single Z (top) and H (bottom), and diboson production of ZZ (top) and WW (bottom).

high energy physics as well as the software created to model the underlying physics at the ILC and its detectors will be required to achieve the physics goals of the ILC program.

2.4.1 ILC Signal and Background

All processes at the ILC can be classified based on the number of fermions f in their final state after boson decay. Thus $e^+e^- \to f\bar{f}$ is a $2\,f$ process, but $e^+e^- \to ZZ$ and WW are $4\,f$ processes. If either the e^- or e^+ beam splits, or if both beams split, the initial state may include one or two photons. Therefore, $\gamma e \to \gamma e$ is a $1\,f$ process, but $\gamma e \to eZ, \nu W$ are $3\,f$ processes. Initial states $\gamma\gamma$, $\gamma\gamma \to f\bar{f}, WW$ also lead to $2\,f$ and $4\,f$ processes. We consider final states originating from Higgs bosons as **Signal** processes, while all other final states are classified as **Background** processes. **Background:** Because the primary signal Higgs boson production process is $4\,f$ or $6\,f$, depending on decay, and $2\,f$ backgrounds are easily suppressed, the $4\,f$ and $6\,f$ backgrounds are the most important to consider. The Feynman diagrams of some of the major $4\,f$ and $6\,f$ backgrounds at the ILC are shown in Fig.(2.10). For their cross sections vs. $\sqrt{s}$ assuming unpolarized beams, see Fig.(2.11). **Signal:** At the ILC, the Higgs boson can be produced singly in three ways: Higgstrahlung $e^+e^- \to ZH$, WW fusion $e^+e^- \to \nu\bar{\nu}H$ and ZZ fusion $e^+e^- \to e^+e^-H$. Also Higgs bosons can be produced doubly in more rare processes: double Higgstrahlung $e^+e^- \to ZHH$ and double WW fusion $e^+e^- \to \nu\bar{\nu}HH$. In double Higgstrahlung the triple Higgs coupling HHH

is available, while in double WW fusion the $HHWW$ coupling is available. Double Higgs production is only possible at $\sqrt{s} = 500\,GeV$ with cross sections below $1\,fb$. Higgstrahlung is an s-channel process in which the H is radiated from a Z. Higgstrahlung occurs around the threshold at $\sqrt{s} \approx m_H + m_Z$, with the $e_R^+e_L^-$ cross section quickly reaching a maximum of $\sigma_{ZH} \approx 300\,fb$ near $\sqrt{s} \approx 250\,GeV$. Thereafter, it decreases with the characteristic $1/s$ dependence of an s-channel process, reaching approximately $\sigma_{ZH} \approx 200\,fb\,(100\,fb)$ near $\sqrt{s} \approx 350\,GeV\,(500\,GeV)$. Vector boson ($ZZ$ or WW) fusion production is a t-channel process in which a Z or a W is exchanged and the large ZZH and WWH couplings produce a Higgs boson. WW fusion turns on at threshold and the $e_R^+e_L^-$ cross section rises to $\sigma_{\nu\nu H} \approx 16\,fb$ ($64\,fb$, $160\,fb$) at $\sqrt{s} \approx 250\,GeV$ ($350\,GeV$, $500\,GeV$). ZZ fusion $e_R^+e_L^-$ cross section rises to $\sigma_{\nu\nu H} \approx 1\,fb$ ($3\,fb$, $8\,fb$) at $\sqrt{s} \approx 250\,GeV$ ($350\,GeV$, $500\,GeV$). The ILC will utilize polarized beams. Through the polarization of electrons and positrons, represented as $e_L^+e_R^-$ or $e_R^+e_L^-$, the activation or deactivation of a process becomes feasible: if the process needs the W to couple ν_R or $\bar{\nu}_L$ then it does not occur. However, achieving a complete polarization of 100 % for electrons or positrons is unattainable, resulting in a certain portion of the beams retaining an undesirable polarization component. Subsequently, we present cross sections values considering positrons with right-handed polarization (30 % polarization) and electrons with left-handed polarization (80 % polarization), which align with the ILC's targeted design. In both signal and background scenarios, cross sections are greater for $e_L^+e_R^-$ compared to $e_R^+e_L^-$, with the distinction being particularly pronounced in the background case. Refer to table (2.4.1) for the cross sections of $4\,f$ and $6\,f$ background processes involving polarized e^+e^- beams at collision energies of $\sqrt{s} = 250\,GeV$, $350\,GeV$ and $500\,GeV$. The cross-sectional values provided in table (2.4.1) encompass a significant factor: the influence of initial state radiation (ISR). Within a Feynman diagram involving the initial state e^+e^-, a photon can attach itself to either the electron or the positron. This photon carries off energy, leading to an effective reduction in the center-of-mass energy of the e^+e^- system. As a result, the particles engaged in interaction experience a cross section pertaining to a lower $\sqrt{s}$ compared to the nominal $\sqrt{s}$ corresponding to the beam energies. Hence, ISR effectively amplifies the cross section of a process that exhibits a diminishing cross section concerning the beam's $\sqrt{s}$. Conversely, it diminishes the cross section of a process that displays an escalating cross section with respect to $\sqrt{s}$. cross section vs beam $\sqrt{s}$, and decreases it for a process with an increasing cross section vs $\sqrt{s}$. In order to optimize a collider's luminosity, particles are grouped together

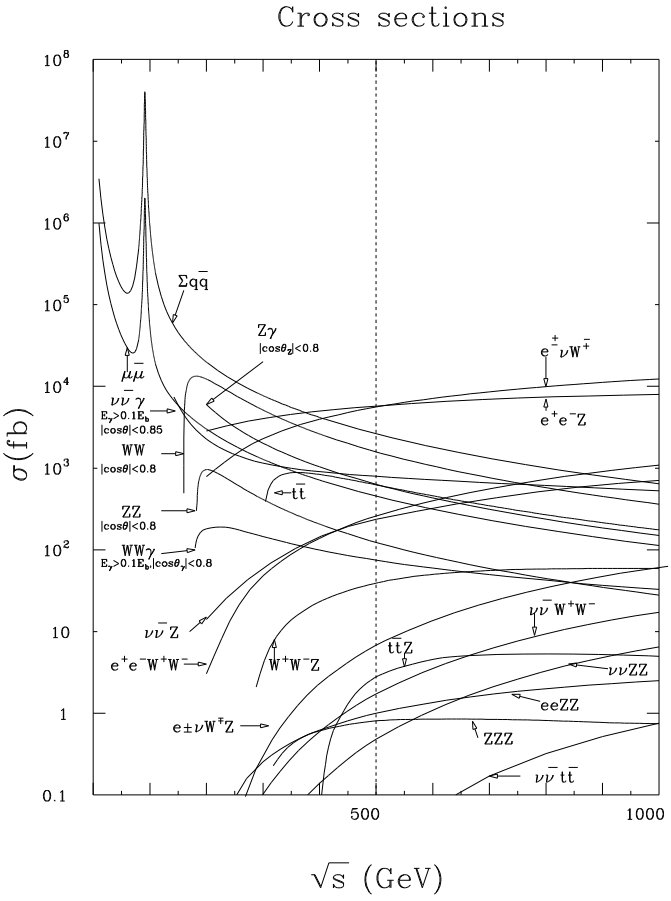

Figure 2.11: Total cross sections for e^+e^- to various SM final states vs $\sqrt{s}$ assuming unpolarized beams. The cross section for $\sum q\bar{q}$ below $\sqrt{s} \approx 100\,GeV$ is the same as Figure 6. From [112].

in bunches. This practice brings about a side effect known as beamstrahlung, where photons are emitted from either an electron or positron within the e^+e^- system due to the influence of an approaching bunch's electromagnetic field. This phenomenon bears resemblance to ISR: it causes a modest reduction in the effective $\sqrt{s}$ of the e^+e^- system. In table 2.4.1 cross section values for $\sqrt{s} = 250\,GeV$ are presented both with and without accounting for beamstrahlung. Beamstrahlung's impact is highly contingent on the specifics of the beam parameters, and the parameters assumed for the staged $ILC - 250$ [110] are applied in the instance outlined in table (2.4.1).

Process	$\sqrt{s} = 250$ GeV		$\sqrt{s^\star} = 250$ GeV		$\sqrt{s} = 350$ GeV		$\sqrt{s} = 500$ GeV	
P_{e^-,e^+}	$-0.8,+0.3$	$+0.8,-0.3$	$-0.8,+0.3$	$+0.8,-0.3$	$-0.8,+0.3$	$+0.8,-0.3$	$-0.8,+0.3$	$+0.8,-0.3$
$e^+e^- \to ZH$	0.313	0.211	0.297	0.200	0.198	0.134	0.096	0.064
$e^+e^- \to \nu\bar{\nu}H$	0.037	0.015	0.034	0.014	0.072	0.012	0.162	0.014
$e^+e^- \to e^+e^-H$	0.011	0.007	0.010	0.007	0.010	0.006	0.012	0.007
$e^+e^- \to b\bar{b}$	15.4	8.87	16.3	9.44	7.52	4.34	3.72	2.14
$e^+e^- \to c\bar{c}$	15.5	9.64	16.5	10.7	7.76	5.03	3.97	2.42
$e^+e^- \to u\bar{u}, d\bar{d}, s\bar{s}$	47.0	28.0	49.5	29.9	23.1	13.6	11.3	6.92
$e^+e^- \to \tau^+\tau^-$	6.10	4.74	6.36	5.02	3.02	2.43	1.57	1.21
$e^+e^- \to \mu^+\mu^-$	6.19	4.63	6.43	5.15	3.00	2.48	1.50	1.20
$e^+e^- \to WW$	37.5	2.58	37.9	2.62	27.1	1.79	17.9	1.15
$e^+e^- \to e^\pm\nu W^\mp$	10.2	0.109	10.4	0.108	10.1	0.134	10.9	0.215
$e^+e^- \to e^+e^-Z$	2.51	2.63	2.38	2.13	2.64	2.23	2.64	3.04
$e^+e^- \to ZZ$	1.80	0.827	1.82	0.837	1.20	0.552	0.761	0.348
$e^+e^- \to \nu\bar{\nu}Z$	0.354	0.117	0.347	0.117	0.470	0.092	0.780	0.088
$e^+e^- \to t\bar{t}$	0	0	0	0	0.267	0.117	0.890	0.421
$e^+e^- \to WWZ$	0	0	0	0	0.024	0.002	0.083	0.006
$e^+e^- \to ZZZ$	0	0	0	0	0.001	0.000	0.002	0.001

Table 2.5: At the ILC, cross sections (in pb) for the Higgs boson signal and some $4\,f$, $6\,f$ background processes for $\sqrt{s} = 250\,GeV$, $350\,GeV$, $500\,GeV$ were measured. ISR is incorporated. Beamstrahlung is included for $\sqrt{s}^\star$, but not for other $\sqrt{s}$. Beam polarisation for example: $-0.8, +0.3$ denotes 80 % negatively polarised electrons and 30 % positively polarised positrons. Whizard 2.6.4 was used to achieve this [113].

2.4.2 Detectors and the SiD & ILD

Detector in the context of particle physics refers to a complex and sophisticated instrument designed to identify and measure the properties of particles produced in high-energy collisions. Typically, the following assessments are carried out on particles in their final state:

- Determination of their spatial coordinates and timing.
- Measurement of their momentum and energy.
- Identification of the particle type (particle ID).

The quantitative signature of stable or quasistable particles crossing a collider detector is detected by energy transfers from the particle to the detector material mediated by electromagnetic or nuclear interactions. A particle's phenomenological signature in a collider detector can be classified as a resonance ($Z, W, t, \pi^0, \rho^\pm$) with lifetimes *too short* to observe directly, a displaced vertex (B, D, τ,... etc) with lifetimes $\tau \approx 10^{-12}\,s$, quasistable (muon, kaon, neutron,... etc) with $\tau \approx 10^{-8}s$, or stable (electron or proton) with $\tau = \infty$. Thus, the ranges of relativistic particles are essentially of order $c\tau \approx 0$, mm, m, respectively. For macroscopic detectors a few meters deep, only quasistable and stable particles are directly detected, but resonances and displaced vertices can be reconstructed from their quasistable or stable decay products by four vector addition. Neutrinos, because they only interact weakly, escape

undetected. Energy loss occurs for electrically charged particles due to induced ionisation of detector electrons, Coulomb scattering from detector nuclei, electromagnetic radiation (bremstrahlung) caused by detector nuclei, and nuclear scattering or absorption if the particle is a hadron. Energy loss happens for electrically neutral particles via photoelectric absorption, Compton scattering or pair formation (for photons), or nuclear scattering or absorption (for hadrons). The modern collider detector is a complex, integrated system of interdependent subdetectors controlled by high-speed electronics. It combines subdetectors like **trackers**, which measure the spatial position and, if a magnetic field is applied, momentum of traversing charged particles, with **calorimeters**, which measure the spatial position and energy of charged and neutral particles, and a variety of other specialized subdetectors. Regardless of whether the tracker technology employed is gaseous ionization or semiconductor-based, the spatial data points recorded by the tracker are processed mathematically to reconstruct the path taken by charged particles as they pass through. When a uniform magnetic field is applied within the active tracking region, it becomes possible to extract the parameters describing the helical path of a charged particle from the fitted track. These parameters are then used to determine the particle's momentum. The vertex detector is a specialized tracking component designed for highly accurate tracking, specifically to identify displaced vertices in close proximity to the interaction point. A tracker with excellent spatial resolution provides both precise spatial vertex identification and accurate momentum determination. Trackers are designed to minimize the energy loss experienced by particles passing through, whereas calorimeters are designed to maximize this energy loss. In the prevalent calorimeter setup, known as a sampling calorimeter, it comprises alternating layers of materials. Some of these layers are designed to induce particle showers and cause energy loss, while others serve as sensitive elements to measure the energy deposited. The way a calorimeter is divided into segments, and the size of these sensitive elements, significantly affects its ability to accurately resolve energy measurements. At the ILC, the International Large Detector (ILD) and the Silicon Detector (SiD) as shown in Fig.(2.12) will be operating in a push-pull mode. This enables one detector to collect data while the other undergoes maintenance. Consequently, both detectors must be self-shielding to facilitate access to one while the other is operational. Detailed descriptions of both detectors concepts are available in Ref. [111].

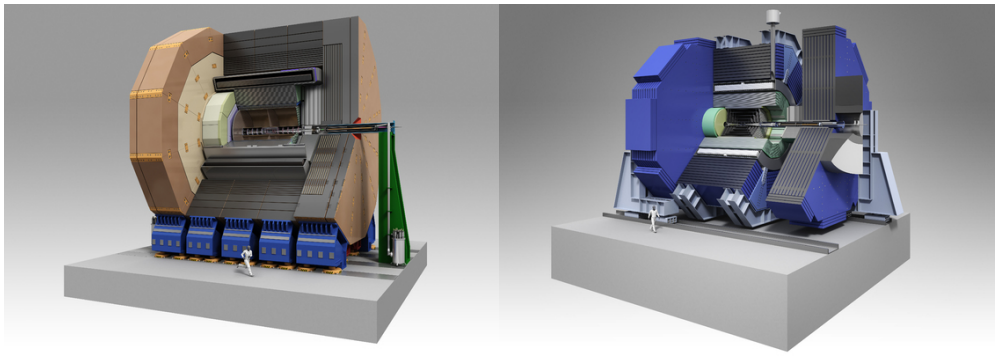

Figure 2.12: Illustration of the two ILC detector concepts: The ILD [114] (on the left) and the SiD [115] (on the right).

2.4.2.1 The ILD detector

ILD is conceived as a versatile detector with a specific emphasis on a precision physics program. This imposes rigorous criteria on ILD's performance: a vertex detector with a point resolution finer than $3\,\mu m$, outstanding tracking performance equivalent to an asymptotic transverse momentum resolution of $\sigma_1/p_T \approx 2 \times 10^{-5} GeV^{-1}$, and a jet-energy resolution of $\sigma_E/E \approx 3-4$, enabling the separation of hadronic decays from Z, W and Higgs bosons. An notable aspect of the ILD detector is its extensive Time Projection Chamber (TPC), creates approximately $\mathcal{O}(200)$ points per track. As depicted in Fig.(2.13), tracks are discernible by sight, facilitating efficient pattern recognition with minimal material budget. Moreover, the TPC enables particle identification based on dE/dx [116]. The particle flow concept achieves optimal event reconstruction by individually reconstructing all particles, both charged and neutral. Consequently, the calorimeter is optimized for particle flow, enabling the reconstruction of individual particles within jets.

2.4.2.2 The SiD detector

A general-purpose experiment to carry out accurate measurements at the ILC is the SiD detector concept. It fulfills the stringent requirements imposed by the diverse spectrum of ILC physics operations. SiD is grounded in the particle flow paradigm, employing an algorithm that optimizes the combination of tracking and calorimetry to reconstruct both charged and neutral particles. The result is an overall di-jet mass resolution that is sufficiently accurate to distinguish between Ws and Zs, along with a significantly more precise determination of jet energy compared to traditional methods. Utilizing a powerful silicon pixel vertex de-

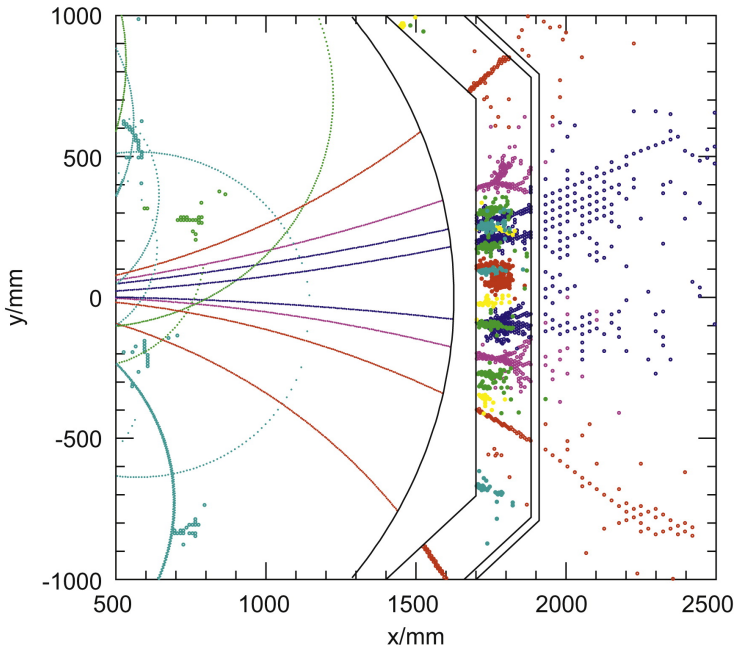

Figure 2.13: A simulated jet within the ILD detector, displaying particle flow objects reconstructed using the Pandora algorithm and depicted in various colours. From [117]

tector, silicon tracking, silicon-tungsten electromagnetic calorimetry, and highly segmented hadronic calorimetry, the SiD detector (Fig. (2.12)) is a compact detection system. SiD also incorporates a muon identification system, an iron flux return, and a high-field solenoid. The integration of silicon sensors in the vertex, tracking, and calorimetry allows for an exceptionally specialized tracking system perfectly suited for particle movement. SiD was designed to fulfill the physics objectives of the ILC [111].

2.4.3 Energy and luminosity

The energy and luminosity of the ILC has been designed to be progressively increased. Table (2.6) displays the parameters of the next steps that are most crucial to comprehending the physics studies. Starting at $250\,GeV$, the ILC will have a moderate design luminosity of $1.35 \times 10^{34} cm^{-2} sec^{-1}$. The ILC will have achieved a total integrated luminosity of $2\,ab^{-1}$ in about 11 years. An energy upgrade that involves extending the linear accelerators to double their energy will come next. In addition to $200\,fb^{-1}$ of luminosity around $350\,GeV$, the $500\,GeV$ stage will accumulate $4\,ab^{-1}$ of integrated luminosity at $500\,GeV$ to measure the top quark mass to the level of theoretical systematic errors. Throughout a 10 year program, the $1\,TeV$ operator is expected to accumulate $8\,ab^{-1}$ of integrated luminosity. The proposed

positron beam polarization and the expected high degree of electron beam polarization will aid in the collection of all this data.

	$91\,GeV$	$250\,GeV$	$350\,GeV$	$500\,GeV$	$1\,TeV$
$\int \mathcal{L}\,(ab^{-1})$	0.1	2	0.2	4	8
duration (yr)	1.5	11	0.75	9	10
beam polarization (e^-/e^+) %	80/30	80/30	80/30	80/30	80/20
$(--,-+,+-,++)$ (%)	(10,40,40,10)	(5,45,45,5)	(5,68,22,5)	(10,40,40,10)	(10,40,40,10)
$\delta_{ISR}(\%)$	10.8	11.7	12.0	12.4	13.0
$\delta_{BS}(\%)$	0.16	2.6	1.9	4.5	10.5

Table 2.6: ILC stage parameters which are most important to physics studies. The percentage of the total running time that is spent in each of the four possible beam polarization orientations is indicated in the fourth line. The average energy loss resulting from beamstrahlung and initial state radiation, respectively, can be seen in the fifth and sixth lines of the electron or positron energy spectrum. From [119].

2.4.4 Beam polarization

The polarization of the beam offers profound insights into the chiral makeup of the SM and may potentially unveil a gateway to physics that extends beyond the SM. Polarizing both beams creates four possible combinations $\left(e_L^- e_R^+,\, e_R^- e_L^+,\, e_L^- e_L^+,\, e_R^- e_R^+\right)$. In the SM, during $e^- e^+$ annihilation into a vector boson an electron annihilates a positron of the opposite helicity $\left(e_L^- e_R^+ \,\text{and}\, e_R^- e_L^+\right)$. The use of beams with opposite signs of polarization for electrons and positrons can enhance collision cross-sections for these processes. This approach is valuable in searches for NP involving scalar particles in the s-channel, where same-sign beam polarization helps suppress SM background (as we will see at next section..). For example, in searches for dark matter particle pair production with a photon employing same-sign beam polarization can reduce backgrounds significantly improving the detectability of the signature. Producing polarized electrons is relatively simple, while the production of polarized positrons is more challenging. Positrons, not naturally occurring in ordinary matter, are produced in sufficient quantities through pair production. This involves directing high-energy photons or electrons at a target. There are two main technical approaches: the current baseline, which is the undulator-based source utilizing photons, and an alternative method involving an additional electron beam to generate positrons [118]. The production of polarized electron beam involves using the photoelectric effect with polarized photons. This process entails illuminating a photocathode with a circularly polarized laser, where the helicity of the electron beam, defining

its polarization, can be altered by changing the laser polarization. The polarized electron source at SLC (Stanford Linear Collider) demonstrated that this approach meets the criteria for achieving a beam polarization of $\geq |80\,\%|$ and a bunch charge of 2×10^{10} electrons [105]. After creating polarized electron bunches, they undergo two-stage acceleration to $5\,GeV$ before entering the damping rings. Within these rings, particle spin precession occurs along magnetic field lines, reducing longitudinal polarization. To counter this, a superconducting solenoid reorients the spin vector vertically, creating transverse polarization and eliminating precession, aligning the spin with the magnetic field. Regarding ILC undulator specifications and positron bunch charge requirements, we can achieve a maximum positron beam polarization of $30\,\%$ (with the possibility to upgrade to $60\,\%$) [107]. Following the target, excess photons and electrons are discarded, and positrons are collected for delivery to the damping rings. The electron or positron polarization can be defined in terms of the number of left-handed (N_{fL}) and right-handed (N_{fL}) fermion components. For a given helicity state, the polarization ($P\,(f)$) is given by

$$P\,(f) = \frac{N_{fR} - N_{fL}}{N_{fR} + N_{fL}}. \tag{2.24}$$

The polarization ranges from -1 to 1, where $P = 1$ corresponds to complete left-handed polarization. $P = -1$ corresponds to complete right-handed polarization. $P = 0$ corresponds to an unpolarized state with an equal number of left-handed and right-handed components.

2.5 Kinematics and data analysis methods

Since all collider observables depend on the momentum and energy of the produced particles, reconstructing momentum is primarily accomplished through energy and angle information. This is largely sufficient because most relevant particles are essentially massless. The central calorimetry system captures the majority of particles, depositing all their energy. Neutrinos and muons, being exceptions, rarely interact with the detector.

Transverse momentum

transverse momentum is a fundamental concept related to the motion of particles within a collider or detector. It is a component of momentum that is perpendicular to the direction

of the particle's motion

$$p_T = \sqrt{p_x^2 + p_y^2} = P \sin\theta, \tag{2.25}$$

where p_x, p_y are the components of the particle's momentum in the transverse plane, P is the total momentum of the particle and $\theta \equiv \theta_{cm}$ is the angle between the direction of motion and the chosen axis (we choose to be z-axis).

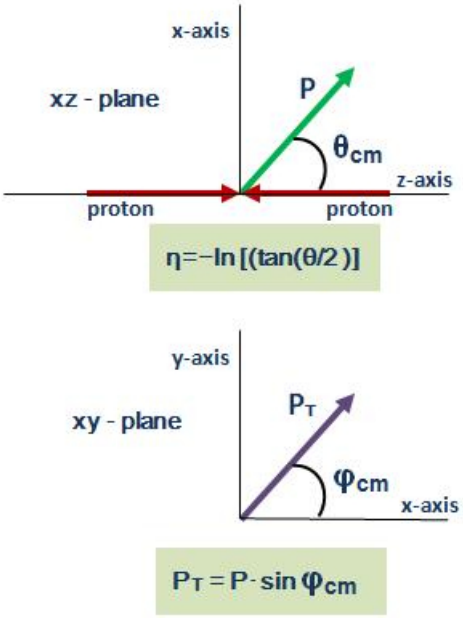

Figure 2.14: Definition of the longitudinal scattering angle ($\theta \equiv \theta_{cm}$) .

Pseudorapidity

Pseudorapidity η is a dimensionless variable used to describe the angular distribution of particles. It's defined as:

$$\eta = -\ln\left[\tan\left(\frac{\theta}{2}\right)\right], \tag{2.26}$$

where θ is the polar angle (angle measured from the particle's trajectory to the beamline) of the particle in a particle detector.

Pseudorapidity has some important characteristics:

- Pseudorapidity differences between particles are approximately invariant under Lorentz boosts (relativistic transformations), which is advantageous in many high-energy physics applications.

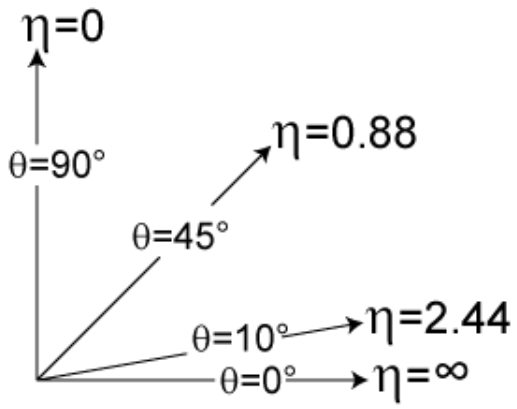

Figure 2.15: Pseudorapidity for various values of θ.

- It's independent of a particle's energy, i.e. unlike **rapidity** where experimental particle physicists often use a modified definition of rapidity relative to a beam axis

$$y = \frac{1}{2} \ln \left(\frac{E + p_z}{E - p_z} \right), \tag{2.27}$$

  where p_z is the component of momentum along the beam axis (the longitudinal momentum, this is also commonly denoted p_L).

Morever, the linear momentum could expressed as $P = (p_T, \eta, \varphi)$, where φ is the azimuthal angle. To derive Cartesian momenta (p_x, p_y, p_z) with the z-axis aligned along the beam axis, the following transformations are applied

$$p_x = p_T \cos\varphi \tag{2.28}$$

$$p_y = p_T \sin\varphi \tag{2.29}$$

$$p_z = p_T \sinh\eta\,. \tag{2.30}$$

Since the azimuthal angle is confined to planes perpendicular to the beam axis (z-axis) $\triangle\phi$ is invariant under boosts along the z-axis. So in the plane $\eta - \phi$ plane we define the quantity $(d \equiv \triangle R)$

$$d = \sqrt{(\triangle\eta)^2 + (\triangle\phi)^2}, \tag{2.31}$$

this represents the distance between two directions or particles (or jets) in the $\eta - \phi$ plane and is called the angular separation. Note that d is invariant under a boost transformation

along the beam line.

Energy and transverse energy

Transverse energy E_T is a component of the total energy that is perpendicular to the beamline direction. It is related to the transverse momentum (p_T) of a particle through the equation

$$E_T = \sqrt{p_T^2 + m^2}, \tag{2.32}$$

where p_T is the transverse momentum and m is the particle's rest mass. For massless particles the last equation will be $E_T = p_T$.

Missing transverse momentum $\overrightarrow{\not{p}}_T$ is a common observable that is built from the particles' momenta

$$\overrightarrow{\not{p}}_T \equiv -\sum_j \overrightarrow{p}_T, \tag{2.33}$$

missing transverse momentum is a 2-vector. **Missing transverse energy** $\not{E}_T$ is a corresponding quantity

$$\not{E}_T \equiv \left|\overrightarrow{\not{p}}_T\right|, \tag{2.34}$$

missing transverse energy (MET) is a scalar. Another quantity is H_T. Although there isn't a single definition for H_T, it often refers to the scalar sum of the transverse momentum that is lacking from some objects. For instance, we may see

$$H_T = \left|\sum_{jets\, j} \overrightarrow{p}^{\,j}_T\right|, \quad \text{or} \quad H_T = \sum_{jets\, j} \left|\overrightarrow{p}^{\,j}_T\right|, \quad \text{or} \quad H_T = \sum_{leptons\, j} \left|\overrightarrow{p}^{\,j}_T\right|. \tag{2.35}$$

The transverse mass is the best option when we are unable to determine all three components of momentum

$$m_T \equiv \sqrt{\left(E_T^1 + E_T^2\right)^2 - \left(p_T^1 + p_T^2\right)^2}, \tag{2.36}$$

where E_T is the transverse energy.

2.5.1 Missimg mass method

A collision is defined by its initial total energy and momentum, denoted as $(E_{in}, \overrightarrow{p}_{in})$. Following the collision the system transitions to a final state where n particles emerge each

contributing to a new total energy and momentum configuration. This transformation is crucial for understanding the outcomes and dynamics of the collision process in terms of the resulting particle distribution and their associated energy-momentum states

$$E = \sum_{i}^{n} E_i, \tag{2.37}$$

$$\overrightarrow{p} = \sum_{i}^{n} \overrightarrow{p}_i, \tag{2.38}$$

in certain experiments it is possible for the measured total energy (E) to be $E < E_{in}$ while the measured momentum ($\overrightarrow{p}$) to be $\overrightarrow{p} \neq \overrightarrow{p}_{in}$. This discrepancy suggests that one or more particles involved in the collision have gone undetected. This scenario is particularly common with neutral particles, such as neutrinos, as well as neutrons, π^0 particles, or K_L^0 particles. Neutrinos interact weakly with matter and can pass through detection systems without leaving a significant trace. To quantitatively analyze and account for undetected particles, we introduce the concept of "missing mass," providing a means to understand and incorporate the contributions of these elusive particles in the overall energy and momentum conservation analysis

$$\text{missing mass } \times c^2 = \sqrt{(E_{in} - E)^2 - (\overrightarrow{p}_{in} - \overrightarrow{p})^2 c^2}, \tag{2.39}$$

for each collision the missing mass is calculated and its spectrum is shown. If there is a distinct peak in the spectrum one particle has escaped our detector.

2.5.2 Invariant mass method

The invariant mass, a property reflecting the combined energy and momentum of an object or a system of objects, remains constant regardless of the reference frame. When the entire system is at rest, the invariant mass equals the total energy of the system divided by c^2. In the case of a single particle system, this invariant mass is alternatively referred to as the rest mass

$$m^2c^4 = E^2 - \overrightarrow{p}^2 c^2, \tag{2.40}$$

for a system of N particles, we possess the following

$$W^2c^4 = \left(\sum_i^N E_i\right)^2 - \left(\sum_i^N \overrightarrow{p}\, c\right)^2, \tag{2.41}$$

where W represents the invariant mass of the particle undergoing decay. In the case of a particle with mass M decaying into two particles, $M \rightarrow 1+2$, so

$$M^2c^4 = (E_1+E_2)^2 - (\overrightarrow{p}_1 + \overrightarrow{p}_2)^2 c^2 = m_1^2c^4 + m_2^2c^4 + 2\left(E_1E_2 - \overrightarrow{p}_1.\overrightarrow{p}_2c^2\right) = (p_1+p_2)^2. \tag{2.42}$$

The statistical significance The statistical significance for each bin is calculated by employing the formula associated with the background-with-signal hypothesis. This involves assessing the significance of a signal within the context of an expected background. The significance measurement serves as an indicator of the strength and reliability of the signal in each specific bin of the data distribution. The formula for the significance (Z-score) can be expressed as [108]

$$Z = \sqrt{2\left((S+B)\ln\left(1+\frac{S}{B}\right) - S\right)}, \tag{2.43}$$

where $S = \mathcal{L}_{\text{int}} \times \epsilon \times \sigma_S$ is the number of events from a signal model, $B = \mathcal{L}_{\text{int}} \times \epsilon \times \sigma_B$ is the number of events from background processes, $\mathcal{L}_{\text{int}}$is the integrated luminosity, $\sigma_{S(B)}$ is the signal/background cross section and ϵ denotes the detection efficiency.

2.6 Madgraph and Root

MadGraph [125] is an event generator software package used for the generation of parton-level processes at the leading order (LO) and next-to-leading order in QCD. It is particularly well-known for its capabilities in calculating cross-sections and generating events for a wide range of processes involving strong force (QCD) and electroweak interactions. MadGraph plays a crucial role in simulating events that can be compared with experimental data from particle colliders such as the Large Hadron Collider (LHC). Its output is in the form of a *Les Houches* file [109], and can consequently be processed by a general purpose Monte Carlo for showering and hadronization. Pythia [127] is a multi-purpose simulator that can model two-to-two processes at LO but it is mainly employed for parton showering, including the the underlying event, hadronization and pile-up events. After the parton-level events are

generated by MadGraph, undergo parton showering, hadronization, and decay (by Pythia for example), the next step in the simulation chain is often the simulation of the detector response. Delphes [130] is a software framework commonly used for simulating the response of a generic particle detector to the final-state particles. Once the simulated events pass through Delphes, the output format is typically in a ROOT [129] file containing detailed information about the detected particles and their properties. ROOT (Remote Object Oriented Tools) is a powerful software framework developed at CERN for data analysis, statistical analysis and visualization. It provides a versatile and powerful environment for storing, manipulating, and analyzing large datasets. ROOT is particularly well-suited for experiments at particle accelerators like the LHC. It offers a wide range of functionalities, including tools for statistical analysis, histogramming, curve fitting, and 2D/3D visualization. ROOT also features a flexible and efficient data storage system, allowing users to store complex data structures, such as trees and histograms, in a ROOT file format. The framework is widely adopted in the high-energy physics community and has become an integral part of the software toolkit for experimental and theoretical researchers alike.

Chapter 3

Exploring the Higgs-Gauge Couplings at Leptonic Colliders, Analysis & Results

3.1 The Higgs-Gauge Bosons Couplings

In the SM, the global custodial $SU(2)$ symmetry in the Higgs and gauge sectors after the EWSB, ensures that the electroweak ρ parameter at tree level satisfies [120]

$$\rho = \frac{m_W^2}{m_Z^2 \cos^2\theta_W} = 1.00039 \pm 0.00019, \tag{3.1}$$

with θ_W is the Weinberg mixing angle and m_Z and m_W are the Z and W gauge boson masses. For generic SM extensions, the Higgs-gauge couplings could be modified either via mixtures or via significant radiative corrections, and the general Lagrangian that describes the Higgs-gauge interactions can be written as[1]

$$\mathcal{L}_{hVV} = g^{(1)}_{hVV} h V^\mu V_\mu + g^{(2)}_{hVV} \frac{h}{\upsilon} V^{\mu\nu} V_{\mu\nu} + g^{(3)}_{hVV} \frac{h}{\upsilon} V^{\mu\nu} \tilde{V}_{\mu\nu}, \tag{3.2}$$

with $\upsilon = 246.22\,\text{GeV}$ is the Higgs vev, $V^\mu = Z^\mu, W^\mu$ is the gauge field, $V^{\mu\nu}$ is the field strength and $\tilde{V}^{\mu\nu} = \frac{1}{2}\epsilon^{\mu\nu\alpha\beta} V_{\alpha\beta}$ its dual field. For the SM, we have $g^{(1)}_{hVV} = g^{SM}_{hVV} = 2m_V^2/\upsilon$,

[1] There exist other high-dimensional operators that are suppressed by powers of the new physics energy scale Λ, like the operator $\eta^{\mu\nu} V_{\mu\alpha} V_{\nu\beta} \partial^{[\alpha} \partial^{\beta]} h$ [27]. In this work, we consider the case of only non-vanishing $g^{(1)}_{hVV}$.

and $g^{(2)}_{hVV} = g^{(3)}_{hVV} = 0$ at tree-level. Here, we consider only possible modification of the first interaction term in eq. (3.2); where any BSM modification with respect to the SM can be parametrized by

$$\kappa_W = \frac{g^{(1)}_{hWW}}{g^{SM}_{hWW}},\ \kappa_Z = \frac{g^{(1)}_{hZZ}}{g^{SM}_{hZZ}}, \tag{3.3}$$

where κ_W and κ_Z are the scale factors [101], and the ratio of these factors $\lambda_{WZ} = \kappa_W/\kappa_Z$ could be a useful quantity that may give crucial information on the nature of EWSB and the electroweak properties of the h_{125} resonance. It also may help to derive the necessary information about the Higgs triple coupling [124]. While recent measurements by ATLAS and CMS of $h \to W^*W$ and $h \to Z^*Z$ decay rates or production for the h_{125} resonance are sensitive to the overall sign and magnitude of λ_{WZ} [17]. This has been shown that the combined measurements of the Higgs couplings and the ratio λ_{WZ} using the LHC Run-I gives [8]

$$\begin{aligned} &0.69 \lesssim |\kappa_W| \lesssim 1.13,\ 0.78 \lesssim |\kappa_Z| \lesssim 1.18,\ 0.58 \lesssim |\kappa_g| \lesssim 1.04, \\ &-1.10 \lesssim \lambda_{WZ} \lesssim -0.73 \quad or \quad 0.72 \lesssim \lambda_{WZ} \lesssim 1.10. \end{aligned} \tag{3.4}$$

While the LHC Run-II [20, 21, 39, 51], gives with 2σ C.L. [2]

$$\begin{aligned} &0.84 \lesssim |\kappa_W| \lesssim 1.38,\ 0.77 \lesssim |\kappa_Z| \lesssim 1.21,\ 0.88 \lesssim |\kappa_g| \lesssim 1.44, \\ &-1.39 \lesssim \lambda_{WZ} \lesssim -0.97 \quad or \quad 0.92 \lesssim \lambda_{WZ} \lesssim 1.37. \end{aligned} \tag{3.5}$$

Here, κ_g is defined as in eq. (3.3). In what follows, we assume both Yukawa and Higgs-gluon couplings are not modified with respect to the SM (i.e., $\kappa_f = \kappa_g = 1$), while the Higgs-gauge couplings could take any value the ranges defined in eq. (3.5). Within these ranges, we will investigate possible excess or lack of events in some final states at leptonic colliders.

[2] These values are considered within the assumption that there are no additional BSM contributions to the Higgs boson width, i.e., $\mathcal{B}_{BSM}(h) = \mathcal{B}_{inv}(h) + \mathcal{B}_{und}(h) = 0$, where $\mathcal{B}_{inv}(h)$ denotes the invisible Higgs branching ratio decay to DM or long lived particles that can escape detection inside the detectors, and $\mathcal{B}_{und}(h)$ denotes the decay to detectable BSM particles.

3.2 The HVV Couplings Signs

In order to identify the Higgs-gauge couplings signs, we propose the final states at the leptonic colliders: $h\nu\bar{\nu}$ @ 250 GeV [Fig. 3.1-a,b,c], hW^+W^- @ 500 GeV [Fig. 3.1-d,e,f] and ZW^+W^- @ 1 TeV [Fig. 3.2] (with $h \to b\bar{b}$, $Z \to jj$ and $W^- \to \ell^-\bar{\nu}$); at the corresponding luminosity at a leptonic collider such as the International Linear Collider (ILC) for both cases with and without polarized beams.

Due to the branching ratio values $\mathcal{B}(h \to b\bar{b}) = 58.09\,\%$, $\mathcal{B}(W \to \ell\bar{\nu}) = 21.34\,\%$ and

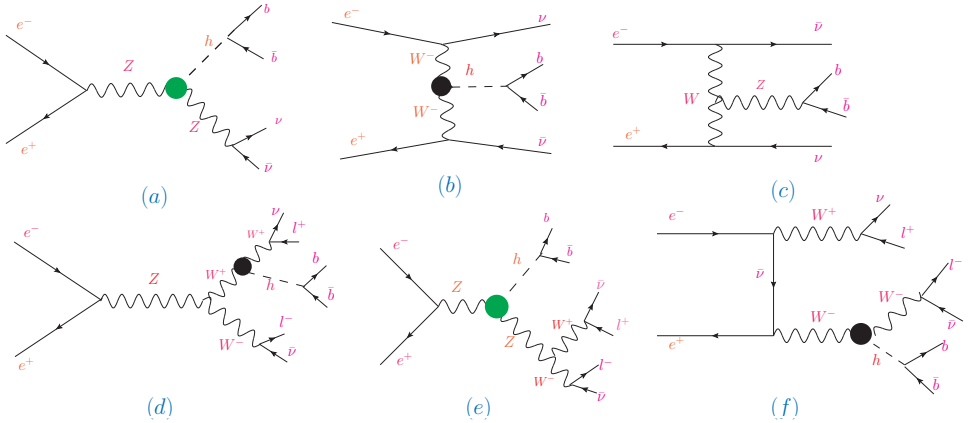

Figure 3.1: Some representative Feynman diagrams for the processes $h\nu\bar{\nu}$ @ 250 GeV (a, b) and hW^+W^- @ 500 GeV (d, e) are shown. Diagrams (c) and (f) illustrate examples of background contributions for the $h\nu\bar{\nu}$ and hW^+W^- channels, respectively. The black and green vertices denote the hWW and hZZ interactions, respectively.

$\mathcal{B}(Z \to jj) = 69.91\%$ [126], and the ILC b-tagging efficiency 80 %, the choice of final states $b\bar{b} + \not{E}_T$, $b\bar{b} + \ell^+\ell^- + \not{E}_T$ and $jj + \ell^+\ell^- + \not{E}_T$; is the best option, especially with the cross section values at the chosen CM energies as will be shown in Fig. 3.3. By changing the center-

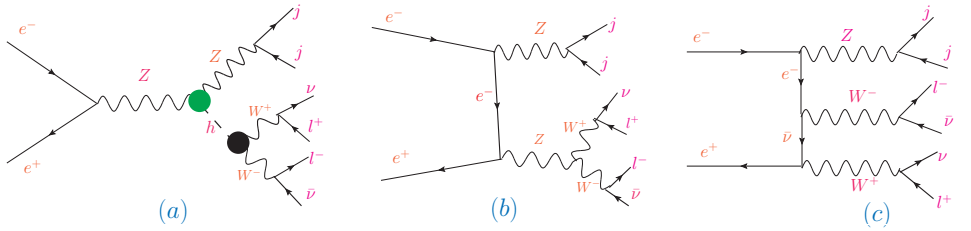

Figure 3.2: The Feynman diagram for the signal process ZW^+W^-(a), where the Higgs boson decays as $h \to b\bar{b}$ and the Z boson decays hadronically as $Z \to jj$. Diagrams (b) and (c) represent examples of background contributions. The black and green vertices indicate the hWW and hZZ interactions, respectively.

of-mass energy $\sqrt{s}$ from 250 GeV to 3 TeV, we get the cross section of $h\nu\bar{\nu}$, hW^+W^- and

ZW^+W^- processes with and without polarized beams as shown in Fig. 3.3. From Fig. 3.3,

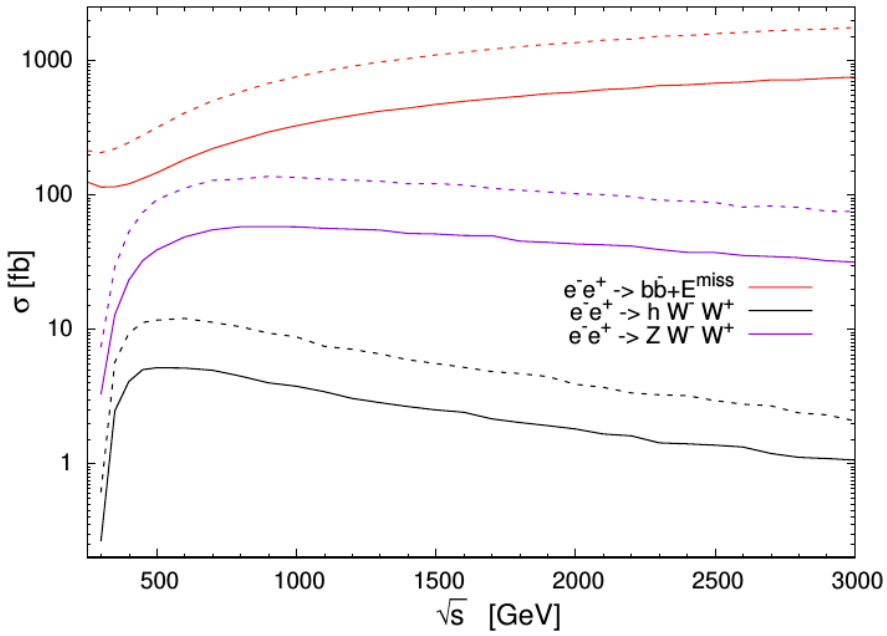

Figure 3.3: The cross section of $e^-e^+ \to h\nu\bar{\nu}$, $e^-e^+ \to hW^+W^-$ and $e^-e^+ \to ZW^+W^-$ processes as a function of $\sqrt{s}$, where the solid (dashed) line represents $P_{e^-,e^+} = [0,0]$ ($P_{e^-,e^+} = [-0.8,+0.3]$). Here, the cross section values are multiplied with the branching ratios of $h \to b\bar{b}$, $W \to \ell\bar{\nu}$ and $Z \to jj$.

one notices that cross section with polarized beams $P_{e^-,e^+} = [-0.8,+0.3]$ is greater than the case with unpolarized ones; by about twice, for the three processes. The reason is that the left-handed part of the vertex electron-positron-gauge bosons is always larger than the right-handed part, which increase the cross section up to 30 %. Indeed, if one considers the inverse polarization ($P_{e^-,e^+} = [+0.8,-0.3]$), the cross section values get decrease by 30 %. Therefore, this justifies the considered optin $P_{e^-,e^+} = [-0.8,+0.3]$. These possible interesting features for future lepton colliders like ILC [43] allow us to consider each final state at the corresponding CM energy as: **(1)** $e^-e^+ \to h\nu\bar{\nu}$ process at 250 GeV; even its cross section is larger for large CM energies, where the reason is to avoid the huge $t\bar{t}$ background. **(2)** the process $e^-e^+ \to hW^+W^-$ at 500 GeV; at which the cross section reaches its maximal value; and **(3)** similarly for the process $e^-e^+ \to ZW^+W^-$ at 1 TeV. These three final states have

the following backgrounds:

$$\begin{aligned} h\nu\bar{\nu}@\,250\,\text{GeV} &: WW,\, ZZ,\, jj + \not{E}_T \\ hW^+W^-\,@\,500\,\text{GeV} &: t\bar{t},\, t\bar{t}h,\, ZZh,\, WWZ,\, WWWW \\ ZW^+W^-\,@\,1\,\text{TeV} &: t\bar{t},\, t\bar{t}h,\, ZZh,\, WWh,\, WWWW. \end{aligned} \tag{3.6}$$

Parametrization of processes cross sections

The final states under consideration arise from multiple Feynman diagrams, some of which involve the Higgs-gauge boson couplings hWW and hZZ (as shown in Fig. 3.1 and Fig. 3.2). Consequently, their total cross sections can be expressed as a polynomial in the coupling modifiers κ_W and κ_Z:

$$\sigma(\kappa_W, \kappa_Z) = \sum_{n,m} \sigma_{[n,m]}\, \kappa_W^n \kappa_Z^m. \tag{3.7}$$

In the SM limit, corresponding to $\kappa_W = \kappa_Z = 1$, the cross section reduces to:

$$\sigma^{\text{SM}} = \sigma(1,1) = \sum_{n,m} \sigma_{[n,m]}. \tag{3.8}$$

To probe the effects of potential deviations from the SM values of the Higgs-gauge couplings ($\kappa_W, \kappa_Z \neq 1$), we define the amplitudes for each process and express the total cross sections as explicit functions of these parameters.

$e^-e^+ \to b\bar{b}\nu\bar{\nu}$ Process

The total amplitude is decomposed as:

$$\mathcal{M}_{\text{total}} = \kappa_W\, \mathcal{M}_W + \kappa_Z\, \mathcal{M}_Z + \mathcal{M}_0, \tag{3.9}$$

where:

- $\mathcal{M}_W$: amplitude from diagrams involving the SM hWW vertex (Fig. 3.1-b),
- $\mathcal{M}_Z$: amplitude from diagrams involving the SM hZZ vertex (Fig. 3.1-a),
- $\mathcal{M}_0$: SM background amplitude (diagrams without hWW or hZZ couplings).

Squaring the amplitude yields:

$$|\mathcal{M}_{\text{total}}|^2 = \kappa_W^2|\mathcal{M}_W|^2 + \kappa_Z^2|\mathcal{M}_Z|^2 + |\mathcal{M}_0|^2 + 2\kappa_W\kappa_Z\,\text{Re}(\mathcal{M}_W\mathcal{M}_Z^*) + 2\kappa_W\,\text{Re}(\mathcal{M}_W\mathcal{M}_0^*) + 2\kappa_Z\,\text{Re}(\mathcal{M}_Z\mathcal{M}_0^*). \tag{3.10}$$

Accordingly, the total cross section is:

$$\sigma(\kappa_W,\kappa_Z) = \kappa_W^2\sigma_W + \kappa_Z^2\sigma_Z + \kappa_W\kappa_Z\,\sigma_{WZ}^{\text{int}} + \kappa_W\,\sigma_{W0}^{\text{int}} + \kappa_Z\,\sigma_{Z0}^{\text{int}} + \sigma_0. \tag{3.11}$$

Here, σ_W and σ_Z are the contributions from pure Higgs-mediated diagrams, σ_0 is the pure background, and the remaining terms represent interference between the different contributions.

$e^-e^+ \to hW^+W^-$ Process

At tree level, this process proceeds only through diagrams involving the hWW and hZZ couplings. The total amplitude is:

$$\mathcal{M}_{\text{total}} = \kappa_W\,\mathcal{M}_W + \kappa_Z\,\mathcal{M}_Z. \tag{3.12}$$

Squaring this yields:

$$|\mathcal{M}_{\text{total}}|^2 = \kappa_W^2|\mathcal{M}_W|^2 + \kappa_Z^2|\mathcal{M}_Z|^2 + 2\kappa_W\kappa_Z\,\text{Re}(\mathcal{M}_W\mathcal{M}_Z^*). \tag{3.13}$$

Thus, the total cross section is:

$$\sigma(\kappa_W,\kappa_Z) = \kappa_W^2\sigma_W + \kappa_Z^2\sigma_Z + \kappa_W\kappa_Z\,\sigma_{WZ}^{\text{int}}. \tag{3.14}$$

$e^-e^+ \to ZW^+W^-$ Process

In this case, only one tree-level diagram involves both hWW and hZZ vertices simultaneously—the so-called Higgs-strahlung diagram. We write the total amplitude as:

$$\mathcal{M}_{\text{total}} = \kappa_W\kappa_Z\,\mathcal{M}_{WZ} + \mathcal{M}_0, \tag{3.15}$$

where $\mathcal{M}_{WZ}$ is the amplitude from the unique Higgs diagram, and $\mathcal{M}_0$ is the SM background amplitude. Squaring gives:

$$|\mathcal{M}_{\text{total}}|^2 = \kappa_W^2 \kappa_Z^2 \, |\mathcal{M}_{WZ}|^2 + 2\kappa_W \kappa_Z \, \text{Re}(\mathcal{M}_{WZ} \mathcal{M}_0^*) + |\mathcal{M}_0|^2. \tag{3.16}$$

Hence, the cross section is:

$$\sigma(\kappa_W, \kappa_Z) = \kappa_W^2 \kappa_Z^2 \, \sigma_{WZ} + 2\kappa_W \kappa_Z \, \sigma_{WZ0}^{\text{int}} + \sigma_0. \tag{3.17}$$

Using Madgraph5 [125] at the partonic level, we generate each process for both unpolarized and $P_{e^-,e^+} = [-0.8, +0.3]$, where the effects from initial state radiation (ISR) and beamstrahlung are not included. The cross section values is estimated by considering the following preselection criteria, that are applied at partonic level

$$\triangle R_{\alpha,\beta} > 0.4, \; |\eta_\alpha| < 2.5 \, (\alpha, \beta = b, j, \ell), \; p_T^{b,j} > 20 \, \text{GeV}, \; p_T^{\ell} > 10 \, \text{GeV}, \; \not{E}_T > 10 \, \text{GeV}. \tag{3.18}$$

By using both polatrized and unpolarized e^-e^+ beams, we estimate different cross section contributions $\sigma_{[n,m]}$ used in eq. (3.7), for the three processes[3]. In table (3.1), we give the non-vanishing cross section contributions $\sigma_{[n,m]}$, for unpolarized and polarized beams.

	$h\nu\bar{\nu}$ $P_{e^-,e^+} = [0,0]$	$h\nu\bar{\nu}$ $P_{e^-,e^+} = [-0.8,+0.3]$	hW^+W^- $P_{e^-,e^+} = [0,0]$	hW^+W^- $P_{e^-,e^+} = [-0.8,+0.3]$	ZW^+W^- $P_{e^-,e^+} = [0,0]$	ZW^+W^- $P_{e^-,e^+} = [-0.8,+0.3]$
$\sigma_{[0,0]}$	60.788	109.297	-	-	59.268	134.931
$\sigma_{[0,1]}$	-1.549	-1.262	-	-	-	-
$\sigma_{[1,0]}$	-1.565	-2.661	-	-	-	-
$\sigma_{[1,1]}$	2.358	2.682	-1.194	-2.458	-1.388	-1.934
$\sigma_{[2,0]}$	7.221	15.821	5.927	13.380	-	-
$\sigma_{[0,2]}$	35.853	52.873	0.582	1.073	-	-
$\sigma_{[2,2]}$	-	-	-	-	0.584	0.792

Table 3.1: The contributions to the cross section according to eq. (3.7); for the considered final states at the correspondings CM energies without and with polarized beams. Here, all cross section values are given in fb.

One sees from table. (3.1) that in the case where the processes occur a Feynman diagram that does not involve hWWor hZZ vertices then the cross sections ($\sigma_{[0,0]}$) is dominated by this contribution (for $e^-e^+ \to h\nu\bar{\nu}$ and $e^-e^+ \to ZW^+W^-$). The SM cross section valuesfor unpolarized/polarized beams are 65.98 fb/ 113.12 fb, ($e^-e^+ \to h\nu\bar{\nu}$) 5.31 fb/ 11.99 fb ($e^-e^+ \to hW^+W^-$) and 58.46 fb/ 133.79 fb ($e^-e^+ \to ZW^+W^-$). One notices also that the

[3]Here, the b-tagging efficiency is considered to be the ILC value , $\varepsilon_b = 0.8$.

interferences are destructive in all processes except the contribution $\sigma_{[1,1]}$ of $e^-e^+ \to b\bar{b} + \not{E}_T$ process. By varying both κ_W and κ_Z within the range in eq. (3.5), and using eq. (3.7) we found the cross sections for unpolarized/polarized beams (Fig. 3.4/Fig. 3.5) and its relative difference for unpolarized/polarized beams with respect to the SM (Fig. 3.6/ Fig. 3.7). In

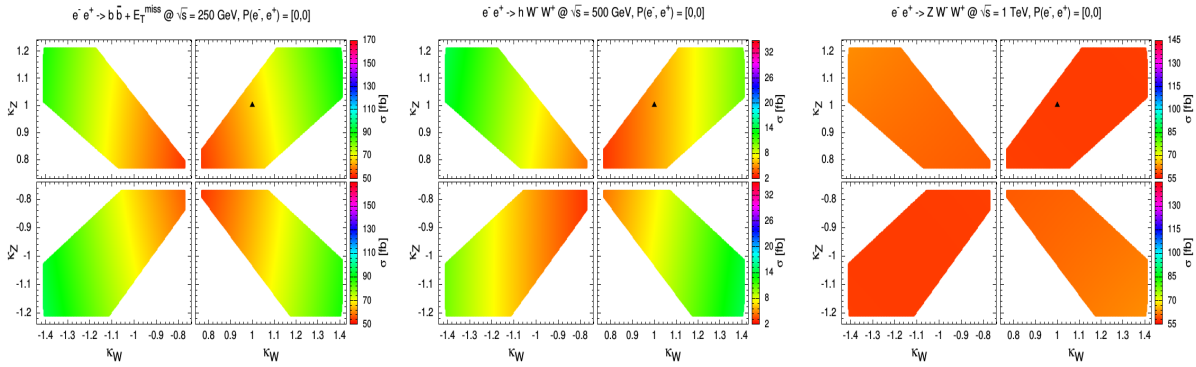

Figure 3.4: The cross sections (in the palette) of the three processes in the $\kappa_W - \kappa_Z$ plan without polarization. The triangle (▲) refers to the SM case.

Fig.(3.4 and 3.5) we display the total cross sections for the three processes $e^-e^+ \to h\nu\bar{\nu}$ (left), $e^-e^+ \to hW^+W^-$ (middle) and $e^-e^+ \to ZW^+W^-$ (right) without and with beam polarization as function of κ_W and κ_Z surviving (from constraints of eq. (3.5)). The cross section of $e^-e^+ \to hW^+W^-$ process have the most large sensitivity to hWW and hZZ couplings (almost all palette colours are present polarized case) because all its Feynman's diagrams involve hWW and/or hZZ vertices. While $e^-e^+ \to h\nu\bar{\nu}$ process although its cross section is the largest (from $\sim 50\,fb$ to $90\,fb$ and from $\sim 90\,fb$ to $170\,fb$ for the cases unpolarized and polarized beams, respectively) where we see less sensitivity and this is due to the presence of several Feynman diagrams that do not contain any contribution.

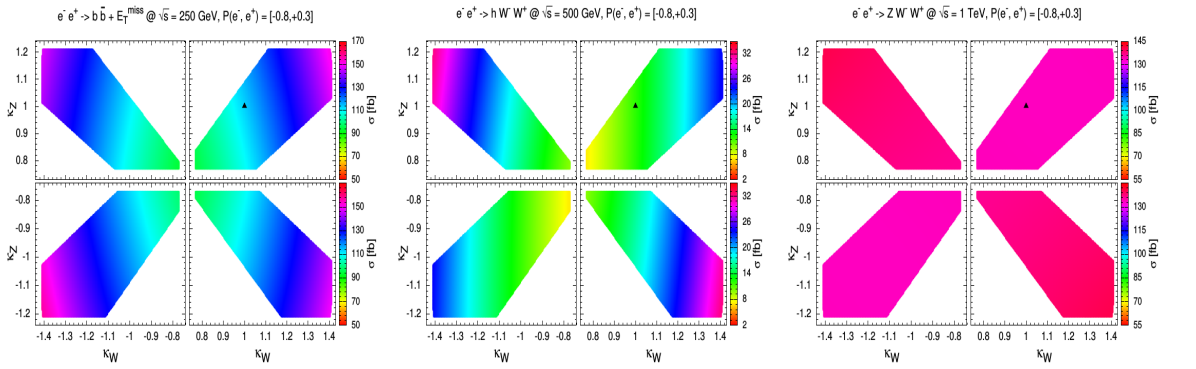

Figure 3.5: The cross sections (in the palette) of the three processes in the $\kappa_W - \kappa_Z$ plan with polarization. The triangle (▲) refers to the SM case.

Moreover, the $e^-e^+ \to ZW^+W^-$ process is almost insensitive to κ_W and κ_Z (same colour), and this is that the process has only one Feynman's diagram including the hWW and hZZ vertices at the same time. It can also be observed, in all processes, that when κ_W and κ_Z have a different sign the sensitivity of the two couplings are greater than when they have the same sign. Besides the results of cross sections shown in Fig.(3.4 and 3.5), we can also present

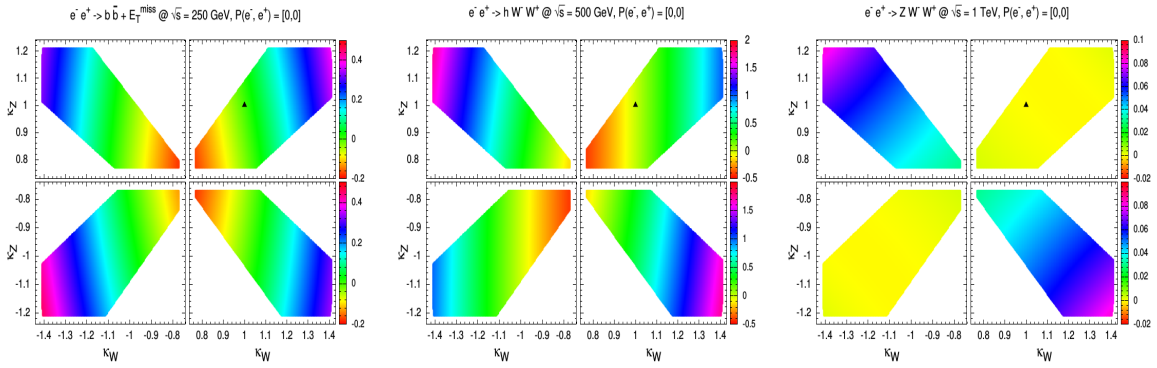

Figure 3.6: The cross section relative difference with respect to the SM ($\kappa_W = \kappa_Z = 1$) (shown in the palette) for the three processes in the $\kappa_W - \kappa_Z$ plan without polarization.

the cross section relative difference with respect to the SM ($[\sigma(\kappa_W, \kappa_Z) - \sigma(1,1)]/\sigma(1,1)$) in the $\kappa_W - \kappa_Z$ plan for the three processes as it is depicted in Fig.(3.6 and 3.7). One could notice that the largest ratio was recorded for a different sign of κ_W and κ_Z in the $e^-e^+ \to hW^+W^-$ and $e^-e^+ \to ZW^+W^-$ processes and this is what will appear in the kinematic distributions. While the effect of the sign is almost the same on $e^-e^+ \to h\nu\bar{\nu}$ process. As a confirmation of

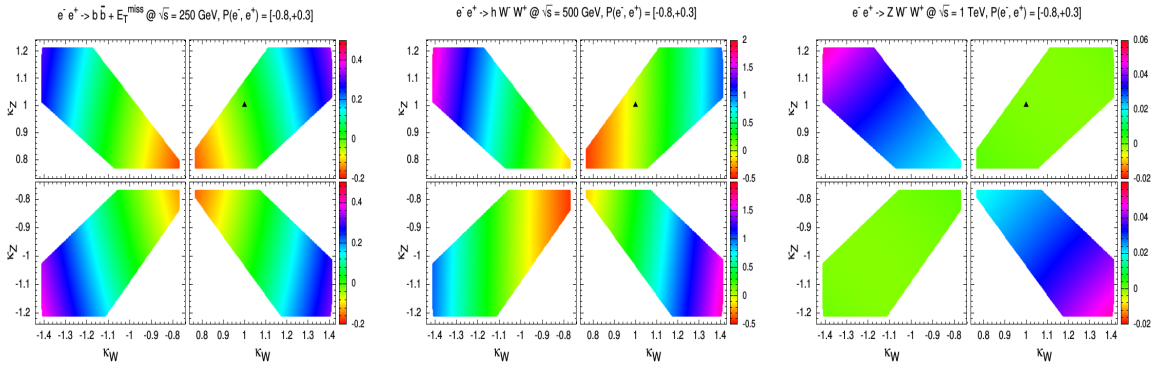

Figure 3.7: The cross section relative difference with respect to the SM ($\kappa_W = \kappa_Z = 1$) (shown in the palette) for the three processes in the $\kappa_W - \kappa_Z$ plan with polarization.

the previous result, the effect of κ_W and κ_Z on the hW^+W^- production is the greatest (the ratio is up to 200 %), then on the $h\nu\bar{\nu}$ final state (approximately 50 %) however it does not exceed 10 % for the ZW^+W^- production.

3.3 Analysis & Results

The possible precision in the measurments of κ_W and κ_Z at the HL-LHC with an integrated luminosity of 3 ab^{-1}, are expected to be $\delta\kappa_W/\kappa_W \leq 5\,\%$, $\delta\kappa_Z/\kappa_Z \leq 4\,\%$, respectively [40]. Then, in order to derive any useful information from such colliders particularly promising leptonic colliders, it is crucial to consider modified hVV couplings just below the LHC reach, i.e., $|\kappa_V| - 1 = \pm 0.04$, whith many possible signs. However, since the expected deviation is not large, one needs first to find probable optimal cuts using the SM case $\kappa_V = 1$ signal (SM-signal) process where the signal event number is $N_s = \sigma(\kappa_W = \kappa_Z = 1) \times \mathcal{L}$, with $\sigma(\kappa_W, \kappa_Z)$ is the cross section and $\mathcal{L}$ is the integrated luminosity. Here we generate both signals and backgrounds using the package Madgraph5 [125], while the packages Pythia8.2 [127, 128] and Delphes-root [129, 130] are adopted for parton shower and detector simulation, respectively. The jets are reconstructed by performing FastJet3.3 [131, 132] with the anti-kt algorithm [133]. Table (3.2) resume cross section values for the considered processes and thier backgrounds. one could remarks the relevant backgrounds for each process, which are $W^+W^- \to b\bar{b}\nu\bar{\nu}$ **(the dominant one),** $ZZ\,(Z \to b\bar{b}, Z \to \nu\bar{\nu})$ and $jj + \not{E}_T$ for $h\nu\bar{\nu} \to b\bar{b} + \not{E}_T$ final state; $t\bar{t}$ **(the dominant one),** $t\bar{t}h$, W^+W^-Z, ZZh and $WWWW$ for the final state $hW^+W^-\,(h \to b\bar{b})$ while W bosons decay semi-leptonically; $t\bar{t}$ **(the dominant one),** $t\bar{t}h$, W^+W^-h, ZZh and $WWWW$ for the final state $ZW^+W^-\,(Z \to jj)$ with W bosons decay semi-leptonically. The dominant decay channel for h ($m_h = 125.09\,\text{GeV}$) in the signal process is $h \to b\bar{b}$, with a 58.09 % [126] branching fraction and the b-tagging efficiency is 80 % and the relevant cross section at the center of masses 250 GeV-ILC; 500 GeV-ILC and 1 TeV-ILC [106] making these final states interesting. The pre-cuts in (3.18) are imposed at the generator level and we perform the analysis by considering the above mentioned integrated luminosity for each process.

We may see also the hVV sign effect on the kinematic distributions as an excess or a lack in the events, for the three final states $h\nu\bar{\nu} \to b\bar{b} + \not{E}_T$ @ 250 GeV, $hW^+W^- \to b\bar{b} + \ell^+\ell^- + \not{E}_T$ @ 500 GeV; and $ZW^+W^- \to jj + \ell^+\ell^- + \not{E}_T$ @ 1 TeV. In order to have an idea about the thier shape (distributions), we show in Fig. 3.8 and Fig. 3.9 some kinematic variables distributions versus number of events for each final states $b\bar{b} + \not{E}_T$, $hW^+W^- \to b\bar{b} + \ell^+\ell^- + \not{E}_T$, and $ZW^+W^- \to jj + \ell^+\ell^- + \not{E}_T$, among the produced kinematic variables distributions which bear a clear indication of the final states, we mention:

- $\not{E}_T$; The missing transverse energy.

	$\sigma\,[fb]$
W^-W^+	3.313×10^3
ZZ	42.588
$jj + \not{E}_T$	73.315
$\boldsymbol{h\nu\bar{\nu}}$	**102.401**
$t\bar{t}$	22.712
$t\bar{t}h$	9.203×10^{-3}
ZZh	7.402×10^{-3}
WWZ	1.009
$WWWW$	2.850×10^{-3}
$\boldsymbol{hW^+W^-}$	**0.168**
$t\bar{t}$	7.306
$t\bar{t}h$	7.783×10^{-2}
ZZh	1.056×10^{-2}
WWh	0.142
$WWWW$	6.348×10^{-2}
$\boldsymbol{ZW^+W^-}$	**1.458**

Table 3.2: The cross section values for $h\nu\bar{\nu}$, hW^+W^- and ZW^+W^- final states at the ILC luminosity 250 fb^{-1}, 500 fb^{-1} and 1000 fb^{-1}respectively. Here, the The bold lines represent the signal and the other lines represent the different background contributions.

• p_T^{bb} $\left(p_T^{jj}\right)$; The transverse momentum for leading and sub-leading b-jet (jet).

• E_T^{bb} $\left(E_T^{jj}\right)$; The transverse energy for leading and sub-leading b-jet (jet).

• M_{bb} (M_{jj}) $(M_{\ell\ell})$; The invariant mass of the leading b-jet and sub-leading b-jet (jet) (lepton).

• ΔR_{bb} $(\Delta R_{j_n j_m})$ $(\Delta R_{\ell_n \ell_m})$; Relative distance between two particles, leading and sub-leading b-jet (jets) (leptons) and their combinations, n and m stands from 1 to 2.

It is clear and in all cases that the SM-signal, represented by the black line, stands out from the backgrounds in events number, the greatest prominence is represented in $ZW^+W^- \to jj + \ell^+\ell^- + \not{E}_T$ process and for all kinematic variables distributions shown. In $h\nu\bar{\nu} \to b\bar{b} + \not{E}_T$ process, the appearance of the SM-signal is less, while in the process $hW^+W^- \to b\bar{b} + \ell^+\ell^- + \not{E}_T$, the prominence is very tiny. Also one could note that the SM-signal prominence is similar, that is, the same increase in all variables, and this is for the three processes, its means that new physics could be reached by considering hVV modified couplings with respect to the SM at particles colliders, especially where new upgrade/construct in the center of mass energies and high luminosity will be offered.

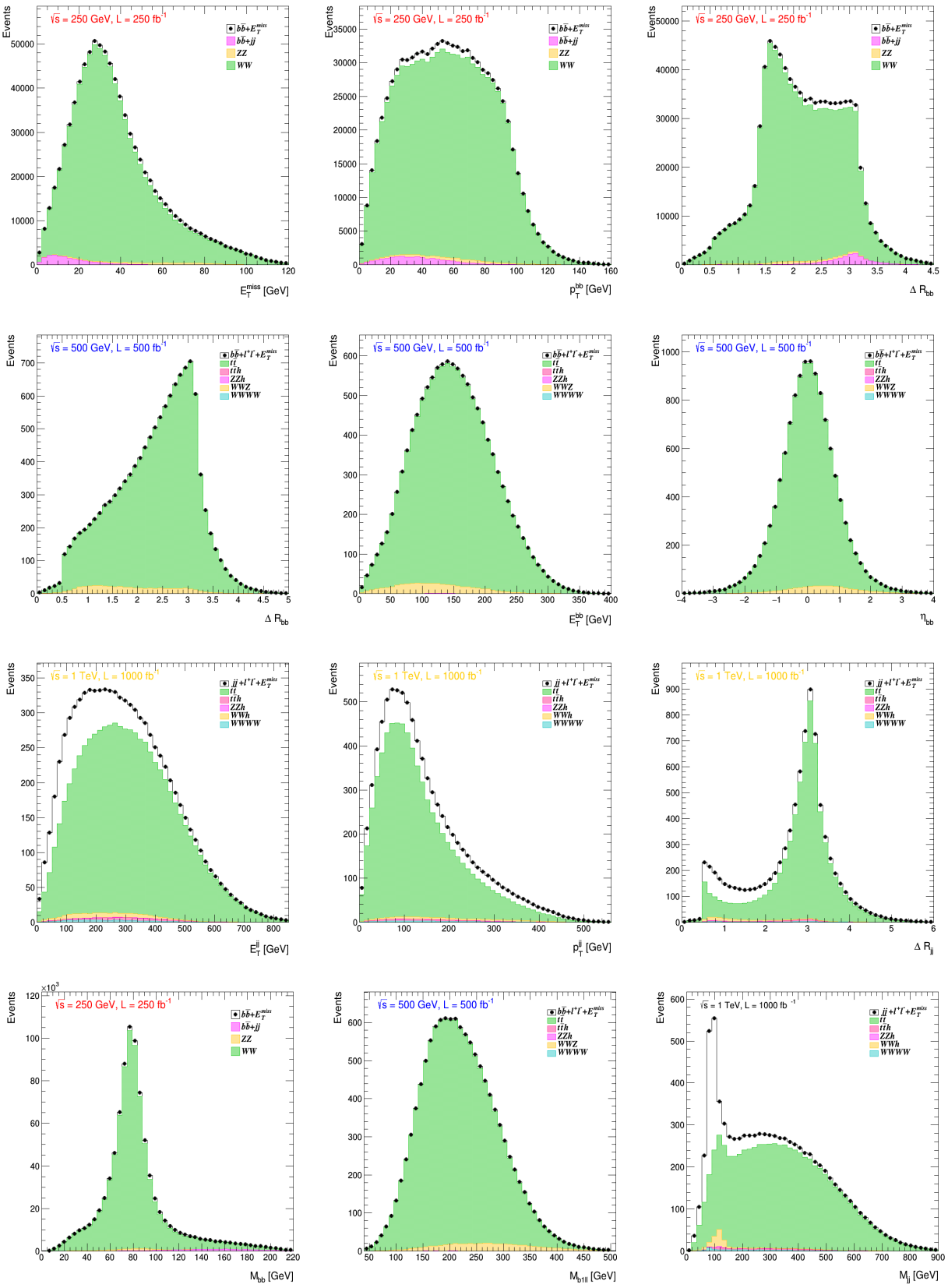

Figure 3.8: Some kinematic variables distributions as function of number of events for signals and backgrouds of the final states $h\nu\bar{\nu} \to b\bar{b} + \not{E}_T$ @ 250 GeV, $hW^+W^- \to b\bar{b} + \ell^+\ell^- + \not{E}_T$ @ 500 GeV; and $ZW^+W^- \to jj + \ell^+\ell^- + \not{E}_T$ @ 1 TeV. Here all distributions are produced from root-delphes output files.

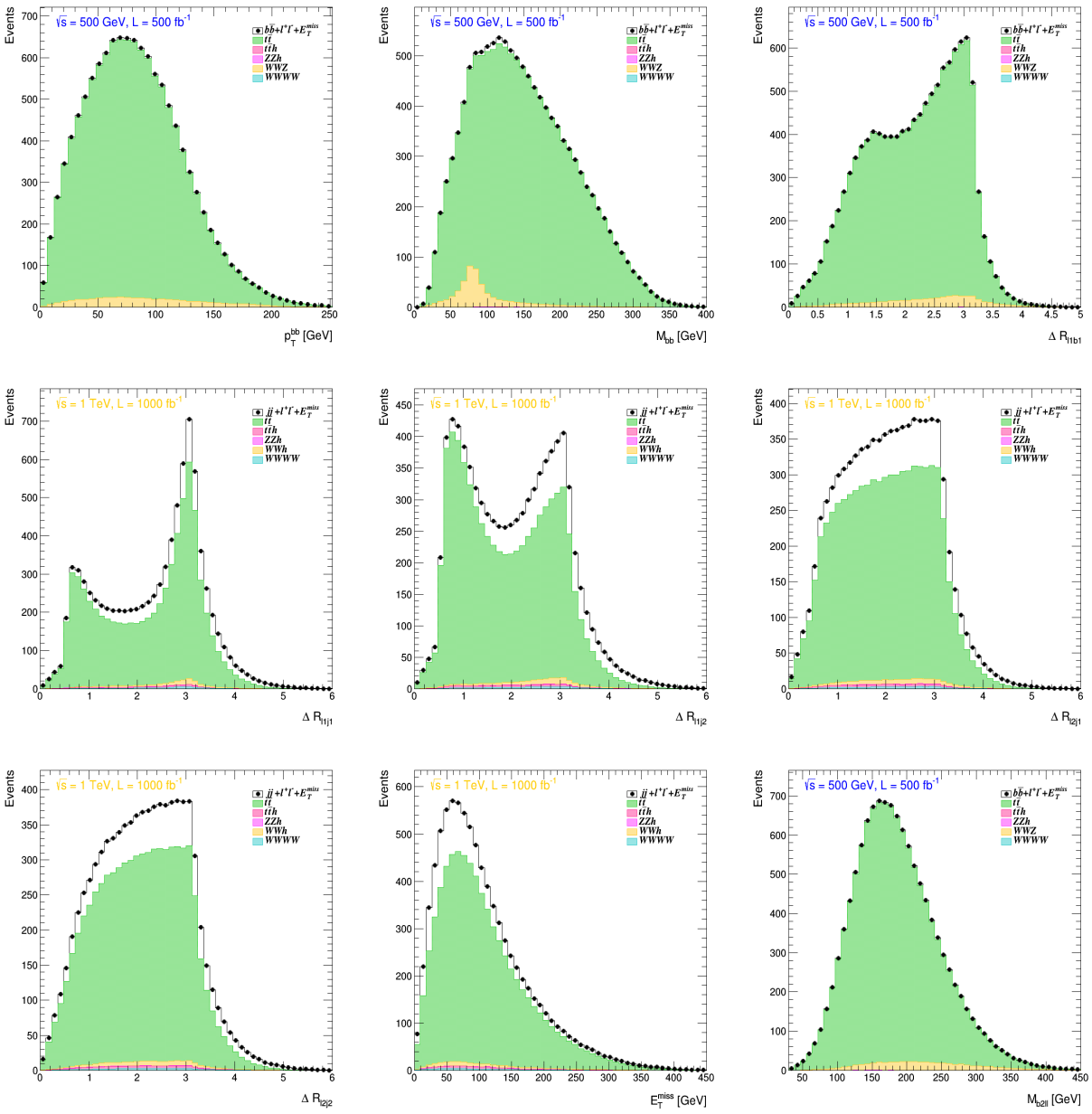

Figure 3.9: Other kinematic variables distributions as function of number of events for signals and backgrouds of the final states $h\nu\bar{\nu} \to b\bar{b} + \not{E}_T$ @ 250 GeV, $hW^+W^- \to b\bar{b} + \ell^+\ell^- + \not{E}_T$ @ 500 GeV; and $ZW^+W^- \to jj + \ell^+\ell^- + \not{E}_T$ @ 1 TeV. Here all distributions are produced from root-delphes output files.

Summary and Conclusions

The independent determination of the Higgs boson couplings to W and Z bosons is essential for scrutinizing the properties of the Higgs boson—thus, for precision tests of the Standard Model and the search for potential new physics. In this study, we have investigated three relevant processes at e^-e^+ colliders—with and without polarized beams $P_{e^-,e^+} = [-0.8, +0.3]$—to probe the hWW and hZZ couplings:

- $e^-e^+ \to b\bar{b} + \not{E}_T$ at $\sqrt{s} = 250\,\text{GeV}$,
- $e^-e^+ \to hW^+W^- \to b\bar{b} + \ell^+\ell^- + \not{E}_T$ at $\sqrt{s} = 500\,\text{GeV}$,
- $e^-e^+ \to ZW^+W^- \to jj + \ell^+\ell^- + \not{E}_T$ at $\sqrt{s} = 1\,\text{TeV}$.

As a first result, we present the cross sections for the three considered processes as a function of center-of-mass energy for both unpolarized and polarized beams. These channels involve Feynman diagrams that depend on the hWW and/or hZZ couplings, making their total cross sections sensitive to the coupling modifiers κ_W and κ_Z. We parametrize the total cross section of each process using the corresponding powers κ_W^n and κ_Z^m.

By taking into account the recent combined measurements from the LHC Run-II on κ_W and κ_Z, we identified a range of allowed values for both the magnitude and sign of κ_W and κ_Z. However, current measurements cannot determine the sign of $\lambda_{WZ} = \kappa_W/\kappa_Z$. It is worth mentioning that extracting these allowed κ values has not always been straightforward.
We then presented the cross sections in the κ_W–κ_Z plane and highlighted their relative deviations from the SM expectation. Among the three processes, the $hW^+W^- \to b\bar{b} + \ell^+\ell^- + \not{E}_T$ final state demonstrated the highest sensitivity to such deviations.

Kinematic distributions (observables) were analyzed under the SM-like scenario $\kappa_W = \kappa_Z = 1$ at different projected luminosities for the International Linear Collider (ILC): $250\,\text{fb}^{-1}$, $500\,\text{fb}^{-1}$, and $1000\,\text{fb}^{-1}$. These observables exhibit strong discriminating power even when

the total rates appear SM-like, emphasizing the importance of high-precision measurements.

Future work can greatly benefit from the incorporation of advanced multivariate techniques and machine learning algorithms such as Boosted Decision Trees (BDTs) [135] and Deep Neural Networks (DNNs) [136], implemented within the Toolkit for Multivariate Data Analysis (`TMVA`) [134]. These techniques are expected to significantly enhance signal-background separation, particularly in complex final states.

Furthermore, this analysis framework can be enriched by considering Beyond the Standard Model (BSM) theories. For example:

- The Standard Model Effective Field Theory (SMEFT) [137], which introduces higher-dimensional operators that modify Higgs-gauge couplings.
- Higgs sector extensions, such as the Two-Higgs-Doublet Model (2HDM) [138], where additional scalar states and altered couplings can lead to observable deviations.

Finally, these studies will be highly relevant at future and upgraded colliders such as the ILC, FCC-ee, CEPC, and CLIC, which aim to perform precision Higgs measurements and probe BSM phenomena through deviations in Higgs-gauge interactions.

Appendix A

MadGraph codes

A.1 The cross section of $e^-e^+ \to h\nu\bar{\nu}$, $e^-e^+ \to hW^+W^-$ and $e^-e^+ \to ZW^+W^-$ processes as a function of $\sqrt{s}$

This is the code used to calculate the cross section versus center-of-mass energy for the processes $e^+e^- \to b\bar{b}\nu\bar{\nu}$, $e^+e^- \to hW^+W^-$, and $e^+e^- \to ZW^+W^-$, considering both unpolarized/polarized beams.

```
import model smm
generate e- e+ > b b~ vl vl~
output eebb-pcm
launch
set aa 1 ! represent kappa_W
set bb 1 ! represent kappa_Z
set nevent 1000 ! the number of events
set ebeam1 250  ! beam 1 energy in GeV
set ebeam2 250  ! beam 2 energy in GeV
set polbeam1 0.0 ! beam polarization for beam 1 unpolarized/-0.8 polarized
set polbeam2 0.0 ! beam polarization for beam 2 unpolarized/0.3 polarized
launch
set ebeam1 350
set ebeam2 350
launch
set ebeam1 450
set ebeam2 450
```

```
launch
set ebeam1 500
set ebeam2 500
launch
set ebeam1 600
set ebeam2 600
launch
set ebeam1 700
set ebeam2 700
launch
set ebeam1 800
set ebeam2 800
launch
set ebeam1 900
set ebeam2 900
launch
set ebeam1 1000
set ebeam2 1000
launch
set ebeam1 1100
set ebeam2 1100
launch
set ebeam1 1200
set ebeam2 1200
launch
set ebeam1 1300
set ebeam2 1300
launch
set ebeam1 1400
set ebeam2 1400
launch
set ebeam1 1500
set ebeam2 1500
```

A.2 Run cards for processes

Here we present the run card used by MadGraph during the generation of event files. It contains the modified couplings κ_W and κ_Z.

```
###################################################################
## PARAM_CARD AUTOMATICALY GENERATED BY MG5 FOLLOWING UFO MODEL   ####
###################################################################
##                                                                ##
##  Width set on Auto will be computed following the information    ##
##        present in the decay.py files of the model.              ##
##        See  arXiv:1402.1178 for more details.                   ##
##                                                                ##
###################################################################

#####################################
## INFORMATION FOR MASS
#####################################
Block mass
    5 4.700000e+00 # MB
    6 1.730000e+02 # MT
   15 1.777000e+00 # MTA
   23 9.118800e+01 # MZ
   25 1.250000e+02 # MH
## Dependent parameters, given by model restrictions.
## Those values should be edited following the
## analytical expression. MG5 ignores those values
## but they are important for interfacing the output of MG5
## to external program such as Pythia.
  1 0.000000 # d : 0.0
  2 0.000000 # u : 0.0
  3 0.000000 # s : 0.0
  4 0.000000 # c : 0.0
  11 0.000000 # e- : 0.0
  12 0.000000 # ve : 0.0
  13 0.000000 # mu- : 0.0
  14 0.000000 # vm : 0.0
```

```
  16 0.000000 # vt : 0.0
  21 0.000000 # g : 0.0
  22 0.000000 # a : 0.0
  24 80.419002 # w+ : cmath.sqrt(MZ__exp__2/2. + cmath.sqrt(MZ__exp__4/4. \\
- (aEW*cmath.pi*MZ__exp__2)/(Gf*sqrt__2)))

###################################
## INFORMATION FOR SMINPUTS
###################################
Block sminputs
    1 1.325070e+02 # aEWM1
    2 1.166390e-05 # Gf
    3 1.180000e-01 # aS
    4 0.000000     # aa
    5 0.000000     # bb

###################################
## INFORMATION FOR YUKAWA
###################################
Block yukawa
    5 4.700000e+00 # ymb
    6 1.730000e+02 # ymt
   15 1.777000e+00 # ymtau

###################################
## INFORMATION FOR DECAY
###################################
DECAY   6 1.491500e+00 # WT
DECAY  23 2.441404e+00 # WZ
DECAY  24 2.047600e+00 # WW
DECAY  25 6.382339e-03 # WH
## Dependent parameters, given by model restrictions.
## Those values should be edited following the
## analytical expression. MG5 ignores those values
## but they are important for interfacing the output of MG5
## to external program such as Pythia.
```

```
DECAY  1 0.000000 # d : 0.0
DECAY  2 0.000000 # u : 0.0
DECAY  3 0.000000 # s : 0.0
DECAY  4 0.000000 # c : 0.0
DECAY  5 0.000000 # b : 0.0
DECAY  11 0.000000 # e- : 0.0
DECAY  12 0.000000 # ve : 0.0
DECAY  13 0.000000 # mu- : 0.0
DECAY  14 0.000000 # vm : 0.0
DECAY  15 0.000000 # ta- : 0.0
DECAY  16 0.000000 # vt : 0.0
DECAY  21 0.000000 # g : 0.0
DECAY  22 0.000000 # a : 0.0
```

List of References

[1] G. Aad *et al.* [ATLAS Collaboration], "Observation of a new particle in the search for the Standard Model Higgs boson with the ATLAS detector at the LHC," Phys. Lett. B **716**, 1 (2012) [arXiv:1207.7214 [hep-ex]].

[2] S. Chatrchyan *et al.* [CMS Collaboration], "Observation of a New Boson at a Mass of 125 GeV with the CMS Experiment at the LHC," Phys. Lett. B **716**, 30 (2012) [arXiv:1207.7235 [hep-ex]].

[3] P. Sikivie, L. Susskind, M. B. Voloshin and V. I. Zakharov, "Isospin Breaking in Technicolor Models," Nucl. Phys. B **173**, 189 (1980).

[4] [ATLAS Collaboration], "Combined coupling measurements of the Higgs-like boson with the ATLAS detector using up to 25 fb^{-1} of proton-proton collision data," ATLAS-CONF-2013-034.

[5] [CMS Collaboration], "Combination of standard model Higgs boson searches and measurements of the properties of the new boson with a mass near 125 GeV," CMS-PAS-HIG-12-045.

[6] [ATLAS Collaboration], "Coupling properties of the new Higgs-like boson observed with the ATLAS detector at the LHC," ATLAS-CONF-2012-127.

[7] Y. Chen, J. Lykken, M. Spiropulu, D. Stolarski and R. Vega-Morales, "Golden Probe of Electroweak Symmetry Breaking," Phys. Rev. Lett. **117**, no. 24, 241801 (2016) [arXiv:1608.02159 [hep-ph]].

[8] G. Aad *et al.* [ATLAS and CMS Collaborations], "Measurements of the Higgs boson production and decay rates and constraints on its couplings from a combined ATLAS and CMS analysis of the LHC pp collision data at $\sqrt{s} = 7$ and 8 TeV," JHEP **1608**, 045 (2016) [arXiv:1606.02266 [hep-ex]].

[9] T. Corbett, O. J. P. Eboli, D. Goncalves, J. Gonzalez-Fraile, T. Plehn and M. Rauch, "The Higgs Legacy of the LHC Run I," JHEP **1508**, 156 (2015) [arXiv:1505.05516[hep-ph]].

[10] S. Chatrchyan *et al.* [CMS Collaboration], "Measurement of the Properties of a Higgs Boson in the Four-Lepton Final State," Phys. Rev. D **89**, no. 9, 092007 (2014) [arXiv:1312.5353 [hep-ex]].

[11] G. Aad *et al.* [ATLAS Collaboration], "Evidence for the spin-0 nature of the Higgs boson using ATLAS data," Phys. Lett. B **726**, 120 (2013) [arXiv:1307.1432 [hep-ex]].

[12] H. Georgi and M. Machacek, "Doubly Charged Higgs Bosons," Nucl. Phys. B **262**, 463 (1985).

[13] M. S. Chanowitz and M. Golden, "Higgs Boson Triplets With M (W) = M (Z) $\cos\theta\omega$," Phys. Lett. **165B**, 105 (1985).

[14] J. F. Gunion, R. Vega and J. Wudka, "Higgs triplets in the standard model," Phys. Rev. D **42**, 1673 (1990).

[15] J. F. Gunion, R. Vega and J. Wudka, "Naturalness problems for rho = 1 and other large one loop effects for a standard model Higgs sector containing triplet fields," Phys. Rev. D **43**, 2322 (1991).

[16] C. H. de Lima, D. Stolarski and Y. Wu, "Status of negative coupling modifiers for extended Higgs sectors," Phys. Rev. D **105** (2022) no.3, 035019 [arXiv:2111.02533 [hep-ph]].

[17] C. W. Chiang, X. G. He and G. Li, "Measuring the ratio of HWW and HZZ couplings through W^+W^-H production," JHEP **1808**, 126 (2018) [arXiv:1805.01689 [hep-ph]].

[18] D. Stolarski and Y. Wu, "Tree-level interference in vector boson fusion production of Vh," Phys. Rev. D **102** (2020) no.3, 033006 [arXiv:2006.09374 [hep-ph]].

[19] K. P. Xie and B. Yan, "Probing the electroweak symmetry breaking with Higgs production at the LHC," Phys. Lett. B **820** (2021), 136515 [arXiv:2104.12689 [hep-ph]].

[20] CMS Collaboration [CMS Collaboration], "Combined measurements of the Higgs boson's couplings at $\sqrt{s} = 13$ TeV," CMS-PAS-HIG-17-031. URL http://cds.cern.ch/record/2308127.

[21] G. Aad *et al.* [ATLAS], "Combined measurements of Higgs boson production and decay using up to 80 fb^{-1} of proton-proton collision data at $\sqrt{s} = 13$ TeV collected with the ATLAS experiment," Phys. Rev. D **101** (2020) no.1, 012002 [arXiv:1909.02845 [hep-ex]].

[22] E. Gabrielli, M. Heikinheimo, L. Marzola, B. Mele, C. Spethmann and H. Veermae, "Anomalous Higgs-boson coupling effects in HW+W- production at the LHC," Phys. Rev. D **89**, no. 5, 053012 (2014) [arXiv:1312.4956 [hep-ph]].

[23] K. Hagiwara, S. Ishihara, J. Kamoshita and B. A. Kniehl, "Prospects of measuring general Higgs couplings at e+ e- linear colliders," Eur. Phys. J. C **14**, 457 (2000) [hep-ph/0002043].

[24] S. S. Biswal, R. M. Godbole, R. K. Singh and D. Choudhury, "Signatures of anomalous VVH interactions at a linear collider," Phys. Rev. D **73**, 035001 (2006) Erratum: [Phys. Rev. D **74**, 039904 (2006)] [hep-ph/0509070].

[25] R. M. Godbole, D. J. Miller and M. M. Muhlleitner, "Aspects of CP violation in the H ZZ coupling at the LHC," JHEP **0712**, 031 (2007) [arXiv:0708.0458 [hep-ph]].

[26] S. S. Biswal, D. Choudhury, R. M. Godbole and Mamta, "Role of polarization in probing anomalous gauge interactions of the Higgs boson," Phys. Rev. D **79**, 035012 (2009) [arXiv:0809.0202 [hep-ph]].

[27] I. Anderson *et al.* "Constraining Anomalous HVV Interactions at Proton and Lepton Colliders," Phys. Rev. D **89**, no. 3, 035007 (2014) [arXiv:1309.4819 [hep-ph]].

[28] N. Craig, J. Gu, Z. Liu and K. Wang, "Beyond Higgs Couplings: Probing the Higgs with Angular Observables at Future e$^+$ e$^-$ Colliders," JHEP **1603**, 050 (2016) [arXiv:1512.06877[hep-ph]].

[29] S. Kumar, P. Poulose and S. Sahoo, "Study of Higgs-gauge boson anomalous couplings through $e^-e^+ \to W^-W^+H$ at ILC," Phys. Rev. D **91**, no. 7, 073016 (2015) [arXiv:1501.03283 [hep-ph]].

[30] V. Khachatryan *et al.* [CMS Collaboration], "Constraints on the spin-parity and anomalous HVV couplings of the Higgs boson in proton collisions at 7 and 8 TeV," Phys. Rev. D **92**, no. 1, 012004 (2015) [arXiv:1411.3441 [hep-ex]].

[31] V. Khachatryan *et al.* [CMS Collaboration], "Combined search for anomalous pseudoscalar HVV couplings in VH(H $\to b\bar{b}$) production and H $\to$ VV decay," Phys. Lett. B **759**, 672 (2016) [arXiv:1602.04305 [hep-ex]].

[32] A. M. Sirunyan *et al.* [CMS Collaboration], "Constraints on anomalous Higgs boson couplings using production and decay information in the four-lepton final state," Phys. Lett. B **775**, 1 (2017) [arXiv:1707.00541 [hep-ex]].

[33] A. M. Sirunyan *et al.* [CMS Collaboration], "Combined measurements of Higgs boson couplings in protonâproton collisions at $\sqrt{s} = 13\,\text{TeV}$," Eur. Phys. J. C **79**, no. 5, 421 (2019) [arXiv:1809.10733 [hep-ex]].

[34] A. M. Sirunyan *et al.* [CMS Collaboration], "Measurements of the Higgs boson width and anomalous HVV couplings from on-shell and off-shell production in the four-lepton final state," Phys. Rev. D **99**, no. 11, 112003 (2019) [arXiv:1901.00174 [hep-ex]].

[35] G. Aad *et al.* [ATLAS Collaboration], "Study of the spin and parity of the Higgs boson in diboson decays with the ATLAS detector," Eur. Phys. J. C **75**, no. 10, 476 (2015) Erratum: [Eur. Phys. J. C **76**, no. 3, 152 (2016)] [arXiv:1506.05669 [hep-ex]].

[36] M. Aaboud *et al.* [ATLAS Collaboration], "Measurement of the Higgs boson coupling properties in the $H \to ZZ^* \to 4\ell$ decay channel at $\sqrt{s} = 13$ TeV with the ATLAS detector," JHEP **1803**, 095 (2018) [arXiv:1712.02304 [hep-ex]].

[37] M. Aaboud *et al.* [ATLAS Collaboration], "Measurements of Higgs boson properties in the diphoton decay channel with 36 fb^{-1} of pp collision data at $\sqrt{s} = 13$ TeV with the ATLAS detector," Phys. Rev. D **98**, 052005 (2018) [arXiv:1802.04146 [hep-ex]].

[38] G. Aad *et al.* [ATLAS Collaboration], "Combined measurements of Higgs boson production and decay using up to 80 fb^{-1} of proton-proton collision data at $\sqrt{s} = 13$ TeV collected with the ATLAS experiment," [arXiv:1909.02845 [hep-ex]].

[39] The ATLAS collaboration [ATLAS Collaboration], "Measurement of gluon fusion and vector boson fusion Higgs boson production cross-sections in the $H \to WW^* \to e\nu\mu\nu$ decay channel in pp collisions at $\sqrt{s} = 13$ TeV with the ATLAS detector," ATLAS-CONF-2018-004. https://cds.cern.ch/record/2308392.

[40] [CMS Collaboration], "Projected Performance of an Upgraded CMS Detector at the LHC and HL-LHC: Contribution to the Snowmass Process," [arXiv:1307.7135 [hep-ex]].

[41] J. de Blas *et al.*, "Higgs Boson Studies at Future Particle Colliders," [arXiv:1905.03764 [hep-ph]].

[42] T. Behnke *et al.* [ILC], "ILC Reference Design Report Volume 4 - Detectors," arXiv:0712.2356 [physics.ins-det].

[43] C. Adolphsen *et al.*, "The International Linear Collider Technical Design Report - Volume 3.II: Accelerator Baseline Design," arXiv:1306.6328 [physics.acc-ph].

[44] A. Robson *et al.* "The Compact Linear e^+e^- Collider (CLIC): Accelerator and Detector," arXiv:1812.07987 [physics.acc-ph].

[45] A. Abada *et al.* [FCC], "FCC-ee: The Lepton Collider: Future Circular Collider Conceptual Design Report Volume 2," Eur. Phys. J. ST **228** (2019) no.2, 261-623

[46] [CEPC Study Group], "CEPC Conceptual Design Report: Volume 1 - Accelerator," arXiv:1809.00285 [physics.acc-ph].

[47] M. Bai, T. Barklow *et al.* "C^3: A "Cool" Route to the Higgs Boson and Beyond," [arXiv:2110.15800 [hep-ex]].

[48] A. Abada *et al.* [FCC], "FCC-hh: The Hadron Collider: Future Circular Collider Conceptual Design Report Volume 3," Eur. Phys. J. ST **228** (2019) no.4, 755-1107

[49] K. Fujii, C. Grojean *et al.* "Physics Case for the 250 GeV Stage of the International Linear Collider," [arXiv:1710.07621 [hep-ex]].

[50] K. Fujii *et al.* [LCC Physics Working Group], "Tests of the Standard Model at the International Linear Collider," [arXiv:1908.11299 [hep-ex]].

[51] The ATLAS collaboration [ATLAS Collaboration], "Combined measurement of differential and inclusive total cross sections in the $H \to \gamma\gamma$ and the $H \to ZZ^* \to 4\ell$ decay channels at $\sqrt{s} = 13$ TeV with the ATLAS detector," ATLAS-CONF-2018-002. https://cds.cern.ch/record/2308390.

[52] S. L. Glashow, "The renormalizability of vector meson interactions," Nucl. Phys. 10 (1959) 107.

[53] S. L. Glashow, "Partial Symmetries of Weak Interactions," Nucl. Phys. 22 (1961) 579.

[54] S. Weinberg, "The renormalizability of vector meson interactions," 'A Model of Leptons', Phys. Rev. Lett. 19 (1967) 1264.

[55] S. L. Glashow, J. Iliopoulos and L. Maiani, "Weak Interactions with Lepton-Hadron Symmetry," Phys. Rev. D2 (1970) 1285.

[56] Y. Ne'eman, "Derivation of strong interactions from a gauge invariance," Nucl. Phys. 26 (1961) 222.

[57] M. Gell-Mann, "Symmetries of baryons and mesons," Phys. Rev. 125 (1962) 1067.

[58] M. Gell-Mann, "A Schematic Model of Baryons and Mesons," Phys. Lett. 8 (1964) 214.

[59] H. Fritzsch, M. Gell-Mann and H. Leutwyler, "Advantages of the Color Octet Gluon Picture," Phys. Lett. 47B (1973) 365. [37].

[60] J. Ellis, "The Discovery of the Gluon," Int. J. Mod. Phys. A **29** (2014) no.31, 1430072 [arXiv:1409.4232 [hep-ph]].

[61] M. Banner *et al.* [UA2], "Observation of Single Isolated Electrons of High Transverse Momentum in Events with Missing Transverse Energy at the CERN anti-p p Collider,"Phys. Lett. B **122** (1983), 476-485

[62] G. Arnison *et al.* [UA1], "Experimental Observation of Lepton Pairs of Invariant Mass Around 95 GeV/c^2 at the CERN SPS Collider," Phys. Lett. B **126** (1983), 398-410

[63] P. Bagnaia *et al.* [UA2], "Evidence for $Z^0 \to e^+e^-$ at the CERN $\bar{p}p$ Collider," Phys. Lett. B **129** (1983), 130-140

[64] A. Einstein, "Über einen die Erzeugung und Verwandlung des Lichtes be-treffenden heuristischen Gesichtspunkt," Ann. Phys., 322: 132-148. (1905)

[65] N. Cabibbo, "Unitary Symmetry and Leptonic Decays," Phys. Rev. Lett. 10 (1963) 531.

[66] M. Kobayashi and T. Maskawa, "CP Violation in the Renormalizable Theory of Weak Interaction," Prog. Theor. Phys. 49 (1973) 652.

[67] S.L. Glashow, Nucl. Phys. B 22 (1961) 579; S. Weinberg, Phys. Rev. Lett. 19 (1967) 1264; A. Salam, in: Proceedings of the 8th Nobel Symposium, p. 367, ed. N. Svartholm, Almqvist and Wiksell, Stockholm 1968.

[68] M. C. Gonzalez-Garcia and Y. Nir, "Neutrino masses and mixing: Evidence and implications," Rev. Mod. Phys. **75** (2003), 345-402 [arXiv:hep-ph/0202058 [hep-ph]].

[69] A. S. Barabash, "Double beta decay: Present status," Phys. Atom. Nucl. **73** (2010), 162-178 [arXiv:0807.2948 [hep-ex]].

[70] M. E. Peskin and D. V. Schroeder, "An Introduction to Quantum Field Theory", Addison-Wesley, 1995, Chapter on QCD,

[71] C. L. Cowan Jr. and F. Reines. 178:pp. 446-449, 1956. C. L. Cowan Jr., F. Reines, F. B. Harrison, H. W. Kruse, and A. D. McGuire. Science, 124(3212):pp. 103-104,1956.

[72] F. J. Hasertet al., "Observation of neutrino-like interactions without muon orelectron in the Gargamelle neutrino experiment," Phys. Lett., vol. B46, pp. 138–140, 1973.

[73] J. R. Espinosa and M. Quiros, "Improved metastability bounds on the standard model Higgs mass," Phys. Lett. B **353** (1995), 257-266 [arXiv:hep-ph/9504241 [hep-ph]].

[74] G. Isidori, G. Ridolfi and A. Strumia, "On the metastability of the standard model vacuum," Nucl. Phys. B **609** (2001), 387-409 [arXiv:hep-ph/0104016 [hep-ph]].

[75] J. R. Espinosa, G. F. Giudice and A. Riotto, "Cosmological implications of the Higgs mass measurement," JCAP **05** (2008), 002 [arXiv:0710.2484 [hep-ph]].

[76] J. Ellis, J. R. Espinosa, G. F. Giudice, A. Hoecker and A. Riotto, "The Probable Fate of the Standard Model," Phys. Lett. B **679** (2009), 369-375 [arXiv:0906.0954 [hep-ph]].

[77] G. Degrassi, S. Di Vita, J. Elias-Miro, J. R. Espinosa, G. F. Giudice, G. Isidori and A. Strumia, "Higgs mass and vacuum stability in the Standard Model at NNLO," JHEP **08** (2012), 098 [arXiv:1205.6497 [hep-ph]].

[78] F. Bezrukov, M. Y. Kalmykov, B. A. Kniehl and M. Shaposhnikov, "Higgs Boson Mass and New Physics," JHEP **10** (2012), 140 [arXiv:1205.2893 [hep-ph]].

[79] D. Buttazzo, G. Degrassi, P. P. Giardino *et al.*, "Investigating the near-criticality of the Higgs boson," JHEP **12** (2013), 089 [arXiv:1307.3536 [hep-ph]].

[80] A. Andreassen, W. Frost and M. D. Schwartz, "Consistent Use of the Standard Model Effective Potential," Phys. Rev. Lett. **113** (2014) no.24, 241801 [arXiv:1408.0292 [hep-ph]].

[81] Z. Lalak, M. Lewicki and P. Olszewski, "Higher-order scalar interactions and SM vacuum stability," JHEP **05** (2014), 119 [arXiv:1402.3826 [hep-ph]].

[82] M. F. Zoller, "Standard Model beta-functions to three-loop order and vacuum stability," [arXiv:1411.2843 [hep-ph]].

[83] A. V. Bednyakov, B. A. Kniehl, A. F. Pikelner and O. L. Veretin, "Stability of the Electroweak Vacuum: Gauge Independence and Advanced Precision," Phys. Rev. Lett. **115** (2015) no.20, 201802 [arXiv:1507.08833 [hep-ph]].

[84] V. Branchina, E. Messina and M. Sher, "Lifetime of the electroweak vacuum and sensitivity to Planck scale physics," Phys. Rev. D **91** (2015), 013003 [arXiv:1408.5302 [hep-ph]].

[85] G. Iacobellis and I. Masina, "Stationary configurations of the Standard Model Higgs potential: electroweak stability and rising inflection point," Phys. Rev. D **94** (2016) no.7, 073005 [arXiv:1604.06046 [hep-ph]].

[86] S. Chigusa, T. Moroi and Y. Shoji, "Decay Rate of Electroweak Vacuum in the Standard Model and Beyond," Phys. Rev. D **97** (2018) no.11, 116012 [arXiv:1803.03902 [hep-ph]].

[87] S. Chigusa, T. Moroi and Y. Shoji, "State-of-the-Art Calculation of the Decay Rate of Electroweak Vacuum in the Standard Model," Phys. Rev. Lett. **119** (2017) no.21, 211801 [arXiv:1707.09301 [hep-ph]].

[88] S. R. Coleman, "The Fate of the False Vacuum. 1. Semiclassical Theory," Phys. Rev. D **15** (1977), 2929-2936 [erratum: Phys. Rev. D **16** (1977), 1248]

[89] G. Zweig, "An SU(3) model for strong interaction symmetry and its breaking," in: Developments in the Quark Theory of Hadrons, ed. by D. B. Lichtenberg and S. P. Rosen, vol. 1, 1964 22.

[90] A. Andreassen, W. Frost and M. D. Schwartz, "Scale Invariant Instantons and the Complete Lifetime of the Standard Model," Phys. Rev. D **97** (2018) no.5, 056006 [arXiv:1707.08124 [hep-ph]].

[91] N. Aghanim *et al.* [Planck], "Planck 2018 results. VI. Cosmological parameters," Astron. Astrophys. **641** (2020), A6 [erratum: Astron. Astrophys. **652** (2021), C4] arXiv:1807.06209 [astro-ph.CO].

[92] A. D. Sakharov, "Violation of CP Invariance, C asymmetry, and baryon asymmetry of the universe," Pisma Zh. Eksp. Teor. Fiz. **5** (1967), 32-35

[93] Encyclopædia Britannica, "Dark Matter," *britannica.com*, https://www.britannica.com/science/dark-matter.

[94] NASA, *What is Dark Matter?*, 2024. https://www.nasa.gov/audience/forstudents/9-12/features/what-is-dark-matter.html, and "Building Blocks of the Universe," *science.nasa.gov*, https://science.nasa.gov/universe/overview/building-blocks/.

[95] Planck, 'Planck 2018 results. VI. Cosmological parameters', (2018), 1807.06209.

[96] Y. Fukuda *et al.* [Super-Kamiokande], "Evidence for oscillation of atmospheric neutrinos," Phys. Rev. Lett. **81** (1998), 1562-1567 [arXiv:hep-ex/9807003 [hep-ex]].

[97] J.˜L.˜Feng, "Dark Matter Candidates from Particle Physics and Methods of Detection," Ann. Rev. Astron. Astrophys. **48** (2010), 495-545 arXiv:1003.0904 [astro-ph.CO].

[98] SNO Collaboration, Q. R. Ahmad *et al.* "Direct evidence for neutrino flavor transformation from neutral-current interactions in the Sudbury Neutrino Observatory," Phys. Rev. Lett. 89 (2002) 011301, [arXiv:nucl-ex/0204008].

[99] D. S. Akerib *et al.* [LUX], "Results from a search for dark matter in the complete LUX exposure," Phys. Rev. Lett. **118** (2017) no.2, 021303 arXiv:1608.07648 [astro-ph.CO].

[100] X. Cui *et al.* [PandaX-II], "Dark Matter Results From 54-Ton-Day Exposure of PandaX-II Experiment," Phys. Rev. Lett. **119** (2017) no.18, 181302 arXiv:1708.06917 [astro-ph.CO].

[101] A. David *et al.* [LHC Higgs Cross Section Working Group], "LHC HXSWG interim recommendations to explore the coupling structure of a Higgs-like particle," [arXiv:1209.0040 [hep-ph]].

[102] Ettore Majorana, "Teoria Simmetrica Dell' Elettrone E Del Positrone," Nuovo Cimento 14 (1937) pp.171–184.

[103] "LCC - Linear Collider Collaboration," www.linearcollider.org. Retrieved 2016-12-14.

[104] The International Linear Collider - Gateway to the Quantum Universe, ILC Community. 2007-10-18.

[105] Ties Behnke, *et al.* "The International Linear Collider Technical Design Report - Volume 1: Executive Summary. 2013," [arXiv:1306.6327 [hep-ph]].

[106] H. Baer, *et al.* "The International Linear Collider Technical Design Report - Volume 2: Physics," [arXiv:1306.6352 [hep-ph]].

[107] Gerald Aarons *et al.* "ILC Reference Design Report Volume 3 - Accelerator. 2007," [arXiv:0712.2361].

[108] G. Cowan, K. Cranmer, E. Gross, and O. Vitells, Eur. Phys.J. C 71, 1554 (2011).

[109] J. Alwall *et al.* "A Standard format for Les Houches event files," In: Comput. Phys. Commun. 176 (2007), pp. 300–304.

[110] Lyn Evans and Shinichiro Michizono, "The International Linear Collider," Machine Staging Report 2017. 2017, 1711.00568.

[111] Ties Behnke *et al.* "The International Linear Collider Technical Design Report - Volume 4: Detectors. 2013, 1306.6329.

[112] Hitoshi Murayama and Michael E. Peskin, "Physics opportunities of e+ e- linear colliders," Ann. Rev. Nucl. Part. Sci., 46:533–608, 1996, hep-ex/9606003.

[113] Wolfgang Kilian, Thorsten Ohl, and Jurgen Reuter, "WHIZARD: Simulating Multi-Particle Processes at LHC and ILC," Eur. Phys. J., C71:1742, 2011, 0708.4233.

[114] Rey. Hori, ILC / Structural view of ILD detector, 2011 from https://linearcollider.org/wp-content/uploads/2022/12/01_ilc2011_ILD_A4_110925.jpg.

[115] Rey. Hori, ILC / general view of SiD detector, 2012 from https://linearcollider.org/wp-content/uploads/2022/12/05_ilc2012_SiD_A4_121108.jpg.

[116] A. Shoji, "Measurement of dE/dx resolution of TPC prototype with gating GEM exposed to an electron beam," arXiv:1801.04499 [physics.ins-det].

[117] M.A Thomson, "Particle Flow Calorimetry and the PandoraPFA Algorithm," 2009 Nucl.Instrum.Meth.A611, 25–40, arXiv:0907.3577 [physics.ins-det].

[118] K. Yokoya *et al.* [Positron Working Group Collaboration], "Report on the ILC Positron Source," 78 pp. (2018)

[119] A.˜Aryshev *et al.* [ILC International Development Team], "The International Linear Collider: Report to Snowmass 2021," arXiv:2203.07622 [physics.acc-ph].

[120] M. Tanabashi *et al.* [Particle Data Group], "Review of Particle Physics," Phys. Rev. D 98, no. 3, 030001 (2018).

[121] E. Aprile *et al.* [XENON], "Dark Matter Search Results from a One Ton-Year Exposure of XENON1T," Phys. Rev. Lett. **121** (2018) no.11, 111302 arXiv:1805.12562 [astro-ph.CO].

[122] [LHC Higgs Cross Section Working Group], S. Dittmaier, C. Mariotti, G. Passarino, and R. Tanaka (Eds.). "Handbook of LHC Higgs Cross Sections: 2. Differential Distributions," CERN-2012-002, CERN, Geneva, 2012, 1201.3084.

[123] [LHC Higgs Cross Section Working Group], S. Heinemeyer, C. Mariotti, G. Passarino, and R. Tanaka (Eds.). "Handbook of LHC Higgs Cross Sections: 3. Higgs Properties," CERN-2013-004, CERN, Geneva, 2013, 1307.1347.

[124] S. Kumar and P. Poulose "Influence of anomalous VVH and VVHH on determination of Higgs self couplings at ILC," [arXiv:1408.3563 [hep-ph]].

[125] J. Alwall *et al.*, "The automated computation of tree-level and next-to-leading order differential cross sections, and their matching to parton shower simulations," JHEP **1407**, 079 (2014) [arXiv:1405.0301[hep-ph]].

[126] https://twiki.cern.ch/twiki/bin/view/LHCPhysics/CERNYellowReportPageBR.

[127] T. Sjostrand, S. Mrenna and P. Z. Skands, "A Brief Introduction to PYTHIA 8.1," Comput. Phys. Commun. **178**, 852 (2008) [arXiv:0710.3820 [hep-ph]].

[128] T. Sjöstrand, S. Ask, J. R. Christiansen, R. Corke, N. Desai, P. Ilten, S. Mrenna, S. Prestel, C. O. Rasmussen and P. Z. Skands, "An introduction to PYTHIA 8.2," Comput. Phys. Commun. **191** (2015), 159-177 [arXiv:1410.3012 [hep-ph]].

[129] I. Antcheva *et al.* "ROOT: A C++ framework for petabyte data storage, statistical analysis and visualization," Comput. Phys. Commun. 180 (2009) 2499 arXiv:1508.07749 [physics.data-an].

[130] J. de Favereau *et al.* [DELPHES 3 Collaboration], "DELPHES 3, A modular framework for fast simulation of a generic collider experiment," JHEP **1402**, 057 (2014) [arXiv:1307.6346 [hep-ex]].

[131] M. Cacciari, G. P. Salam and G. Soyez, "FastJet User Manual," Eur. Phys. J. C **72**, 1896 (2012) [arXiv:1111.6097 [hep-ph]].

[132] M. Cacciari and G. P. Salam, "Dispelling the N^3 myth for the k_t jet-finder," Phys. Lett. B **641** (2006), 57-61 [arXiv:hep-ph/0512210 [hep-ph]].

[133] M. Cacciari, G. P. Salam and G. Soyez, "The anti-k_t jet clustering algorithm," JHEP **0804**, 063 (2008) [arXiv:0802.1189 [hep-ph]].

[134] A. Höcker *et al.*, "TMVA - Toolkit for Multivariate Data Analysis," PoS **ACAT** (2007), 040 [arXiv:physics/0703039 [physics.data-an]].

[135] P. Roe, H. Yang, J. Zhu, Y. Liu, I. Stancu, and G. McGregor, "Boosted Decision Trees as an Alternative to Artificial Neural Networks for Particle Identification," Nucl. Instrum. Meth. A **543** (2005), 577-584.

[136] A. Radovic *et al.*, "Machine learning at the energy and intensity frontiers of particle physics," Nature **560** (2018), 41–48 [arXiv:1806.11484 [hep-ex]].

[137] A. Falkowski and F. Riva, "Model-independent precision constraints on dimension-6 operators," JHEP **02** (2015), 039 [arXiv:1411.0669 [hep-ph]].

[138] G. C. Branco, P. M. Ferreira, L. Lavoura, M. N. Rebelo, M. Sher and J. P. Silva, "Theory and phenomenology of two-Higgs-doublet models," Phys. Rept. **516** (2012), 1–102 [arXiv:1106.0034 [hep-ph]].